ABSTRACT

Title of Dissertation: STUDY OF CONDENSATION OF
REFRIGERANTS IN MICRO-CHANNELS
FOR DEVELOPMENT OF FUTURE
COMPACT MICRO-CHANNEL
CONDENSERS

        Sourav Chowdhury, Doctor of Philosophy, 2008

Directed By: Professor Michael Ohadi, Department of
Mechanical Engineering

Mini- and micro- channel technology has gained considerable ground in the recent years in industry and is favored due to its several advantages stemming from its high surface to volume ratio and high values of proof pressure it can withstand. Micro-channel technology has paved the way to development of highly compact heat exchangers with low cost and mass penalties. In the present work, the issues related to the sizing of compact micro-channel condensers have been explored. The considered designs encompass both the conventional and MEMS fabrication techniques. In case of MEMS-fabricated micro-channel condenser, wet etching of the micro-channel structures, followed by bonding of two such wafers with silicon nitride layers at the interface was attempted. It was concluded that the silicon nitride bonding requires great care in terms of high degree of surface flatness and absence of roughness and also high degree of surface purity and thus cannot be recommended for mass fabrication. Following this investigation, a carefully prepared experimental setup and test micro-channel with hydraulic diameter 700 μm and aspect ratio 7:1 was fabricated and overall heat transfer and pressure drop aspects of two condensing refrigerants, R134a and R245fa were studied at a variety of test conditions. To the best of author's knowledge, so far no data has been reported in the

literature on condensation in such high aspect ratio micro-channels. Most of the published experimental works on condensation of refrigerants are concerning conventional hydraulic diameter channels (> 3mm) and only recently some experimental data has been reported in the sub-millimeter scale channels for which the surface tension and viscosity effects play a dominant role and the effect of gravity is diminished. It is found that both experimental data and empirically-derived correlations tend to under-predict the present data by an average of 25%. The reason for this deviation could be because a high aspect ratio channel tends to collect the condensate in the corners of its cross-section leaving only a thin liquid film on the flat side surfaces for better heat transfer than in circular or low aspect ratio channels.

STUDY OF CONDENSATION OF REFRIGERANTS IN A MICRO-CHANNEL FOR

DEVELOPMENT OF FUTURE COMPACT MICRO-CHANNEL CONDENSERS

By

Sourav Chowdhury

Dissertation submitted to the Faculty of the Graduate School of the
University of Maryland, College Park in partial fulfillment
of the requirements for the degree of
Doctor of Philosophy
2008

Advisory Committee:
Professor Michael Ohadi, Chair/Advisor
Professor Marino di Marzo
Professor Jungho Kim
Assistant Professor Bao Yang
Professor Gary A. Pertmer

Dedication

To my parents for whose unconditional love and dedication I am forever gratefully

indebted

Acknowledgements

First and foremost I would like to thank my advisor Dr. Michael Ohadi, whom I am indebted to for his encouragement, counsel and support throughout the course of my study and research.

I also extend my appreciation to the other members of my advisory committee who provided support and guidance, including Dr. Marino di Marzo, Dr. Jungho Kim, Dr. Bao Yang, and Dr. Gary A. Pertmer.

During the course of my research, Dr. Serguei Dessiatoun and Dr. Amir Shoustari have afforded me invaluable their support and guidance. I am grateful for their generous help and counsel. Also, I had the privilege of working with and being advised by several fellow scientists, including Dr. Francis Franca and Dr. John Lawler, to whom I wish to express my sincere gratitude. I would also like to thank Dr. Reza Ghodssi, for his suggestions and interaction and providing me with the opportunity of productive interaction with his team and access to micro-fabrication facilities.

I am grateful to my many friends and colleagues at the Smart and Small Thermal Systems Laboratory for providing a stimulating and constructive environment to learn and grow. I am especially thankful to Dr. Vytenis Benetis, Dr. Parisa Foroughi, Dr. Guohua Kuang, Dr. Saeed Moghaddam, Arman Molki, Dr. Mihai Catalin Rada, Dr. Valentin Tudor, Dr. Jianlin Wu, Ebrahim Al-Hajri, Edvin Cetegen and Mohamed Al-Shehhi. I would also like to thank my friends in MEMS Sensors and Actuators Lab who have assisted me in some aspects of micro-fabrication.

Finally, I wish to thank ASHRAE Research Grant Committee, the AHX/EHD Consortium and ATEC Inc. for their invaluable financial support of this project.

TABLE OF CONTENTS

NOMENCLATURE

A	Constant	j	Index Variable
A_c	Cross-sectional Area (m^2)	k	Thermal Conductivity (W/m^{2}K)
$A_{Surface}$	Surface Area (m^2)	L	Channel Length (m)
a_r	Aspect Ratio	$\dot{m}$	Mass Flow Rate (kg/s)
a	Width (m)	n	Index Variable
b	Height (m)	$\overline{Nu}$	Average Nusselt Number
c, C	Constant	p, q, r	Constant
Co	Confinement Number	P	Perimeter (m)
D	Diameter (m)	P_w	Wetted Perimeter (m)
D_h	Hydraulic Diameter (m)	P	Pressure (Pa or kPa)
EB	Energy Balance Ratio	q, Q	Heat Transfer Rate (W)
f	Friction Factor	q''	Heat Flux (W/m^2)
Fr, Fr*	Froude Number	q'	Heat Transfer Rate Per Unit Length (W/m)
G	Mass Flux (kg/m^{2}s)		
g	gravity(m/s^2)	R	Thermal Resistance (K/W)
Ga	Galileo Number	Re	Reynolds Number
h	Heat Transfer Coefficient (W/m^{2}K)	S_r	Slip Ratio
		T	Temperature (C)
$\overline{h}$	Average Heat Transfer Coefficient (W/m^{2}K)	t	Thickness (m)
		U	Average Velocity (m/s)
i	Specific Enthalpy (J/kg)	U	Uncertainty
j_g, $j_g{}^*$	Dimensionless Gas Velocity	V	Velocity (m/s)

$\dot{V}$ Volumetric Flow Rate (liter/min)

We   Weber Number

X   Matrinelli Parameter

x   Vapor Mass Fraction, Quality

X, Y   Coordinate Axes (m)

z   Axial Coordinate (m)

GREEK SYMBOLS

α Void Fraction

β Volumetric Void Fraction

δ Height (m)

δ Film Thickness (m)

Δ Difference

ε Surface Roughness (m)

μ Dynamic Viscosity (kg/m.s)

ν Kinematic Viscosity (m^2/s)

ϕ Two-Phase Multiplier

σ Surface Tension (N/m)

τ Shear Stress (N/m^2)

SUBSCRIPTS

c   capillary

corr   from correlation

Cu   Copper

evap   evaporator

f   liquid

g   gas/vapor

GS   superficial vapor

h   hydraulic

h   height

i   interfacial

in   inlet

out   outlet

l   liquid

ln   logarithmic

LS   superficial liquid

ref   refrigerant

sat   saturation

th   thermodynamic

tt   turbulent-turbulent

v   vapor

w   wall

LIST OF TABLES

LIST OF FIGURES

Chapter 1

INTRODUCTION

1.1 BACKGROUND

Micro-channel technology has gained considerable ground in recent years in industry and is favored for its capability to yield low cost, compact heat and mass transfer devices due to high surface to volume ratio, among other advantages. Considerable volume of literature exists on micro-channel cooling techniques – by liquid phase and phase changing fluids – applied to cooling of electronics and other high heat flux devices for a wide range of both military and commercial applications. More recently, the interest in overall compactness of thermal cooling loops has spurred interest in studying condensing refrigerants in micro-channels to complement the micro-channel evaporator technology. Due to high heat transfer coefficients it offers and high values of proof pressures it can withstand, micro-channel technology also finds strong interest in two-phase flows of high pressure refrigerants used automotive & stationary heating, ventilating, and air conditioning/refrigeration (HVAC-R) industry.

With the significant demand in this field, the art of combining and utilizing the manifold benefits of the micro-channel technology is further ahead that the science of obtaining comprehensive understanding of fluidic heat and mass transfers in these channels. This is more so for condensing flows in micro-channels which is of recent interest as evidenced by a number of publications on experimental and theoretical works within the present decade. Several heat transfer and pressure drop correlations have been proposed for various micro- and mini- channel sizes and with a variety of refrigerants, mostly pressurized ones. Most of these correlations have purely experimental basis and

some were created with guidance from analytical and flow visualization understandings. These published experimental data and proposed correlations form a valuable basis for the design and development of compact micro-channel evaporators and condensers.

In the present work, the feasibility of fabrication of a compact micro-channel condenser with interconnects, using conventional MEMS techniques, have been explored to understand its issues and limitations. Following this, an experimental investigation of condensation of refrigerants in a high aspect ratio micro-channel with two pressurized refrigerants, R134a and R245fa have been carried out to understand the applicability of the available correlations. The study involved parametric variations of the flow aspects and calculated/measured the overall heat transfer coefficient and pressure drop. This knowledge is essential for the sizing of the condenser in the design phase. Thus, the present work adds to the growing body of experimental literature on condensation in mini- and micro-channels. The present work is a part of a longer undertaking for a comprehensive investigation and assessment of the physics of such flows in a single micro-channel.

1.2 RESEARCH OBJECTIVES & SCOPE

Following are the broad objectives of the present work:

1) To explore the issues in fabrication of a condenser structure in silicon for the use in electronics cooling applications.

2) To generate experimental data of heat transfer and pressure drop for a single high aspect ratio micro-channel and compare those with reported correlations from the literature to understand their applicability in relation to condenser sizing and designing.

1.3 RESEARCH APPROACH AND PRESENTATION OF WORK

First, a thorough literature survey and review was conducted and is presented in Chapter 2. Next, to fulfill the objectives of research, preliminary experiments were carried out in a compact condenser made by Electro-discharge machining (EDM) on a brass plate and in a thermo-siphon test setup with a single transparent glass capillary tube, which are reported in Chapter 3. Then, in Chapter 4, the feasibility of micro-fabrication process as a means for making micro-channels in a silicon substrate is explored. In Chapters 5 through 7, an experimental investigation is reported with two pressurized refrigerants, R134a and R245fa, in a specially constructed horizontal single-channel micro-condenser of hydraulic diameter 0.7 mm and aspect ration 7:1. A compact experimental setup was constructed and instrumented with care to lower the heat loss/gain effects which affected the uncertainties in data. Overall heat transfer coefficient and pressure drop data were then collected and comparison of this data against various correlations meant both for conventional scale tubes and micro-channels were made. CFD-based approximate numerical inverse heat transfer modeling was adopted with manual iterations to investigate the local heat transfer effects in the channel for selected data points. Finally, in Chapter 8, several conclusions are presented and the future efforts needed to bring a closure to the present work are indicated.

1.4 SUMMARY

In the present chapter, the background and need for the present research is stated and the research scope is broadly outlined. The research approach encompassing the objectives and issues of interest that arose during the research is briefly described.

Chapter 2

LITERATURE REVIEW OF CONDENSING FLOWS IN SMALL HYDRAULIC
DIAMETER CHANNELS

2.1 INTRODUCTION

In the past decade significant attention has been spent in heat transfer and fluid
flow enhancement of the process for heat removal from small surface areas under high
heat flux conditions such as high heat flux electronic chips and high current density
electrical equipment. Although compared to single phase and boiling flows the
phenomenon of condensation is less studied, there is a sizable and growing volume of
literature available in two-phase condensing flows, mostly in conventional tubes. In a
thermal management loop, the heat is dissipated from the target surface to the liquid. If
the fluid changes phase then it has to be condensed by air or another cooling medium.
Often the cooling is done with air. In such a case, since the air-side thermal resistance is
significantly high, even when extended fin or louver-enhanced surface area is provided to
the air-side, most recent research efforts have been spent in reducing the air-side thermal
resistance through various enhancement techniques. Meanwhile, a more effective heat
transfer on the refrigerant side means less volume/weight for the whole system. With the
advent of miniaturization of components due to various reasons, chief amongst which is
the cost, volume, weight and portability, compact condenser designs involving micro-
channels and micro-port flat tubes have been sought after by the refrigeration, air-
conditioning and automotive industries. This need has spurred studies in internal flow
condensation in mini- and micro-channels. Still, at the present moment, the body of

experimental and analytical literature on condensing flows in small diameter channels is limited.

Detailed and up-to-date surveys of literature condensation in general were reported by Garimella et al. [63] and Ghiaasiaan [64]. However, in the present chapter, a brief review of relevant literature related only to flow condensation in small diameter channels will be discussed. Since heat transfer and hydrodynamics of two-phase flow are strongly linked, predictive models on condensation involve the understanding of the complex flow regimes that exist in a micro-channel. Hence a brief review of the literature on flow regime studies in adiabatic and condensing two-phase flows is relevant and will be made.

2.2 TWO-PHASE FLOW REGIMES

Before the details on flow regimes in mini- and micro-channels are discussed, the issue of what should be regarded as a mini- or micro- channel is needed to be understood. This topic has been discussed by different researchers and there is a general agreement that when the channel size starts to influence the flow pattern, heat transfer and pressure loss gradients in a way not found in conventionally studied tubes/channels, it needs a different treatment. Thus, the broad term 'micro-channel' refers to those channel sizes for which the relative importance of gravity, interfacial shear, surface tension start to become different than that for 'macro-channels' or certain mini channels. At smaller channel sizes, the influence of gravity is less (but not necessarily negligible) and the surface tension and viscous forces emerge as dominant players in determining the flow pattern. This is a broad distinction between micro- and macro-channels. A more nuanced

categorization can be made by making the distinctions between mini-channels (relatively larger sized channels, typically 1 to 2 mm in hydraulic diameter, but still distinctly different than the 'macro-' category), micro-channels (smaller in diameter than mini-channels; less than 1 mm hydraulic diameter) and the extreme of the range, sub-micron channels (where the continuum regime is no longer applicable). Serizawa et al. [1] conducted steam-water and air-water flow visualization studies in a micro-channel with hydraulic diameter 50 µm and recommended that the capillary length scale, given in Equation 2.1 below should be greater than the hydraulic diameter of the channel for it to belong to micro-channel category.

$$L_c = \sqrt{\frac{\sigma}{g(\rho_l - \rho_g)}} \qquad (2.1)$$

This parameter captures the competition between the surface tension and the buoyancy forces. In air-water studies, where the surface tension is strong, the micro-channel diameter limit will be higher than that for the refrigerant like R-134a. There is yet another parameter similar to the above and is termed as Confinement Number, Co, which essentially is the ratio of the capillary length scale to the hydraulic diameter ($Co = L_c/D_h$). Kew and Cornwell [2] had recommended that if Co > 0.5 then the flow is truly influenced by the hydraulic diameter. This can be understood for a channel in which, in order to keep the forces in balance, it is necessary that a single bubble, not multiple bubbles, occupies the entire cross-section of the channel at any instant. In practice, a survey of the mini- and micro-channel literature indicates that such strong demarcation in categorization is not used by researchers and the term micro-channel is sometimes, incorrectly, included to mean channels having sizes slightly larger than 1 mm hydraulic diameter. Specifically, in case of high aspect ratio rectangular channels, one of the

dimensions may be of several millimeters long while the other dimension may be about a few hundred microns. In such case, there is gravity effect if the longer side of the channel cross-section is aligned with the gravity vector and the effect is less significant when the other side is so.

Unfortunately, because of its relative simplicity in technique, most of the flow regime studies for two-phase flows have been conducted with adiabatic flows in which the gaseous component is typically chosen as air or nitrogen and the liquid component as water or oil. There are parallels between such flows and condensing two-phase flows. However, the surface tension and gravity effects are significantly different. For example, the ratio of densities of air to that of water is about 1:1000 where as for a refrigerant fluid such as R134a the vapor to liquid density ration is in the range of 1:200. Similarly, the surface tension effects (and contact angles with respect to the channel material) could be significantly different. Also, the effect of momentum change in condensation, when gas molecules enters the liquid encountering reduction in velocity, is absent in adiabatic studies. Hence in the present discussion, the condensing flows in relatively small diameter conventional channels and micro-channels will be discussed.

2.2.1 VOID FRACTION

Void fraction models express relationships of the void-fraction (α_g or simply α) to the flow quality (x). Void fraction is a parameter that describes the mixed nature of two-phase flow and can be described as the time-averaged fraction of the cross-section of the channel occupied by the gas phase at a given location. A good model for void fraction is a useful component in the analysis for a one-dimensional flow in which one

momentum equation can be solved for fluid for a given void fraction. In condensing flows, in general, the void fraction decreases along the length of the channel because of the decrease in the quality. However, in order to obtain a physically appropriate model for the void fraction, the actual physics of the flow should be taken into account. In the different correlations proposed so far for condensing flows, the void fraction calculation relates to the slip between the two phases.

Butterworth [3] proposed the general form of the more widely used void fraction models:

$$\alpha = \left[1 + A\left(\frac{1-x}{x}\right)^p \left(\frac{\rho_g}{\rho_l}\right)^q \left(\frac{\mu_l}{\mu_g}\right)^r \right]^{-1} \tag{2.2}$$

The constants in this relationship differ from model to model and are summarized for some of the commonly used models in the Table 2.1.

Table 2.1: Constants for various void fraction models of the form proposed by Butterworth

Correlation	A	P	q	r
Homogenous Flow	1	1	1	0
Lockhart-Martinelli (1949)	0.28	0.64	0.36	0.07
Baroczy (1963)	1	0.74	0.65	0.13
Zivi (1964)	1	1	.67	0
Thom (1967)	1	1	0.89	.18

Comparison of Void Fraction Models Commonly Used
(R134a at T_sat=50C)
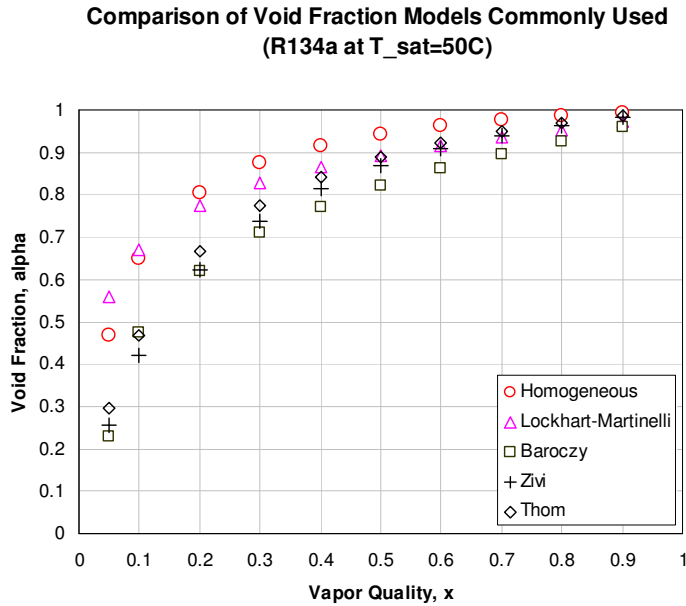
Figure 2.1: Variation of void fraction with quality for different commonly used models

Several other researches have also used the model given by Smith [4]:

$$\alpha = \left[1 + \left(\frac{\rho_g}{\rho_l} \right) \left(\frac{1-x}{x} \right) \left(0.4 + 0.6 \sqrt{\frac{\frac{\rho_l}{\rho_g} + 0.4 \left(\frac{1-x}{x} \right)}{1 + 0.4 \left(\frac{1-x}{x} \right)}} \right) \right]^{-1} \tag{2.3}$$

Smith stated that this model is useful for different flow regimes, mass fluxes, qualities etc. parameters.

A related parameter of interest similar to void fraction is the volume fraction β, which is the time-averaged fraction of gas/vapor volume at a specific location. The homogeneous void fraction, $\alpha_{Homogeneous}$ is same as β. The slip ratio, S_r, which is the

ratio of the average velocities of the gas core and the liquid, is related to the void fraction (Premoli [5]) by:

$$\alpha = \frac{x}{x + S_r(1-x)\left(\rho_g / \rho_l\right)} \qquad (2.4)$$

As mentioned before, majority of the work done in experimental studies on void fraction have been performed in air-water systems and therefore not readily applicable to condensation situation. However, mention should be made for some of the novel techniques that have been made use of in these studies. For small diameter channels (between 1 and 5 mm), Kariyasaki [6] measured void fractions and proposed empirically derived models of the measured void fraction as a function of β. Mishima, Hibiki and co-researchers [7, 8] made several publications in which they used a novel neutron radiography technique to measure the void fraction profile in 1 to 4 mm diameter channels and found that their data is in good agreement with that of Kariyasaki et al. Triplett et al. [9, 10] had used image analysis technique, whereas Rezkallah and co-workers [11] had used non-intrusive capacitance-type probe to measure void fraction in micro-gravity environment. Kawahara et al. [12] also used image analysis technique to measure void fraction of nitrogen and pure water or water-ethanol mixtures in millimeter and sub-millimeter channels and concluded that the millimeter channels follow homogeneous flow model. They have used different concentrations of ethanol to study the effect of fluid properties on void fraction but concluded that such effect was not significant. Thus, a variety of techniques and understanding have been developed in void fraction studies. However, as mentioned before, more research related to actual condensing flows is needed.

2.2.2 FLOW REGIME ANALYSIS

Several researchers in the past have studied condensation in macro-sized tubes and have attempted to give the transition criterion from one flow regime to the next through various flow parameters. Table 2.2 depicts some of these studies on condensation flow regimes and the choice of the transition parameter(s) used by the various researchers.

Table 2.2: Summary of important Condensing Flow Regime Analysis

Researcher	Parameter(s)	Relationship form	Remarks
Traviss-Rohsenow [13]	Film Reynolds No. $Re_l = G(1-x)D/\mu_l$ Froude No. $Fr_l = V^2/g\delta$ Galileo No. $Ga_l = gD^3/\nu_l$ Martinelli Parameter, X_{tt}	$Re_l = f(Fr_l, Ga_l, X_{tt})$	$Fr_l = 45$ marks the boundary between annular and stratified wavy, slug and plug flows.
Breber et al [14]	Wallis' $j_g^* = Gx/(Dg\rho_g(\rho_l.\rho_g))^{0.5}$ Martinelli Parameter, X	Titel-Dukler type flow regime map with axes j_g^* and X	Different combinations of j_g^* and X gives annular, Wavy/Stratified, Slug and Bubbly Flows.
Sardesai [15]	Modified Froude $Fr^* = Fr.(\rho_v/Gx). U_{GS}$ Martinelli Parameter, X Chisholm two-phase multiplier, ϕ_g	$\phi_g^2.F = K$, constant	$K=1.75$ is lower limit of annular flow, $K=1$, start of gravity flow
Soliman [16]	Film Reynolds No. $Re_l = G(1-x)D/\mu_l$ Martinelli Parameter, X_{tt} Film Thickness Parameter, δ^+ Azer two-phase multiplier, ϕ_g Galileo No. $Ga_l = gD^3/\nu_l$	$Re_l = f(Fr_l, Ga_l, (\phi_g/X_{tt}))$	Various data sources used. Annular to wavy/intermittent flow transition at $Fr=7$.
Soliman [17]	Weber No. We Azer two-phase multiplier, ϕ_g Superficial gas & liquid Reynolds No. Re_{GS} & Re_{LS} Martinelli Parameter, X_{tt}	$We = f(Re_{GS}, \phi_g, X_{tt}, etc..)$ at different Re_{LS}	Various data sources used. $We<20$: always annular $We>20$: always mist
Tandon et al. [18]	Wallis' $j_g^* = Gx/(Dg\rho_v(\rho_l.\rho_v))^{0.5}$ Smith's void fraction, α	Similar to Breber et al. with axes j_g^* & $(1-\alpha)/\alpha$	Different combinations of j_g^* & $(1-\alpha)/\alpha$ gives spray, annular, wavy, slug, plug flows.
Wang et al. [19]	Mass Flux, G Quality, x	Flow Map with axes G & x	$50<G<700$ kg/m^2.s studied at different saturation temperatures and for different refrigerants. Flow transitions criteria given in the flow map.
Dobson and Chato [20]	Modified Superficial Vapor Velocity, $j_g = j_{g,Mandhane}.(\rho_g/\rho_{air})$ Superficial Liquid Velocity, j_l	Mandhane (1974) Map was created with air-water studies. Hence the j_g needed correction.	Exhaustive condensation studies in 3 to 7 mm for different refrigerants and blends, and wide mass flux range $25<G<750$ kg/m^2.s Detailed description of flow regime changes for different G and x. Found very good agreement with *corrected* Mandhane Flow Map.
Coleman and Garimella [21, 22]	Mass Flux, G Quality, x	Flow Map with axes G & x	Very detailed study of condensation of R134a in round, square and rectangular tubes at different qualities with $1<D_h<4.9$ mm and $150<G<750$ kg/m^2.s. Effect of Hydraulic diameter and channel shape on flow regime

			was notable.

Amongst the different flow regime analyses tabulated here, the works of Dobson and Chato [20] and Coleman and Garimella [22] deserve special mention due to thoroughness of their studies. Especially, the latter work, which encompasses various tube shapes and tube hydraulic diameters and which includes a wide range of test conditions, is significant and creates a strong reference for further studies. Some of the salient observations noted by them are given below:

- Four major flow regimes, annular, wavy, intermittent and dispersed were identified. Within each major regime, different patterns/mechanisms were discernible. For example, in the annular regime, mist, annular ring, wavy ring, wave packet and annular film patterns were visible. These various patterns are evidence of the balancing influences of gravity and interfacial shear.

- Apart from overall flow regime maps for a particular tube at different mass flux and quality values, flow regime maps with G and x as axes have been erected to specifically show the effects of tube hydraulic diameter for square tubes (separately for intermittent and annular flow regimes) and tube shape effect at similar hydraulic diameters (for flow regime transitions).

- For overall flow pattern map for a particular hydraulic diameter, the regions for major regimes and within each regime, the regions of different flow patterns were identified.

- The flow map for studying effect of hydraulic diameter on square tubes indicates that with decreasing D_h, the region of intermittent regime is reduced. This effect is

significant at lower mass fluxes: 150<G<400 kg/m^2.s. The effect was attributed to the fact that at smaller hydraulic diameters, the surface tension effect is more significant because it is easier to collect and retain liquid condensate in the corners. Thus the transition from intermittent to wavy/annular region occurs at higher qualities. Also, at larger hydraulic diameters, the annular flow tends to be wavy flow with discrete waves visible in the bottom condensate pool; the top condensate layer was relatively thinner than the bottom pool.

- As hydraulic diameter decreases the wavy flow regime is increasingly replaced by annular regime since the surface tension tends to stabilize the flow.

- In case of flow map for effect of tube shape, it was noted that the square and rectangular tubes tend to hold condensate at the corners and hence at a given mass flux, the transition from intermittent to wavy flow regimes was found to occur in their cases at qualities lower than that for round tubes. In this respect the behavior of rectangular tubes was found to be in between square and round tubes.

- In conclusion, the effect of the tube hydraulic diameter was found to be stronger than that of the tube shape.

In summary, although a wealth of investigations have been generated in flow regime mapping, only a few available literature, mostly involving diameters > 3 mm have been available that involves condensing flows. The flow maps created by Coleman-Garimella [22] provide a starting reference and guidance for future studies involving higher aspect ratio micro- and mini-channels.

2.2.3 MINI- AND MICRO-CHANNEL HEAT TRANSFER AND PRESSURE DROP STUDIES

Table 2.3 summarizes the available experimental literature that is relevant to the present work. As seen in this table, there is only a limited sub-set of work that concern channels with hydraulic diameter < 1 mm and some of them involve enhanced surface features such as micro-fins. A brief discussion on some of the more relevant publications amongst these will be given here.

Yang and Webb [23, 24] employed a modified Wilson-plot technique to obtain data for plain and micro-finned tubes with a somewhat high mass flux range relative to the refrigeration and air-conditioning applications typically found. Their data indicate enhancement of the heat transfer coefficient with micro-fin features although the enhancement effects decreased for the upper ranges of mass fluxes. The heat transfer coefficient also showed a weak dependence on the heat flux and the authors attributed this to increased contribution of the momentum effect at higher heat fluxes.

Table 2.3* Summary of experimental condensation literatures in horizontal channels with D_h < 3 mm

Researcher	Channel Dimensions & Features	D_h (mm)	Fluid	T_{sat} (C)	G (kg/m^2.s)
Yang and Webb [23, 24]	Smooth, Micro-fin, Horizontal, MP	2.64, 1.56	R-12	65	400-1400
Zhang [25]	Smooth, Horizontal, SP-C, MP-C, MP-R	6.25, 3.25, 2.13, 1.45, 0.96, 1.33	R134a, R22, R404a	40, 65	200-1000
Webb and Ermis [26]	Smooth, Micro-fin, Horizontal, MP, R	0.611,1.564, 0.44,1.33	R134a	65	300-1000
Garimella and Bandhauer [27]	Smooth, Horizontal, MP-S.	0.76	R134a	51.7	150-750
Wilson et al. [28]	Micro-fin, Horizontal, Flattened	1.84, 4.4, 6.37, 7.79	R134a, R410a	35	75-400

Koyama et al. [29]	Smooth, Horizontal, MP, R	1.11, 0.807	R134a	60	100-700
Wang [30]	Smooth, Horizontal, MP-R	1.46	R134a	61-66.5	79-760
Baird et al. [31]	Smooth, Horizontal, SP-C	0.92, 1.95	R123, R11	20-72	70-600
Cavallini et al. [32, 33]	Smooth, Horizontal, MP-R	1.4	R134a, R236ea, R410A	40	200-1400
Kim et al. [34]	Smooth, Horizontal, SP-C	0.691	R134a	40	100-600
Bandhauer et al. [35]	Smooth, Horizontal, MP	0.506, 0.761, 1.52 mm	R134a	-	150-750

*Note: Based in part on Cavallini [33]; MP- Multi-port, SP-Single port, R-Round, C-Circular

The main mechanism for micro-fin enhancement, which was notable at low mass fluxes and higher qualities, was believed to be due to drainage of the condensate film from the tips of the fins towards their bases. At higher qualities, the fins are submerged in condensate and therefore were not able to provide enhancement.

Koyama et al. [29] conducted a study on condensation of R134a in two 865 mm long extruded multi-port tubes, one with 19 ports (D_h =0.807 mm) and the other with 8 ports (D_h =1.114 mm). The effective length is 600 mm for each tube with the balance length used to provide access to the pressure ports. Local heat transfer coefficients were measured using heat flux sensors for 75 mm length sections. The authors acknowledged that it is very difficult to accurately measure the local heat flux using Wilson plot method or by temperature rise in the coolant especially for small channels such as these. Limited data identifying individual test points were provided; however, the data has been presented in form of comparison with heat transfer and pressure drop correlations. The Nusselt number correlation used by them is of the form of a root-sum-square of the

annular and stratified Nusselt numbers obtained from Haraguchi et al. [36]. In addition to this modification, they had adopted the formula for two-phase multiplier proposed by Mishima-Hibiki [37], because the correlations proposed by these authors were best able to predict their data. Even then, their Nusselt number comparison graph showed significant over-prediction of the data; interestingly, the over-prediction was found to be higher for the tube of diameter 1.114 mm rather than for the 0.807 mm. Moser [38] correlation was found to be a better predictor for the smaller diameter tube than the larger one although for lower mass fluxes (<300 kg/m^2.s) the correlation gave significant under-prediction.

Cavallini et al. [32, 33] conducted measurements of heat transfer coefficients and pressure drop in a multi-port flat tube with 1.4 mm port hydraulic diameter using R134a and R410A. The test section was divided into three segments to provide quasi-local conditions for their measurements. They converted the saturation temperature changes into pressure drop values and found reasonably good agreement with correlations by Friedel [39], Zhang and Webb [25], Mishima-Hibiki [37] and others. However, they found that their heat transfer coefficient data was under-predicted, especially at higher heat fluxes, by several available correlations, most notably by those proposed by Moser et al. [38], Zhang and Webb [25], Cavallini et al. [40] and Koyama et al. [29]. The reason proposed for this was that at higher mass fluxes, a tendency of mist type flow was possible. Also, most of the available correlations come from larger diameter tubes with annular flow features.

Garimella and Bandhauer [35] implemented an interesting thermal amplification technique to mitigate the issues of low heat duties due to low mass fluxes and high heat

transfer coefficients. The local condensation heat transfer rates were measured within ±10%. The heat transfer coefficient values reported by these authors were for 0.506, 0.761 and 1.520 mm circular tubes with R134a as the working fluid. However, heat transfer coefficients beyond 85% quality have not been. In general, the data indicate an approximately linear trend between heat transfer coefficient and local quality, within the reported quality range. For the lower mass flow rate cases such as 150 and 300 kg/m^2.s, the proper distinction was not possible to be made between heat transfer coefficient of the higher and lower mass fluxes, since the difference lie within the data uncertainty.

Baird et al [31] implemented thermo-electric coolers for the purpose of local heat flux measurement in their study with 0.92 and 1.95 mm circular channels at different heat and mass fluxes for R123 and R11. Their data, unlike that of Yang and Webb [23], indicate a rather strong influence of heat flux and a weaker influence of the saturation pressure on heat transfer coefficient. Very little influence of the tube diameter was observed in their operating range.

2.2.4 ANALYTICAL MODELS

So far very few studies have been observed which concern the modeling of the two-phase condensing flows. Notable among them are the studies of Begg et al. [41] and by Wang and Rose [42, 43]. Begg et al. [41] have studied the physical and two-dimensional mathematical model of annular film condensation in mini circular tubes with the vapor and liquid flows coupled through interfacial heat flux, shear stress, and pressure jump conditions due to the surface tension effects. In their model an equilibrium stable annular flow is assumed to occur with saturated vapor flow at the inlet and liquid

completely filling the tube at some distance from the tube's inlet end. In their mathematical model, they have adopted the Munoz-Cobo et al.[44] interfacial shear stress formula meant for annular film condensation in vertical tubes with non-condensable gases, and friction factor as proposed by Wallis (1969). To validate their model, they created a thermo-siphon loop made with Pyrex® which circulated water vapor into test section. The test section consisted of three kinds of tubes with diameters 3.4, 2.3 and 1.6 mm with a thermally insulated flow development region prior to the condensing section. Quasi-static annular flow pattern was observed and the pattern was found to be steady except when non-condensable gases were believed to be present within the test setup. One interesting observation in the predicted film thickness profile was that at the end of the annular flow where the liquid film collapses to form fully liquid flow, the film thickness suddenly decreases before increasing again. Also, in the flow visualization studies, the film thickness seems to increase (for smaller diameter tubes) before decreasing and increasing again (to converge into the liquid pool). It was not clear if non-condensable elements in the vapor were responsible for this phenomenon.

Wang and Rose [42, 43] have studied a truly three dimensional model of annular condensation in circular, square, rectangular and triangular channels at millimeter scale. In their model they considered effects of gravity, surface tension, and shear. For non-circular cross-section tubes, they employed cylindrical coordinate system for the condensate film in the corner regions and Cartesian coordinates for flat edges. The condensation momentum loss effect (suction) was modeled after the approach proposed by Mickley et al. (1954) (as described by Kays, Crawford and Weigand [45]) and the interfacial friction factor (zero transpiration) was taken of the form proposed by Churchill

[46]. The effect of the film curvature along the axial direction was neglected. This is an issue where the condensate film tends to converge giving an error in the prediction for total condensation length. Due to competing effects of surface tension and gravity, the film thickness was not found to be uniform at different points on the perimeter at a given location. This would cause a non uniform heat transfer coefficient at different locations of the perimeter. In their graphical comparison of average heat transfer coefficient profiles along the axis for different geometries, significant differences were observed for rectangular and square geometries against circular geometries. In fact, near the vapor entrance, the rectangular geometry indicates 50% better heat transfer coefficient at the flow conditions they considered. This is a promising result.

2.3 SUMMARY

In this chapter, a brief summary of available literature on study of various aspects of condensation in mini- and micro-channels has been presented. The relevant literature, broadly classified into void fraction related studies, flow regime analysis and flow condensation heat transfer and pressure drop studies has been summarized. In the end, a brief summary of few available analytical studies have been made.

Chapter 3

OBSERVATIONS FROM PRELIMINARY FLOW VISUALIZATION &
NUMERICAL STUDY

3.1 INTRODUCTION

In the present chapter, preliminary flow visualization and preliminary numerical (CFD) study of bubble flow hydrodynamics will be presented. The visualization studies were designed to obtain preliminary information about the flow process in a micro-channel, such as prevailing flow regimes, issues in test setup preparation etc. and were not meant for rigorous investigation of the condensation phenomenon with care for accuracy. In the same light, the preliminary numerical study of bubble behavior has been made to understand the flow simulation process and its potential as well as its limitations.

3.2 DESCRIPTION OF EXPERIMENTAL SETUPS AND VISUALIZATION

3.2.1 MICRO-CHANNEL ARRAY VISUALIZATION

Two experimental setups were used in the preliminary study of condensation. In the first setup, shown in Figure 3.1, a micro-channel test prototype (Figure 3.2) was installed. In preparing the test prototype, the wire-EDM (Electro Discharge Machining) process was employed to machine sixty-eight micro-channels in a brass block with overall dimensions of 30mm × 30mm. Each channel was 250 μm wide and 400 μm deep (hydraulic diameter 0.31mm) with a wall of 175 μm between adjacent channels. The micro-channels were covered from the top using a Plexi-glass® plate sealed along the sides with rubber gasket. Visualization of the condensation of vapor occurring in these micro-channels was achieved through this Plexi-glass® cover. The condenser was water-cooled from below as shown in Fig. 3.2. The micro-evaporator has similar geometry but

had twenty channels and an overall channel array dimension of 10mm × 10mm. Heat was supplied to the evaporator by means of a rod-shaped electrical heater embedded in the brass block underneath the channel structure.
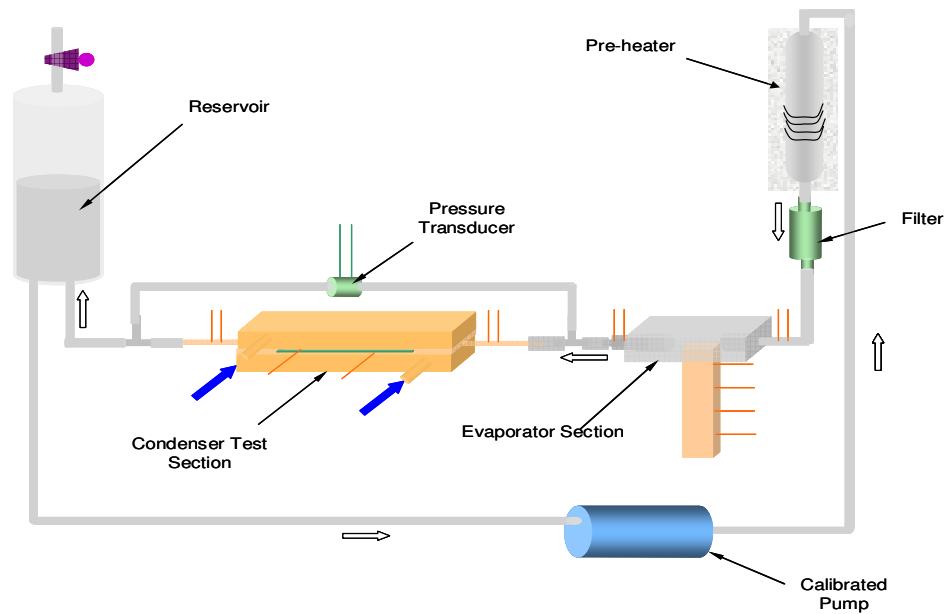
Figure 3.1: Schematic of the test loop for testing the EDM-machined Micro-condenser
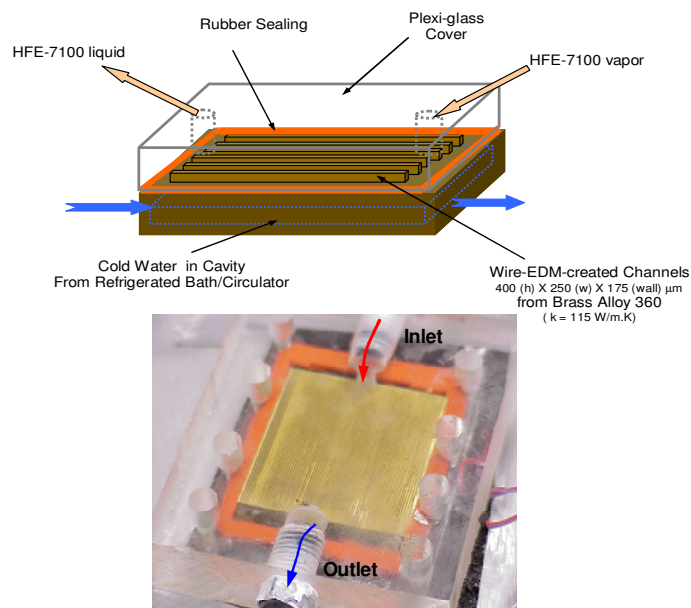
Figure 3.2: (Top) Schematic of the test prototype (Bottom) Photograph of the assembly from above

HFE-7100 was used as the working fluid since there is an active interest to use this fluid for electronics cooling applications. Also, HFE-7100 is liquid at room conditions and was useful in this present case since the test setup was not designed for pressurized refrigerants.

Saturated vapor inlet condition was not applied to the condenser due to the concern that the evaporator might experience 'dry out' condition in the high heat duty process and the evaporator heater might get burnt. Only medium to low condenser inlet qualities were used for sample tests. The EDM-machined micro-condenser, in one such test, exhibited heat removal capacity of 26 Watts at a flow rate of 134 kg/m^2.s at a saturation temperature close to the room condition (25C). The pressure drop across the test channel at this flow rate was 800 Pa. A heat transfer coefficient of 2900 W/m^2-K was achieved at an inlet vapor quality of 0.24. Further, it was observed that at higher mass fluxes, the bubbles in the two-phase flow entering the condenser inlet, tends to concentrate in the few channels near the middle of the channel array due to flow inertia. Also, the distribution of the entrant bubbles in the inlet header section was significantly influenced by the tilt angle of the test prototype with respect to the gravity vector. Thus, although the channels were sufficiently small for gravity to have an effect on the flow after it entered the channel, the effect occurred in the header section itself. (With this knowledge, the interconnect design described in Appendix A.4 was provided with web features to direct the two-phase flow evenly across the array of the channels.). Upon entering the channel, the two phase flow took the form of plug flow pattern, with a typical vapor bubble between two liquid plugs diminished in volume (due to vapor condensation) as the flow proceeded along a channel towards the exit. Small flow

oscillations were observed for all flow conditions tested. These oscillations could be inherent to the flow process.

3.2.2 SINGLE MICRO-CHANNEL VISUALIZATION

A second test setup was based on the thermo-siphon concept, similar in configuration to that used by Begg et al. [41] for the validation of their mathematical model. A schematic of this test setup is shown in Figure 3.3 and its actual photograph is presented in Figure 3.4. The reason this setup was chosen for a preliminary study was primarily because of its simplicity, and also in order to confirm and better understand the authors' visual observations.
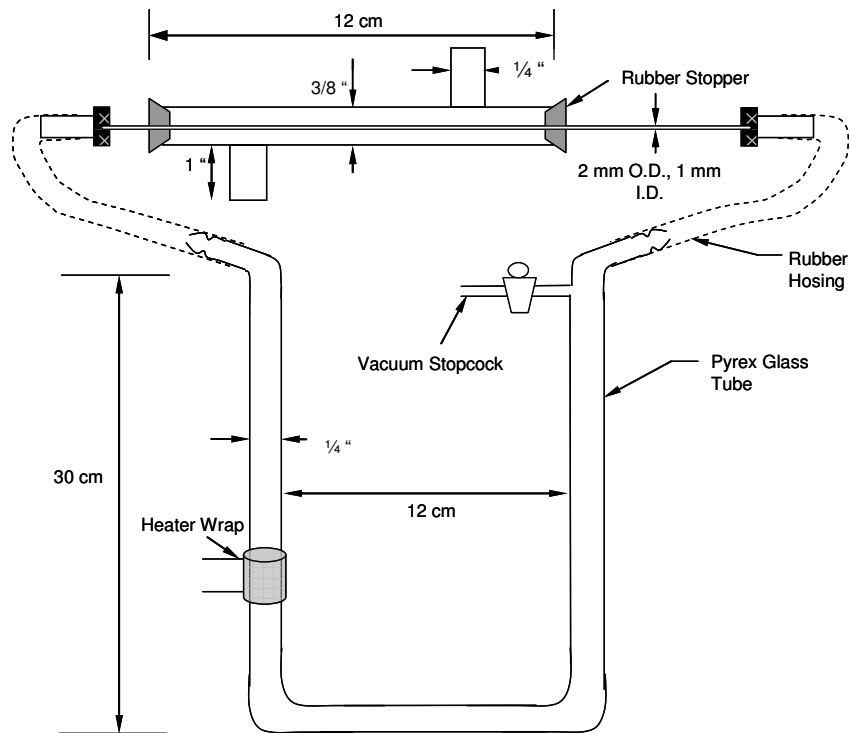
Figure 3.3: Schematic of the visualization Test Setup, constructed similar to that used by Begg et al [41].

The main apparatus in this setup was the Pyrex® U-tube with a tube-in-tube capillary condenser connected to its either end by means of flexible rubber hosing. The tube-in-

tube condenser consisted of a cylindrical Plexi-glass water jacket with inlet and outlet ports for coolant water flow. The coolant flow was countercurrent to the flow of condensing refrigerant in the capillary. The capillary was also of Pyrex® construction with inner diameter 1 mm. The effect length of the condenser was 12 cm. To one of the arms of the U-tube apparatus a heater wrap was affixed with heat conductive adhesive. The other arm of the U-tube was provided with a port equipped with a vacuum valve for charging and discharging of the working fluid. As in the previous case, the fluid chosen for the study was HFE-7100. To operate the test setup, first the coolant flow was started and then slowly the voltage input to the heater was increased to allow heat to dissipate into the liquid. The heat input was kept sufficiently low to allow evaporation from the surface of the liquid pool in the U-tube arm but to discourage violent boiling activity which might destabilize the condensation process in the capillary by introducing pressure fluctuations along the inlet path.   During operation of the loop, the pressure drop across the flow channel could be estimated from the difference of the levels of liquid in each arm of the U-tube and calculating the gravitational head there-from.

A test was conducted with heater power input of 4.95 Watts. It was observed that the condensation process, once established and stabilized, had an annular flow pattern with a net condensation length of 37 mm. However, the end of the vapor core where the condensate liquid film converges and marks the beginning of liquid-only flow was oscillating continually back and forth along the tube axis and small vapor bubbles were getting injected into the liquid flow. This unstable behavior of the oscillating liquid vapor meniscus was observed even at lower heat inputs, but with a lesser amplitude. In recent literature, some references to this kind of flow have been made. Chen and Cheng [47] had

observed this behavior in their study of condensation of pure steam in an array of micro-channels with hydraulic diameter 82.8 µm. In their study, the annular flow typically ends with 'injection flow' when, intermittently, parcels of vapor mass at the head of the annular core, get separated from the core, and get injected into the liquid condensate due to oscillation of the meniscus.
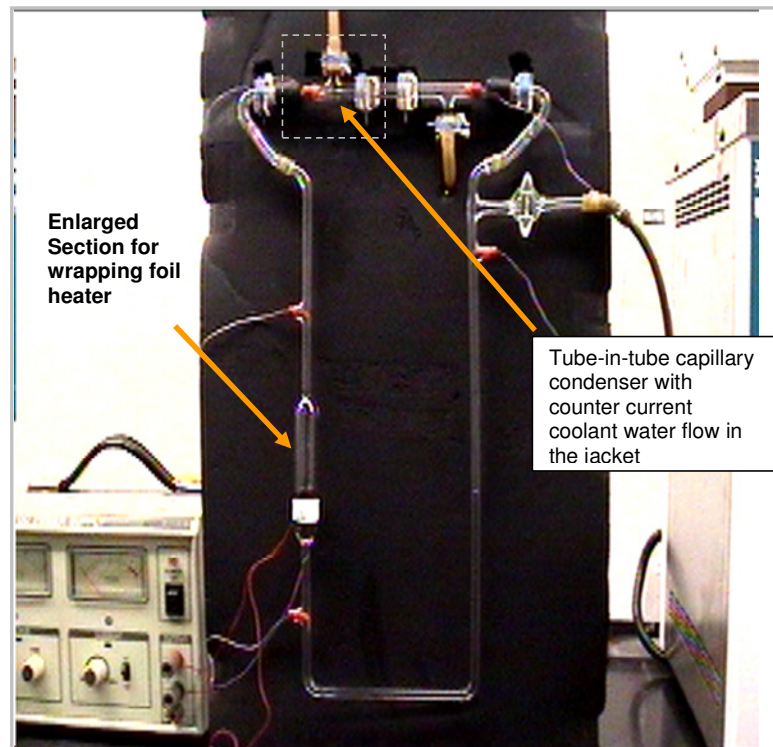
Figure 3.4 Photograph of the thermo-siphon visualization test setup

3.3 DISCUSSION ON OBSERVATIONS IN THE PRESENT PRELIMINARY STUDY

Three issues were apparent from the observations from these two test setups. First, it would be difficult to detect and control the uniformity of flow distribution if an array of parallel micro-channels were used for more rigorous study. Secondly, even if a single micro-channel was used, there remained the possibility flow-induced oscillations. Thirdly,

thermo-siphon mechanism would not be a sufficient driver for the flow in the loop, and an additional pump would be needed, if higher mass-flux cases were to be investigated.

3.4 CFD STUDY OF A BUBBLE MOTION BY VOLUME OF FLUID (VOF) APPROACH

Under low and moderate mass flux conditions and low local qualities, where liquid and gas flows would both be laminar, an intermittent flow regime had been found to operate in small hydraulic diameter micro-channels by Coleman and Garimella [22]. This intermittent regime flow is of the pattern of discrete plug and slug flows, such that elongated capsule like bubbles, separated from each other by pure liquid slugs and from the channel walls by a thin liquid film were found to exist. These elongated bubbles are often termed as Taylor bubbles, and have been subject to scrutiny by different authors such as Nijhuis et al. [48], Taha and Cui [49, 50, 51], van Baten and Krishna [52], Zheng et al. [53] and others, who employed CFD analysis to understand the hydrodynamics of these bubble motions under adiabatic conditions.

Here, a brief description of the findings from a similar effort in characterizing different bubbles in motion in a circular channel with hydraulic diameter 1 mm and R134a at saturation temperature of 50C is provided. In this work, an adiabatic condition had been studied due to the lack of a comprehensive model for interfacial mass transfer that could be implemented in this numerical procedure.

3.4.1 PROBLEM FORMULATION

A Volume of Fluid (VOF) approach to solution of the flow field was adopted. The CFD software FLUENT (version 6.3.26) was used to model the problem. VOF

model is able to track the motion of two immiscible fluids in contact. It solves a single set of momentum equation and the interface between the fluids is tracked based on the volume fraction of each fluid in each computational cell, throughout the computation domain. Thus in case of a gas-liquid flow, a cell having $\alpha_g = 0$ is completely in the liquid phase, where as those cells having $\alpha_g = 1$ is in the gas phase. Those cells with $0 < \alpha_g < 1$ are in the interfacial zone between two the fluids. The details of the CFD model can be obtained from Fluent® User's Guide [54].

A 1 mm diameter circular tube was chosen for the study so that a 2D axially symmetric domain, 0.5 x 10 mm, could be simulated with a high mesh density, taking into account the limitation of available computing power. Figure 3.5 shows the details of the computational domain. The mesh density chosen for this study was 50 (X) x 500 (Y). In order to enable the simplification of study by having the three dimensional problem solved with 2D axially symmetric flow, gravity was not chosen to participate in the problem.

The domain was initialized to a fully liquid state except for a region around the axis having specification of full vapor. The initial shape of this vapor region that was chosen was similar to the axial cross-section of a cylinder with hemispherical caps to aid rapid convergence. Any other shape (encompassing same vapor cross-sectional area) would eventually lead to similar steady state shape, but would require more computation time.
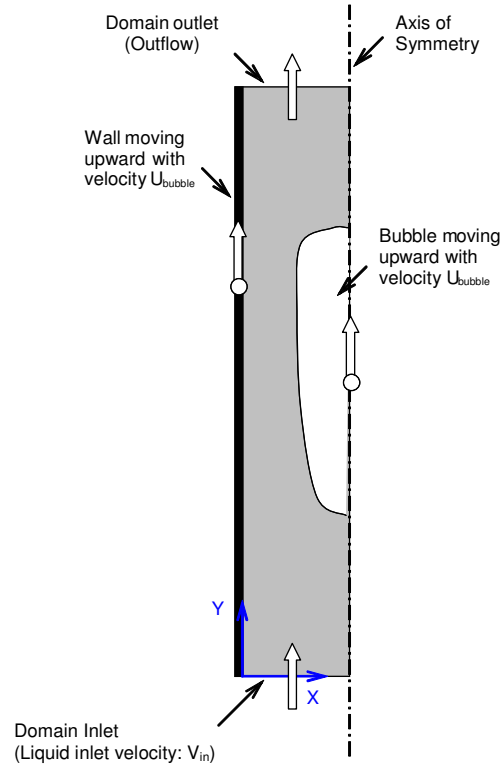
Figure 3.5: Schematic describing the flow domain for simulation of a Taylor Bubble

Since the inlet liquid mass flow rate forces the bubble to rise in the Y-direction, in order to capture the evolution of the bubble, the wall was given a fictitious velocity, equal in magnitude and direction as that of the bubble, so that the bubble would appear stationary with respect to the wall. The steady state bubble velocity was unknown and hence the wall velocity, initially set to an arbitrary guess value, was continually updated in small increments by observing whether the bubble was moving relative to the wall as iterations through flow time were progressed. Courant number, which determines the solution time step, was set to 0.25 for unsteady iterative solution.

3.4.2 RESULTS AND DISCUSSION
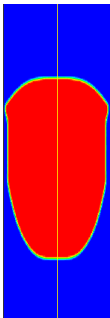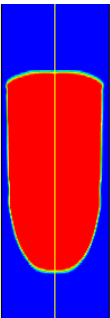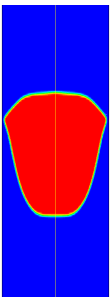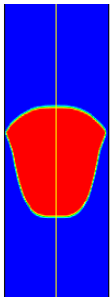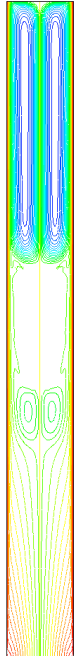
The results of this preliminary CFD model are presented in Table 3.1. As seen in the table, two aspects of bubble motion were studied, namely,

(a) effect of mass flux, and

(b) effect of bubble volume

on the bubble shape and the flow pattern in the liquid plug upstream and downstream of the bubble. Four different model conditions were chosen for this brief study. For the first two conditions, the bubble volume was kept constant and only the inlet mass flux, G was changed between low and high values (11 and 110 kg/m^{2}s). For the third and fourth conditions, the same flow state was studied with smaller bubble volume.

For all diagrams, the flow was from the bottom towards the top, as depicted in Figure 3.5. For the larger bubble volume, the influence of refrigerant mass flux on bubble shape and liquid flow pattern was clearly visible. In case of lower mass flux case, the bubble cap was more rounded than that in higher mass flux case. Also, the film thickness increased for larger mass flux case. For lower mass flux, there was a strong toroidal vortex structure ahead of the bubble with a similar but weaker and elongated toroidal structure behind it. As mass flux increased, this latter vortex shrunk in dimension where as the one ahead of the bubble was found elongated to span the entire remaining length of the tube. In case of the smaller bubble volume, both the shape and the flow structures ahead and behind the bubble were almost identical, with little or no effect of the mass flux, at least for the level of mass fluxes investigated here. Also, the bubble velocity, and hence the Capillary number, seems to be unaffected by refrigerant mass flux. This conclusion should to be verified for other bubble volume and mass flux cases.

Table 3.1 Summary of the preliminary CFD investigation on adiabatic bubble hydrodynamics

Steady State Bubble Shape				
Contour of Stream Function in the Flow Domain				
Mass Flux, G (kg/m^2.s)	11.02	110.20	11.02	110.20
Bubble Velocity, U_{bubble} (m/s)	0.17	1.6	0.17	1.6
Capillary Number, Ca= $\mu_l U_{bubble}/\sigma$	4.97×10^{-3}	4.68×10^{-2}	4.97×10^{-3}	4.68×10^{-2}
Bubble Volume (mm^3)	0.6786	0.6786	0.3958	0.3958

It must be borne in mind that only single bubble motions had been studied here. In reality, in case of plug/slug flows, a train of bubbles are present. In such a case, the flow structure ahead and behind a particular bubble at a particular mass flux would have strong similarity due to periodicity of the problem.

With regards to the phenomenon of condensation, the interesting aspect of the present study was the insight into the vortical structures ahead and behind a moving bubble. It may be easily understood that due to this motion, the liquid particles were continually brought from the liquid layers adjacent to the channel wall into the main flow stream. This would cause an enhancement in the wall heat transfer. Taha and Cui [51] also cited the earlier findings that the slug flow structures enhanced the radial mass transfers in reactors with catalytically active walls and in case of blood flow, the vortical motion of the blood plasma ahead and behind a red blood corpuscle augmented the distribution of nutrients. In Figure 3.6, the velocity vector map inside and around a larger bubble in motion for the higher mass flux case is shown. The colors of the vectors reflect the phase of the fluid. It can be seen that there was a vortex structure present inside the bubble as well, which might contribute to the heat transfer enhancement, especially if the bubble contained superheated vapor inside. Due to the vortical structures present both inside and ahead/behind a bubble, the modeling of heat and mass transfer through the bubble cap and tail and through the cylindrical side surfaces need to be modeled differently. The heat and mass transfer through the side surface may be expected to be of stronger influence since the liquid film around the bubble is of minimum thickness here and also the liquid motion is fastest in this region. However, as visible from the shape of the bubbles for smaller bubble volumes, the cylindrical bubble surface is not present.
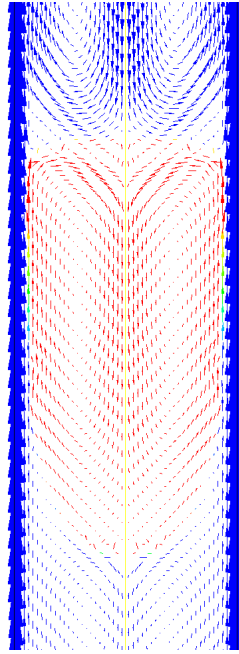
Figure 3.6: Velocity vector map inside and around a bubble (G=110.2 kg/m^2.s and Bubble volume=0.6786 mm^3)

In closing this preliminary study, it should be mentioned that in the present case the flow studied is adiabatic with zero mass exchange between the two phases. In case of actual condensation phenomenon, there is a net heat and mass transfer from the vapor to the liquid phases with a corresponding change in momentum. This issue has not been addressed here. A detailed note is provided in Chapter 8 concerning the lack of a confident understanding/model of the interfacial heat and mass transfer. If such a model is established, the present study can be made to include those effects to better reflect the real situation.

3.4 SUMMARY

In the present chapter, three preliminary studies have been presented – two experimental and one numerical CFD-based – with a view to understand and gain confidence in the condensation phenomenon in micro-channels as applicable to the functioning of a compact multi-channel condenser. In the experimental studies, the issues of flow maldistribution and flow oscillations were highlighted, and in the adiabatic numerical study of bubble hydrodynamics, the vortical flow structures inside the vapor and liquid regions were identified as factors that may be influencing the heat and mass transfer. The study also clearly suggests the need for more detailed flow visualization investigation that can realistically represent the actual situation.

Chapter 4

DESIGN AND FABRICATION OF A MICRO-CHANNEL CONDENSER IN A

SILICON WAFER USING MEMS TECHNIQUES

4.1 INTRODUCTION

In this chapter, a brief account of activities in relation to design and fabrication of a micro-channel condenser in a silicon wafer has been provided. The objective was to create a compact two-phase forced convective cooling loop with components made with the same material as that of a microchip, i.e. silicon. Silicon micro-channel evaporators for heavy duty electronic chips and such other high heat flux application have been widely reported in literature. Compact micro-pumps, driven variously by electric current and suitable for the above application were reported as well. Therefore, to bring a closure to a complete compact thermal management loop, the feasibility study of a micro-condenser made from a silicon substrate was felt to be needed. If such a condenser was found possible to conveniently fabricate, then the condenser, evaporator and micro-pump can all be fabricated on one silicon substrate within a small footprint, thereby eliminating the necessity of separate interconnections between these components.

4.2 MICRO-CHANNEL CONDENSER DESIGN

The aim of this design was to etch micro-channel structures onto silicon wafers by bulk micromachining techniques. As shown in Figure 4.1, the design consists of wafer-wafer bonded micro-channel structure supported at ends but fluidic interconnects. Two possible varieties are shown in this sketch – the first one having one wafer bearing the channel feature and capped with a blank wafer, and the second one having the channel

structure on both wafers and are bonded after the channels are aligned with each other and contacted. Clearly, the level of complexity in creating the second variety was more since it involved alignment issues that needed to be dealt with by means of an some intra-red camera technique such that the channel structures would be 'visible' through the back side. As a first attempt, the design having a blank wafer cap was studied.
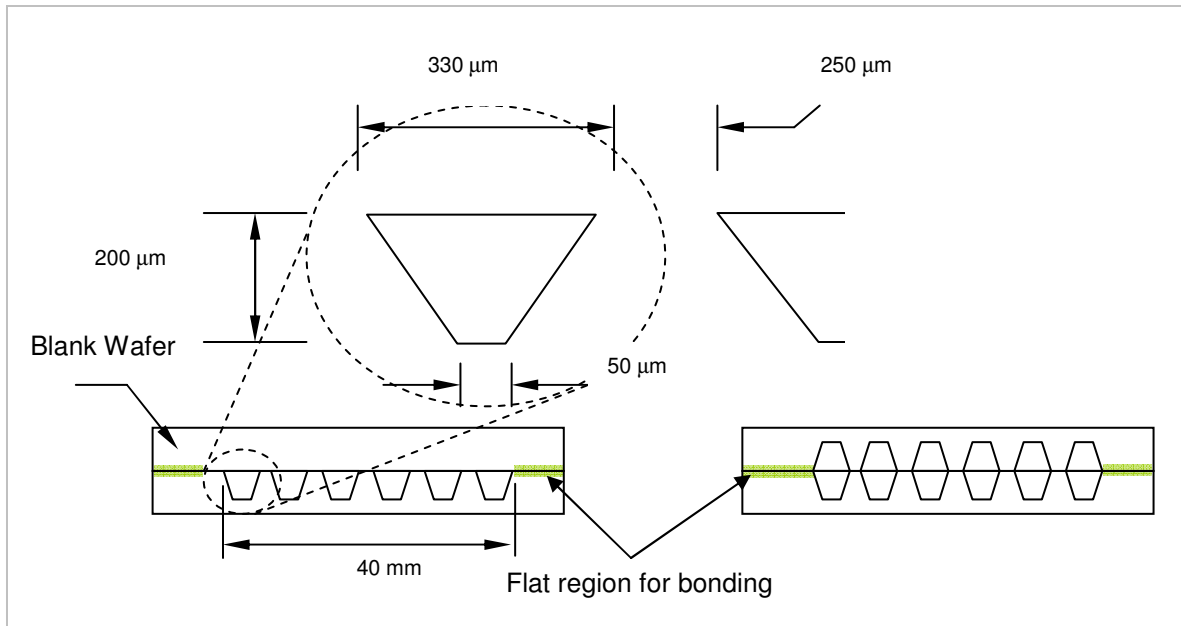
Figure 4.1: Cross-section details of silicon micro-channel condenser

For development purposes, bulk chemical etching of silicon is selected for its flexibility and cost issues. Initially a cavity width of 500 μm, depth of 350 μm and wall width of 100 μm was chosen to maximize heat transfer area. However, it was found that due to fabrication and handling limitations, the resultant wafers were damaged. A revised design with reduced cavity width of 330 μm, depth of 200 μm and wall width of 250 μm were selected as the final design parameters. The channels are 64 mm long and there are 68 channels in the array with an overall width of 40 mm.

Channels or grooves can be etched in silicon wafers by either deep reactive ion etching (DRIE) or anisotropic wet etching techniques. High aspect ratios channels can be fabricated more conveniently by DRIE than by wet etching, since DRIE produces vertical channel walls, whereas wet etching generates angled sidewalls, as illustrated in Figure 4.2.

| (a) | (b) |
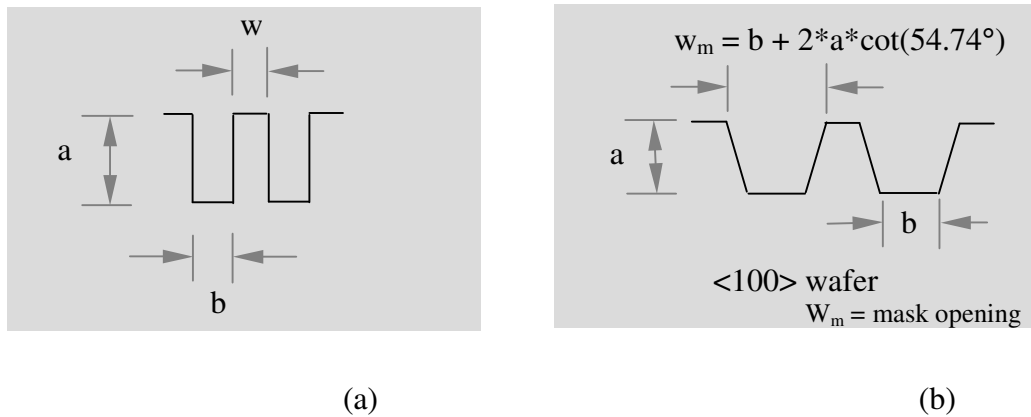
Figure 4.2: Geometry of the cross-section of channels by (a) DRIE and (b) anisotropic chemical etching

4.3 FABRICATION METHODOLOGY & RESULTS

4.3.1 PROCESS STEPS

Based on the above design, a set of standard 4 inch diameter and 525 μm <100> polished silicon wafers with pre-deposited 0.1 μm silicon oxide (SiO_2) and 0.3 μm LPCVD silicon nitride (Si_xN_y) were purchased. Photolithography was performed using a standard 5 inch-square chrome-on-glass mask, shown in Figure 4.3. The pattern was developed and cured. Next Reactive Ion Etching (RIE) was performed to produce a channel pattern on the silicon oxide – silicon nitride layer. Subsequently, the wafer was

immersed in an aqueous potassium hydroxide (KOH) solution, a standard silicon etchant, in a constant temperature etch bath. The etching medium was an aqueous solution of 44% KOH (by weight) at 80 C. The measured etch rate was 1.4 µm/min and etch was performed for 160 minutes. Towards the end of the etch process, the etch rate was found to reduce. Figure 4.4 delineates the various process steps that were carried out in the creation of a wafer with the desired micro-channel pattern. The result of etching is shown in Figure 4.5.
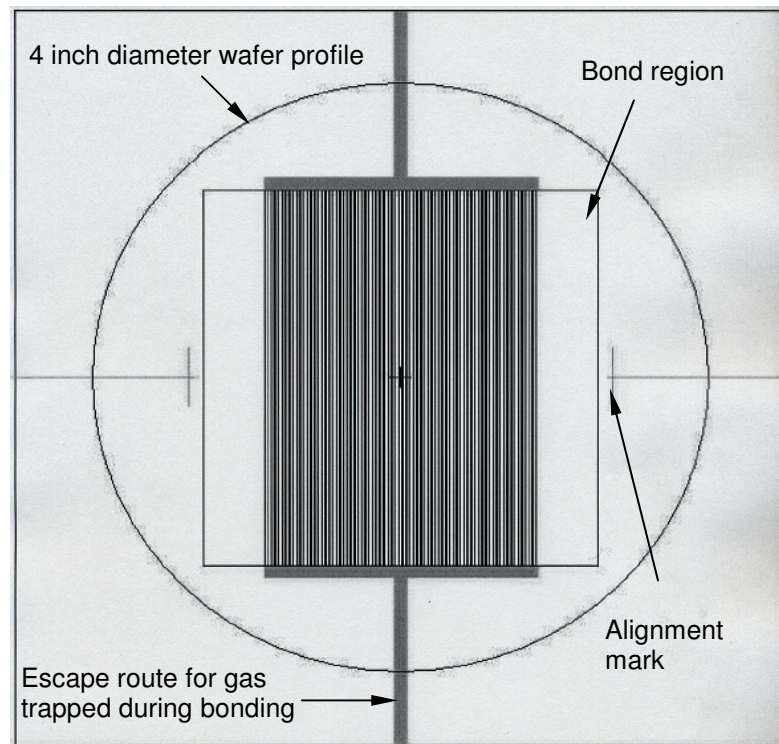
Figure 4.3 Photograph of the mask pattern used for photolithography
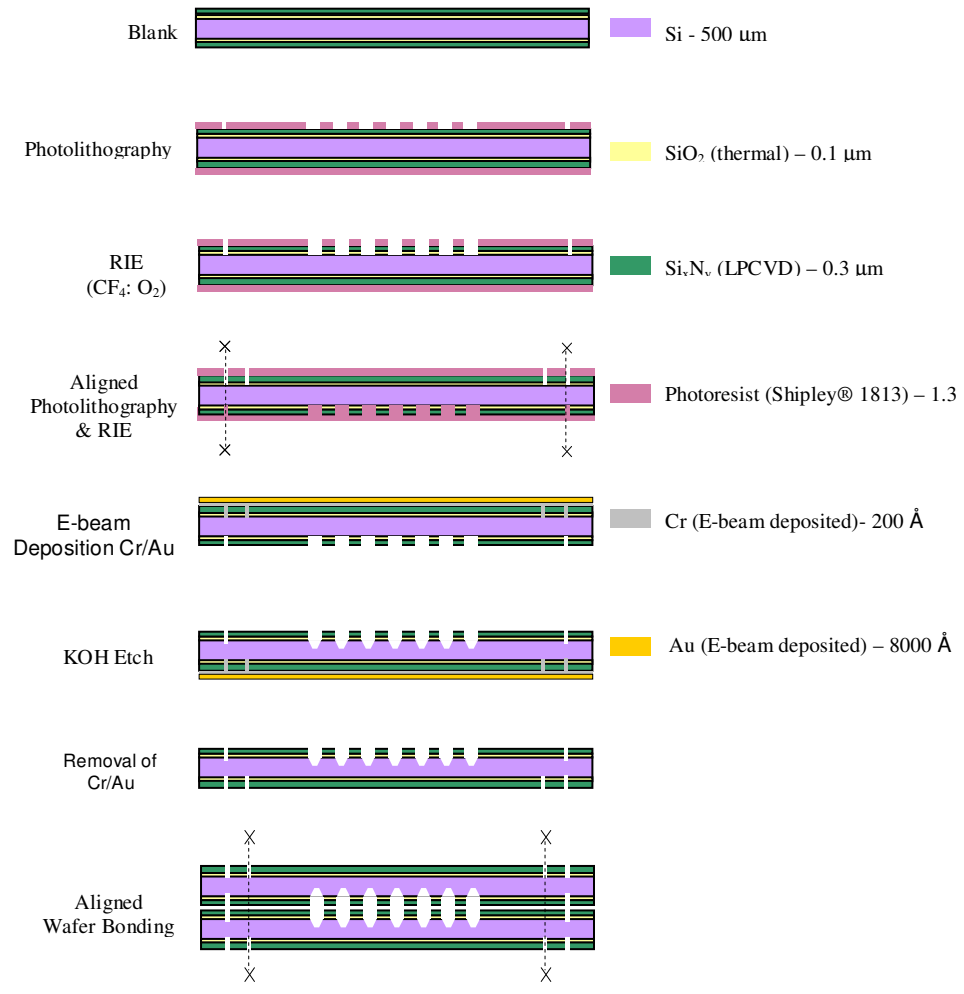
Figure 4.4: Process flow for fabrication of Silicon micro-channel condenser
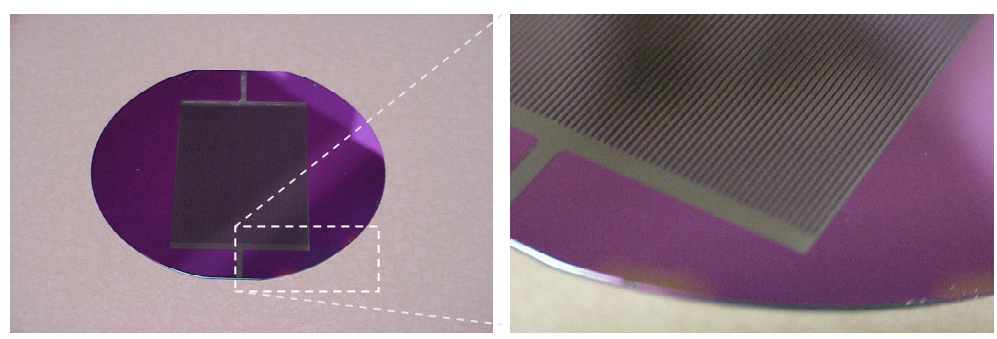
Figure 4.5: (Left) Micro-channel pattern etched on 4 inch diameter <100> Silicon wafer with pre-deposited 0.1 µm Silicon Oxide and 0.3 µm Silicon Nitride (Right) Close-up of the V-groove feature

4.3.2 WAFER-WAFER FUSION BONDING PROCEDURE

Wafer bonding is more commonly applied to Si-Si or SiO_2-SiO_2 layers. However, recent applications necessitate bonding between Si_xN_y - Si_xN_y. This is because silicon nitride, due to its relatively high insensitivity to etching solution can be used as a masking layer (with appropriate patterned openings per design). This eliminates the need for additional mask layer fabrication steps (such as inert gold layer deposition). However, bond strength for the bond between two silicon nitride layers been found to be significantly less than that between bare silicon layers or between silicon oxide to silicon oxide layers. Such a bonding process has been sparingly mentioned in literature (Sanchez et al. [59], Bower et al. [60]). Careful preparation of samples has been reported to result in reasonable bond strength in case of Nitride layers. A suggested mechanism for bond formation is formation of $\equiv$Si-N-Si$\equiv$ covalent bonds across contacting surfaces. Low surface roughness is a significant criterion for good bond strength. Direct bonding at room temperature is possible though it has been seen to produce lower yield strengths. A subsequent step of annealing has been shown to improve bond strength significantly.

The main steps in fusion bonding of wafers were:

(a) chemical cleaning of the wafers to obtain very high surface purity,

(b) hydration of wafer surfaces,

(c) contact bonding of the wafers, also called pre-bonding,

(d) baking of the wafers in a furnace at a high temperature and pressure.

Cleaning of the wafer surfaces prior to bonding was a very crucial step and significantly influenced the bond quality. Because of the high degree of flatness of the wafers, any small particle or impurity at the interface might cause weak bond formation

or voids. Therefore, a pre-cleaning step was necessary. This step involved the established chemical treatment process known as RCA cleaning. The process involved three steps (and three wafers baths) as shown in Table 4.1.

Table 4.1: Wafer Cleaning Procedure (RCA Cleaning)

Step	Step Name	Procedure Details	Procedure/Steps
1	SC-1	5:1:1 of H2O:H2O2:NH4OH @ 70C for 15 mins.	1. Heat Bath; add NH_4OH; add H_2O_2 into hot bath. 2. Add more Peroxide than necessary as it tends to be boiled off
2	HF Dip	50:1 of H2O:HF for 2 mins.	This removes thin layer of SiO2 metallic contaminants tend to accumulate in step 1.
3	SC-2	6:1:1 of H2O:H2O2:HCl @ 70C for 15 mins.	1. Add HCl; Heat Bath; add H_2O_2 into hot bath.

4.3.3 RESULTS

Figure 4.6 shows the first result of fusion bond of wafers as per original design shown in Figure 4.1 (right). The bonding was performed, for demonstration purpose, at a professional foundry facility belonging to an outside vendor, due to the need for wafer aligment. The subsequent samples were tested in-house as per simplified design i.e. Figure 4.1 (left). This simplified design eliminated the necessity of wafer alignment at pre-bond stage thereby rendering the complexity, although it restricted the design to channels of smaller hydraulic diameter.
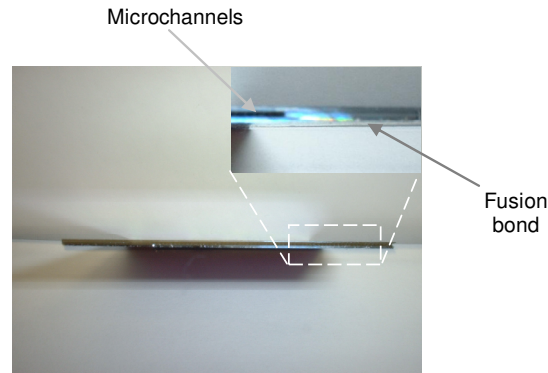
Figure 4.6: Photograph showing result of fusion bond and dicing to create the first prototype micro-condenser

During the in-house process development, the pre-bonded wafers were inspected using an IR-camera-enabled wafer bond inspection system especially designed for the present work. The substrate (silicon) and the nitride and oxide layers permit infra-red radiation to pass through them. If the infra-red rays encountered voids, multiple reflections that occured between the disjoined surfaces, caused visible interference fringes to be formed. These fringes could be observed by means of the IR-camera as shown in Figure 4.7.
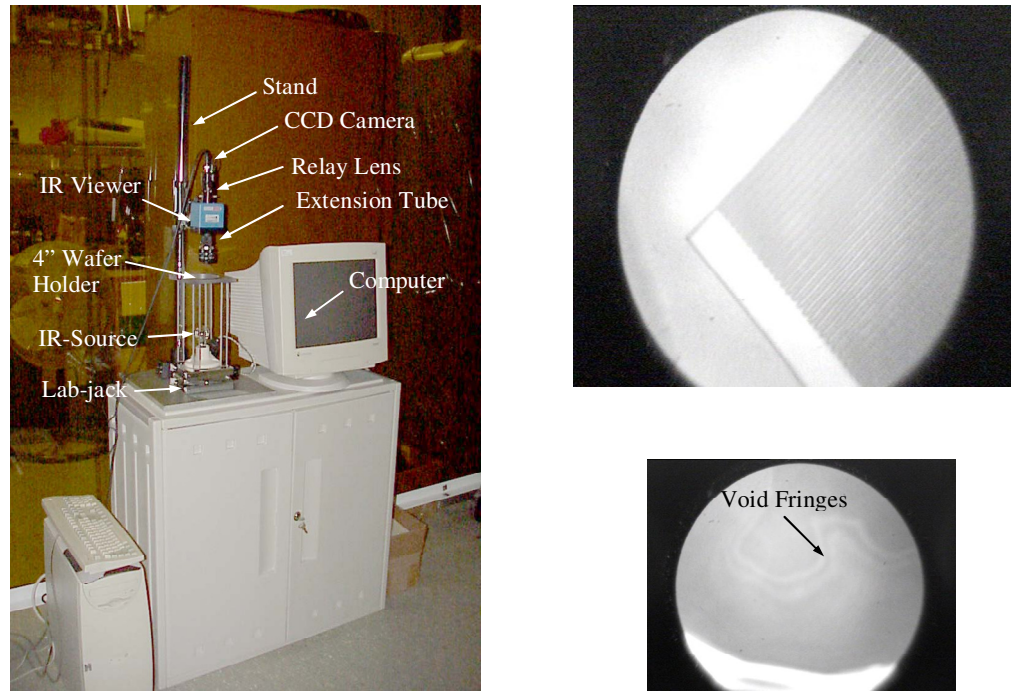
Figure 4.7 (Left) An assembled set-up for inspection of wafer bond quality consisting of an IR-Viewer and a CCD camera for digital capturing. (Right-above) View of sample under microscope (Right-below) Void fringes exhibited around the periphery of void regions

Some samples showed evidence of large void regions, as indicated by the appearance of void fringes in the IR images. Some samples only exhibited small voids at the extremeties of the wafers, so these samples were chosen for subsequent annealing step to complete the bonding. Samples were annealed in a furnace at 1000 C for two hours with a clamping force of about 10 kN. Figure 4.8 shows a sample result of wafer bonding for simplified design produced at the in-house facility.
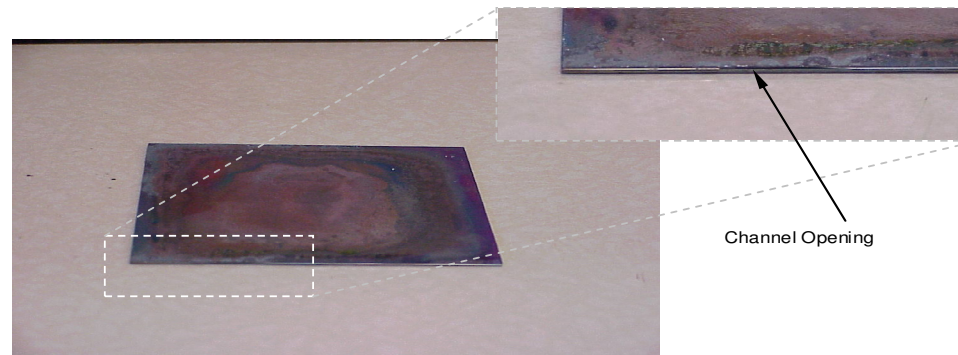
Figure 4.8 Photograph showing the result of wafer bonding for the simplified design

4.4 PACKAGING

Figure 4.9 depicts the packaged micro-channel condenser. Two channeled copper heat sinks were fabricated to encase the micro-condenser channel structure from the two faces. A thermally-conductive paste was used as an interface layer between the silicon condenser and the two heat sinks. Plastic interconnects were specially designed and fabricated by a rapid prototyping process for distributing the fluid to the micro-channels. These interconnects were sealed to the micro-condenser with a layer of epoxy glue.
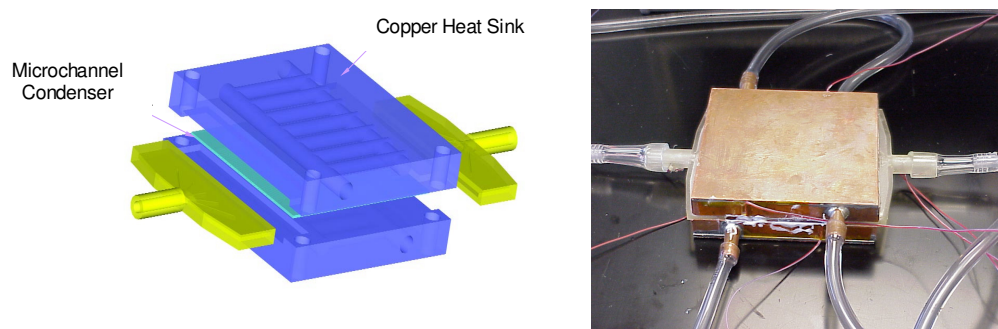
Figure 4.9 (Left) CAD Model showing the package configuration (Right) Photograph of the package.

4.5 CONCLUSIONS AND SUMMARY

In this chapter, a process for Silicon Nitride to Silicon Nitride surface bonding technique was explored to see the viability of this process for the fabrication of wafer stack containing embedded flow structures. It is concluded, that while this fusion bonding process is possible to implement in laboratory condition only under great care for surface purity and surface flatness, by no means, it is an appropriate bonding technique if robustness of the condenser for handling, packaging and testing is desired for. A more convenient and productive technique would be anodic bonding to Pyrex® wafer or bonding of the Silicon Oxide layers which is a proven process but would require additional masking layers such as chrome-gold. Due to the fragile quality that caused breakage of the samples at various stages of the development process, sufficient samples were not available to complete the study of the fluid flow aspects of these micro-condensers. In retrospect, it is also desired that substrate wafers be of at least 1 mm thick each in order to implement 200 µm channel depth without risk of breakage.

Chapter 5

DESIGN AND FABRICATION OF THE TEST SECTION MICRO-CHANNEL

5.1 INTRODUCTION

This section explains the design and fabrication of the micro-channel test section that was used to perform experimental tests to generate condensation data. As explained in the previous chapter, the objective of creating and testing a micro-channel condenser by the bonding of silicon wafers with embedded channel structures was not realized due to the lack of robustness of the designed structure. Some recommendations have been made in the design and the process steps which may lead to a successful product. However, that avenue was not pursued due to a lack of resources and time. Based on the preliminary experiments on EDM-machined metallic condenser test section, as described in Chapter 3, it was felt that the actual condensation phenomenon should be explored in the present work, in order to address the issue of sizing the intended micro-channel array condenser for a particular cooling application. However, as found during the literature study, at the time of this research work, only a few papers were available to describe condensation in a small channel such as desired for the silicon micro-condenser. Hence, a more basic study on condensation of common refrigerants to understand the applicability of the reported correlations to condensation in small hydraulic diameter channels was deemed as the necessary step. Since the present work was intended to be a part of a longer study program, pursuing the design alterations recommended for the fabrication of a micro-condenser was planned to be a future work. Meanwhile the exploration of the basic phenomenon was planned to be completed. For this reason, the remainder of the

present work is devoted to the study of condensation phenomenon in a small hydraulic diameter and high aspect ratio micro-channels.

The objective of the design of the test section was to create a high aspect ratio micro-channel with hydraulic diameter $D_h \leq 750$ µm and aspect ratio: $4 \leq a_r \leq 7$. The rationale for choosing a high aspect ratio was that such aspect ratios micro-channels have been shown to be effective in flow boiling scenarios and can be expected to perform similarly in condensation scenarios as well. Using a multi-port extruded aluminum micro-channel tube, similar to the works presented in most literature, was considered during experimental planning. However, there are several issues related to commercially available multiport tubes. First, as experienced during the preliminary tests presented in Chapter 3, it is difficult to ensure uniform flow distribution in the different ports at the inlet header section. Second, it may not be possible to control the coolant flow outside a multi-port tube such that it uniformly affects all flow channels. Third, it would be difficult to identify the exact locations for inlet and outlet pressure measurements, as entrance losses would be there. Fourth, the fluid flows in the ports would experience different wall temperatures on different sides of their rectangular cross-sections, if high aspect ratio channel is used. Finally, it would be difficult to obtain such a tube with all ports having exact rectangular shapes – typically the end ports of the tube are of different shapes and dimensions than that of the ports in the middle due to extrusion limitations. It must be mentioned here that the major benefit of using the multi-port channels, as opposed to a single channel, is that the total heat transfer value would be few times the value of heat transfer from a single channel under similar inlet mass fluxes and temperature and pressure conditions and hence the error generated due to heat losses (or

gains) and other parasitic effects, being independent of the total amount of heat transfer within the condenser, would possibly be reduced in the multi-port tube case. A single channel test with small error margins was one of the main concerns in the design of the experimental apparatus. Further discussions on the desired error limits, the design of the apparatus, and the control systems to keep error within those limits will be discussed in a subsequent chapter.

5.2 DESIGN OF MICRO-CHANNEL PROTOTYPE

Based on the reasons presented in the previous section, it was determined that a single micro-channel test section would be prepared for the present study. In order to obtain a rectangular cross-section with a high aspect ratio ($7 \leq a_r \leq 10$) and having the hydraulic diameter $D_h \leq 750$ µm, a channel with rectangular cross-section of 400 µm ×2800 µm was created. For this channel, the cross sectional area was A_c = 400.2800 µm^2 = 1120000 µm^2 or 1.12 mm^2 and wetted perimeter was be P_w= 3.2 mm. Therefore, the hydraulic diameter was D_h = 700 µm and the aspect ratio was a_r = 7.0. This satisfied the dimensional criteria.

The next question was the optimal length of this test section. Typical automotive condensers employ multiport tubes with lengths ranging from 300 to 600 mm where as for compact heat exchangers for, say, electronics cooling applications, the length of tubes is necessarily much smaller, and can be up to an order of magnitude smaller than automotive condensers.

There are other aspects to this issue. First, creating a long test section increases the surface area for heat losses; since a single channel test section was to be employed

where the lower margin of the heat transfer rate (for the expected range of test parameters) would be about 10 W only, the amount of heat loss impacts would the significantly affect the accuracy of data . Second, in the case where the channel length is short (viz. 50 mm), similar to the EDM-machined micro-channel discussed previously in relation to the preliminary tests, the surface area available for heat transfer on the refrigerant-side is limited, and hence, in order to accommodate the latent heat transfer from the refrigerant at mass fluxes of 50 to 300 kg/m^2.s, the temperature difference between the wall and the refrigerant need to be significantly high in order to condense a vapor flow at quality 1.0 (or even a 15C superheat) at the inlet to a liquid at quality 0.0 at the outlet of the channel. In order to have such high temperature differences, the coolant needs to operate at temperatures close to or even below the normal freezing point of water (for certain test cases) and thus water could no longer be used as coolant. This would significantly reduce the possibility of using available instruments and chillers in the experimental setup. Furthermore, cold coolant piping has its own issue of heat losses at different ambient conditions and it would be difficult to control such losses in a laboratory environment. Thus, operations at reduced coolant temperatures are difficult to design and also to control. Another problem with using very short test section is that the entrance effects and flow patterns of both the coolant and the refrigerant can be significantly different than the representative cases if the data is to be used for comparison with that from literature. The only advantage of a short test section is that the test section surface area (i.e. coolant jacket area exposed to ambient air) for heat transfer is minimized which could reduce the parasitic heat transfer.

Since the intent of the present experimental study is to aid in the design of compact condenser heat exchangers, a moderate figure of 200 mm was selected for the test channel length. This length is comparable to those used in some of the recent condensation studies (Garimella et al. [35], Begg et al. [41]) of similar micro-channel hydraulic diameters, and hence an additional advantage is that their data can be compared with the present work to check validity of the data from the present work.

Entrance and exit portions of the channel were expanded into a cylindrical flow cross-section to accommodate inlet and outlet tubes of 1/8" O.D. These tubes were stainless steel and thin-walled (0.1 mm wall thickness) to minimize axial heat conduction losses (or gains) from the test section. 1/16" O.D. pressure ports were created 5 mm away from the entrance and exit ends of the channel. Therefore, the effective length of micro-channel flow (from the perspective of the pressure drop measurement), measured from center of entrance pressure port to the center of exit pressure port, was 190 mm. However, the entire 200 mm length is available for heat transfer.

Next the wall thickness of the channel had to be decided. On one hand, a thin walled tube, subject to possible corrosion, could leak or even burst at high refrigerant operating pressures (up to 20 bars). There is also a possibility that the test channel could bulge in the middle and cause intended rectangular cross-section to distort. On the other hand, a thick wall selection could lead to a slightly higher temperature difference between the refrigerant and the coolant and could also be affected by axial conduction. A controlled axial conduction is not entirely without benefit, as it can assist in keeping wall temperature uniform along the length of the test section. An analysis performed in ANSYS indicated that a wall thickness of 2 mm, with for copper as the wall material, is

sufficient to prevent burst and also maintains the intended rectangular shape at elevated refrigerant pressures of up to 20 bars. Figure 5.1 indicates the model in ANSYS for structural analysis. At 2 mm wall thickness, the model indicates that the maximum deflection at the middle of the channel is 4 µm which is 1% of the channel width. This value of deflection is acceptable. If we had a channel with a smaller aspect ratio (i.e. higher channel width), then the deflection might be expected to be even smaller.
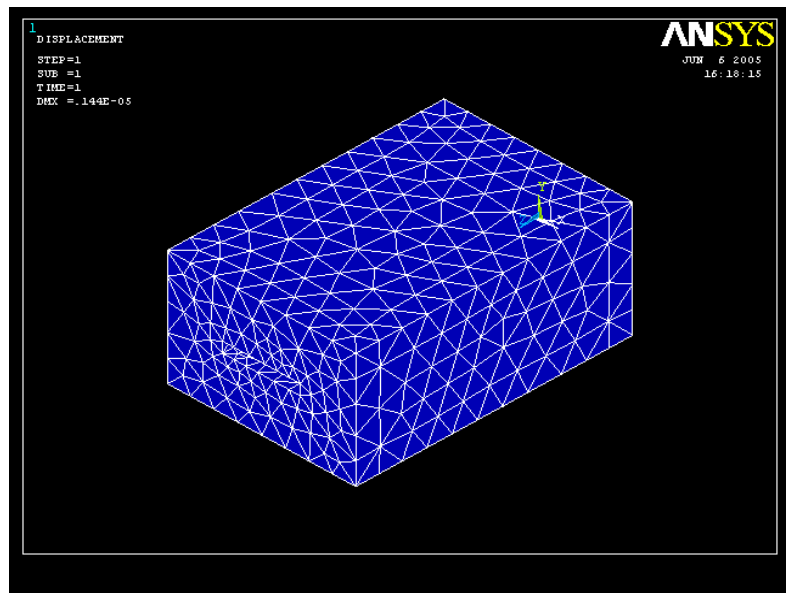
Figure 5.1: An ANSYS model for structural analysis of the micro-channel

Based on these considerations, the final structure was a channel 200 mm x 0.4 mm x 2.8 mm and was created in a bar of copper with dimensions 200 mm x 6.8 mm x 4.4 mm with 2.0 mm wall thickness on all sides of the channel. An exploded CAD model of the micro-channel with design dimensions is shown in Figure 5.2.

Flow Port
1/8" O.D.

400 µm

. Pressure Port
1/16" O.D.

Micro-channel
400 µm x 2800 µm
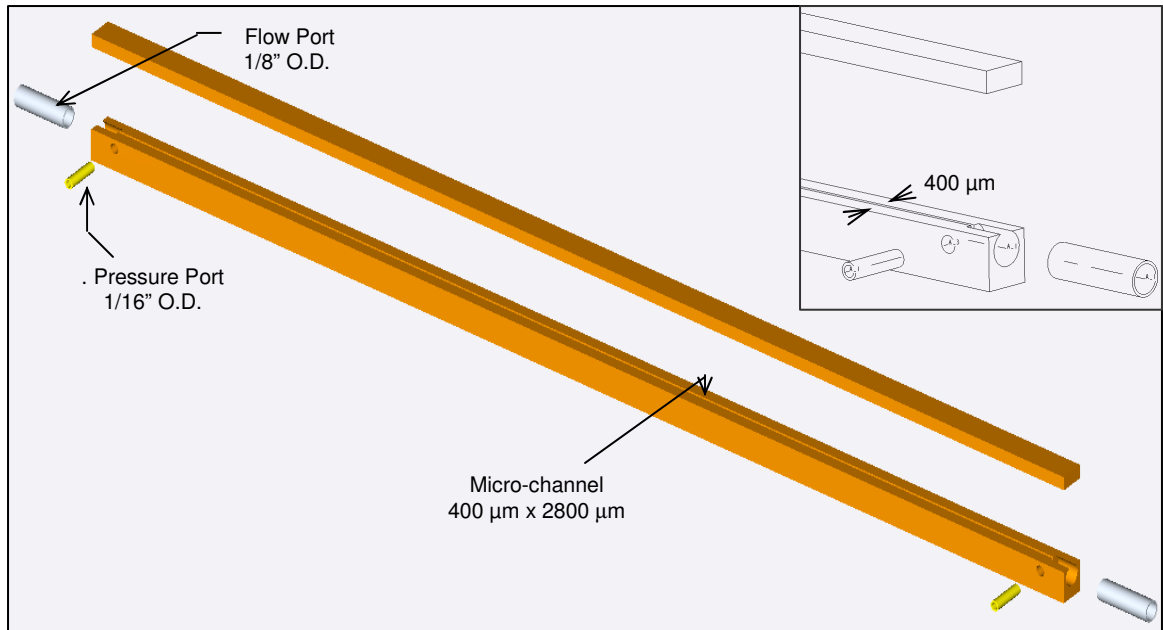
Figure 5.2: Exploded view of CAD model of the micro-channel test section. Inset: Detailed view of channel end

5.3 FABRICATION METHODOLOGY

The goal of the micro-channel fabrication was to create a rectangular cross-section with minimal distortion and to maintain that cross-section straight along the entire length of the channel.

The first step in the strategy for fabrication was to determine whether it was appropriate to create a one-piece channel (as in extrusion) or a two-piece structure (an open groove with a lid) which would be subsequently joined. With a view to create a one piece structure, extrusion process was considered. However, creating a customized extrusion die is expensive. Alternatively, to be a process similar to the fabrication of jewelry, was considered. In this process a wax mandrel was produced and its surface was coated with a thin silver solution, which was electrically conductive. After this solution dried, the mandrel piece was immersed in an appropriate electrolytic bath and the surface

was metalized by electro-deposition. The thickness of deposited metal could be controlled by current and time of deposition. Subsequently, the metalized mandrel was gently heated up to the melting point of wax (70 to 80C) and the molten wax was drained off. As a trial for creating a wax mandrel for the micro-channel, for understanding the challenges that could be associated with this process, a portable extrusion setup was assembled in the laboratory with a controllable motor and screw injector. A trial extrusion die was prepared to study the process controls. Several difficulties presented themselves in this operation. The wax mandrel did not retain the intended shape as wax was found to expand after it passes out from the die. Secondly, it was difficult to keep the 200 mm length of the wax mandrel straight during handling as wax is very pliable. Still a trial electro-deposition of copper was performed in a bath of copper sulphate solution to observe the final outcome. The result at the end of this trial run is exhibited in Figure 5.3.
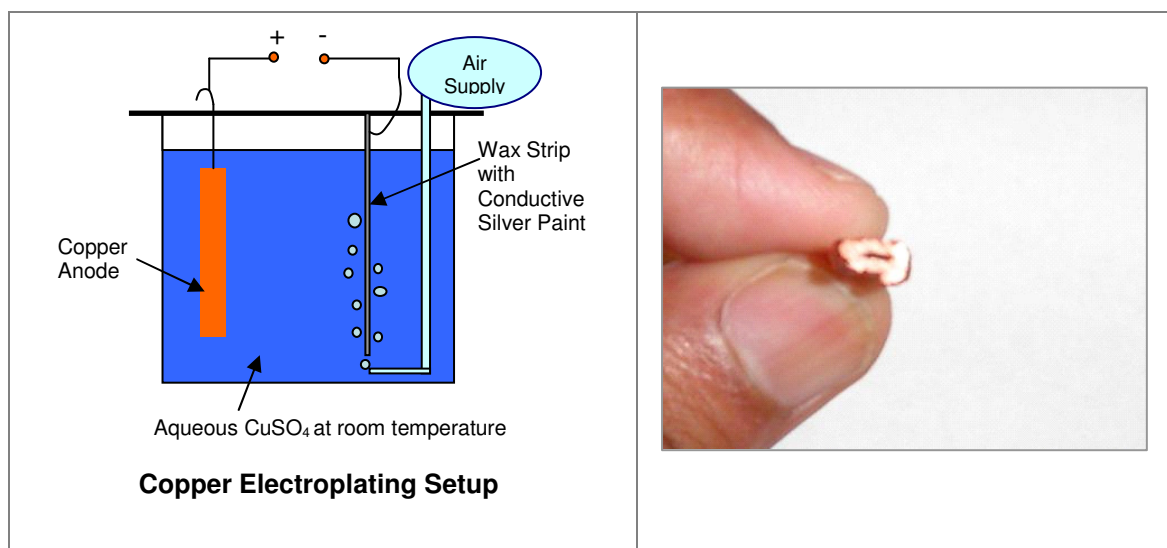
Figure 5.3: *Left* – Schematic of copper electro-deposition setup. *Right* – Result of first trial with wax mandrel.

This channel, created wholly from electro-deposition, had a distorted internal geometry, and the external surface of the channel exhibited uneven nodular formations because the gas bubbles that formed due to the deposition chemical reaction were removed too slowly. A stream of air was introduced, as shown in Figure 5.3 to augment the bubble breakout process. However, it needed significant attention and adjustments to produce smoother external surface of the channel. Although the final outcome was not completely discouraging, it was clear that this process inherently possessed significant logistical challenges and control issues and therefore, was deemed not worth pursuing. Instead, a traditional machining approach would be adequate.

Electro-discharge machining (EDM) was initially thought to be the appropriate machining technique in this situation. The available cutting wire tool had various wire gages ranging from 0.125 mm and higher. However, because the material choice was copper, and because the length of cut was 200 mm it was advised that a thicker wire tool be used to avoid wire breakage. Also, it would be difficult, yet possible, to maintain a 400 μm channel width while avoiding pitting and other roughening features on the side wall. Another reason was that due to the wire tool shape, the channel end profile would be rounded instead of the desired right-angled corners. Although a rounded end would not significantly alter the channel cross-sectional area and hydraulic diameter values, it would still be a defect. Therefore, it was decided that a computer-controlled milling operation would be a simple and appropriate method of channel creation. Further, a 400 μm thick slitting saw blade was available commercially and would be a suitable tool.

After the channel was created by the well-controlled slitting operation, it was inspected for defects and measurements were taken with electronic calipers with

precision of 1 µm. The next step was to create a channel cover. Typically, such channels are covered by brazing of a metal plate. However, it was feared that by such a brazing operation the channel height was not guaranteed to stay at design dimensions. Also the heat applied during brazing could distort the channel shape. It was determined that a more benign approach would be desirable.

The process flow for creating an integrated channel cover is shown in Figure 5.4. Step 1 was the creation of a 4.8 mm x 4.4 mm x 200 mm oxygen-free 99.9% pure Copper blank. A channel 2.8 mm x 0.4 mm was created in this blank (Step 2) by the well-controlled machining process described in the previous paragraph. All oil and other organic deposits were cleaned from the surface of the structure by immersing it in a jar of 10% strength aqueous solution of sulphuric acid. Then structure was cleaned in water and dried, and then jeweler's wax was pressed into this channel (Step 3) to create a protective layer to prevent electro-deposition inside the channel. Prior to Step 4, the inlet, outlet and pressure port tubing pieces were brazed to the channel. Step 4 was a crucial preparatory step involving several sub-steps. First, remnants of wax were carefully scraped off from the top of the channel with a sharp razor blade, leaving the wax filled inside the channel and flush at the surface. Then a wax-dissolving solution was applied on the exposed copper surface using a cotton swab to further dissolve the wax and any organic residues that may contaminate the surface preventing electro-deposition. The remaining three faces of the channel structure were coated with paint to protect them from deposition. Finally, a fine paint brush was used to apply a coating of silver solution on the exposed wax layer so that it was ready to be coated with copper. After the silver solution dried, the structure was placed inside a freshly prepared copper sulphate bath and air flow was

provided using a small air pump to continually remove gas bubbles formed on the cathode surface. The current flow, the temperature of the bath, and immersion time were recorded to ensure desired deposition thickness.
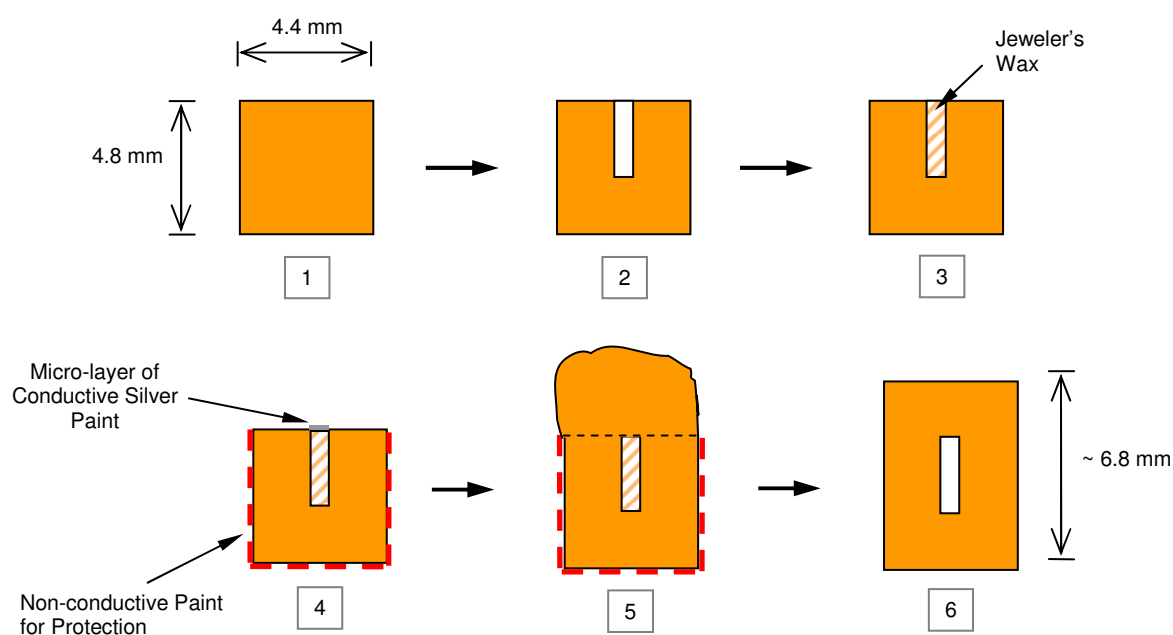
Figure 5.4: Six-step process in machining and closing a channel.

After desired thickness of deposition was achieved, the structure was removed from the bath and the residual solution was cleaned off the object (Step 5). It was observed that some undesired nodule growths began to form from the painted sides of the channel structure, as shown in Figure 5.5. This is because the paint layer, although not electrically conductive *per se*, acts as a weak dielectric layer with certain impurities causing low conduction at certain places. These nodular growths were weakly attached to the object and were broken away by finger pressure. The last step, Step 6, was to clean the wax present inside by passing boiling water through the micro-channel and melting

the wax. As an added precaution, the wax-dissolving solution was also passed through the micro-channel to dissolve any residual wax left in the channel. This brings the process of fabrication to a conclusion.
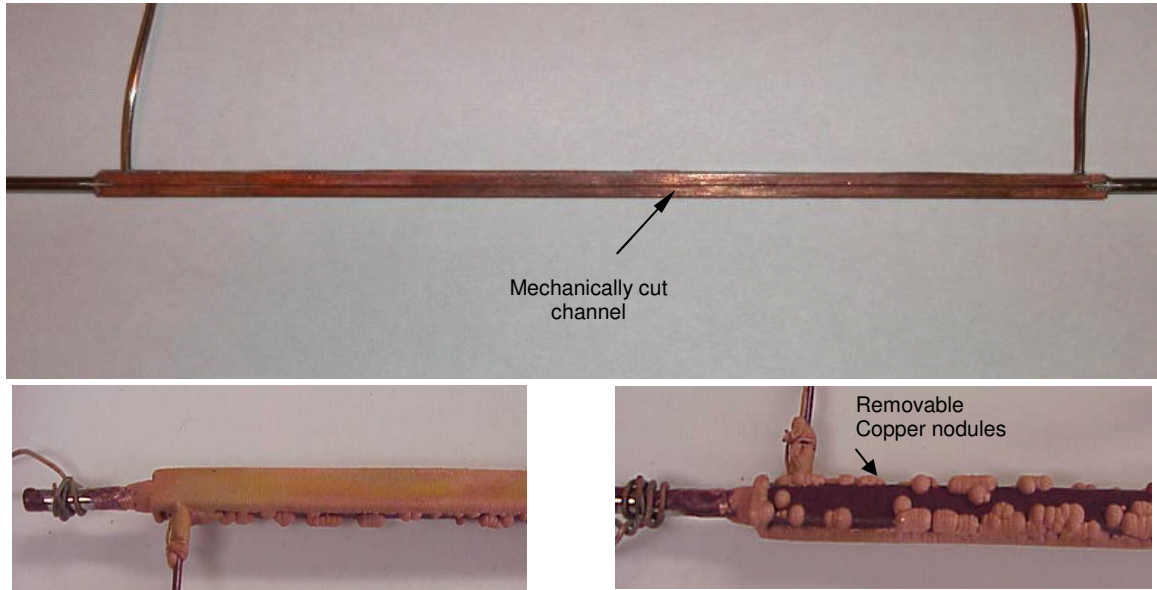
Figure 5.5: *Top* – Micro-channel structure with integrated flow and pressure ports before deposition. *Bottom Left* – Electro-deposited cover. *Bottom Right* – Undesirable but removable nodular growth of Copper on the painted surfaces.

5.4 LEAKAGE TESTING AND VALIDATION OF CHANNEL GEOMETRY

After the channel was created, it was connected to a compressed air cylinder by Swagelok® fittings and was tested for leakage by holding the channel under water and subjecting the channel to an internal air pressure of up to 20 bars. The channel was kept submerged at this condition for several hours. However, no signature of bubble formation was observed, attesting to the integrity of the channel.

Although great care was taken to create channel geometry close to the design of the micro-channel, it was felt that an additional step of validation would be useful. After the test channel was assembled in the test apparatus, as described in the next chapter, a test was run in which liquid R245fa refrigerant at a known temperature, T=23.4 C and

pressure, P=140.7 kPa was circulated in the loop and pressure drop measurements between the inlet and exit ends of the channel were recorded by using a calibrated pressure transducer. These experimentally obtained data were compared with pressure drop obtained from CFD simulation with the FLUENT® software program by creating an exact design model of the channel. This comparison is shown in the graph in Figure 5.6. This corroboration, along with the visual measurements of the channel dimensions after machining operation, provided confidence that the final form of the channel closely matched the design dimensions.
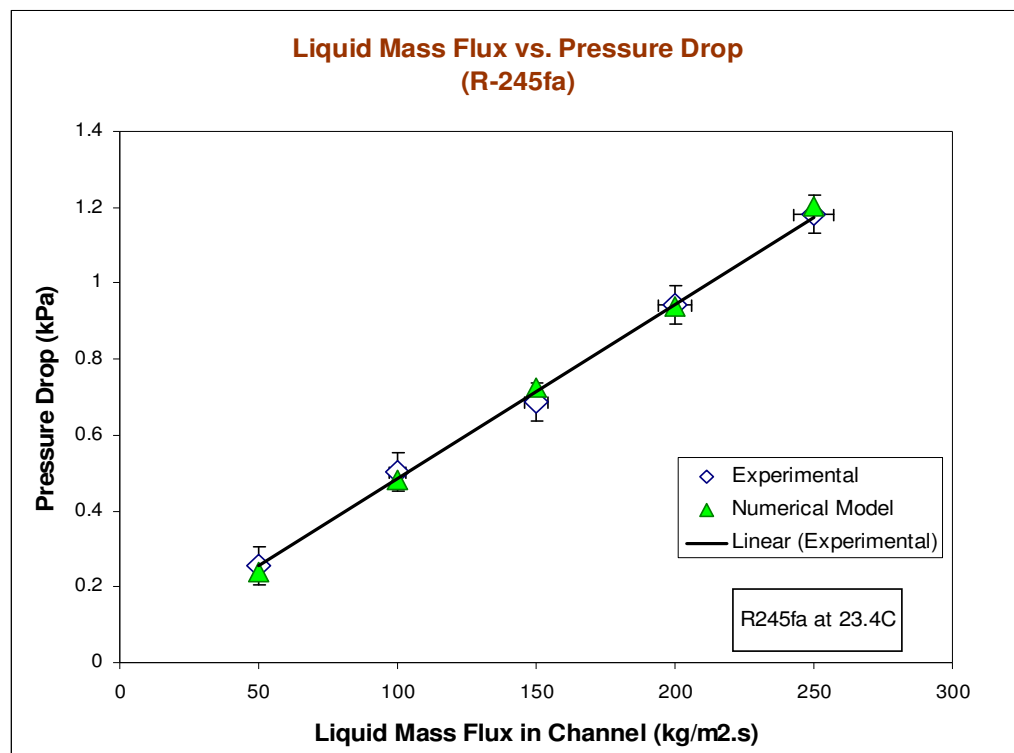
Figure 5.6: Graph of comparison of CFD simulation and experimental measurements of pressure drop across the micro-channel length.

5.5 SUMMARY

This chapter presents the criteria and thought process that led to the design of a non-traditional fabrication method for creating a suitable micro-channel structure for the present experimental work. Data from simulation software tools and adoption of a trial-and-error approach were used to fine tune and/or validate the design and fabrication process. The result was a carefully prepared micro-channel structure with integrated flow and pressure ports that was ready to be incorporated in the test apparatus, described in the next chapter.

Chapter 6

EXPERIMENTAL APPARATUS AND INSTRUMENTATION

6.1 INTRODUCTION

It was necessary for the design of the experimental apparatus was to accommodate condensation tests for two refrigerants – one, a high pressure refrigerant and another, a refrigerant which is in liquid state at temperature and pressures close to room conditions. The selection and properties of the two refrigerants, one of which was determined to be R134a, are discussed in a later section of the present chapter. The setup also needed to operate with R134a at mass fluxes through the channel: from 50 to 300 kg/m^2.s, saturation pressures from 30 to 70 C, and inlet super-heats from 0 to 20 C. These ranges are typical for compact condenser applications. It was also important to contain the mass flux measurement error within ± 5% and energy balance, uncertainty in heat transfer coefficients and pressure drops for each data point within ± 15%. These limits, especially the uncertainty limit on the heat transfer coefficient, are critical since many results in available literature are reported as much as 30 %. It was mentioned in Chapter 5 that because a single channel was employed in this investigation, the heat transfer was about 10 W on the lower side of the heat inputs and such a low value of heat power would be especially subject to error in measurements and uncertainty due to heat losses. Hence it was necessary in the design of the apparatus to counter such errors as far as possible. Also, some of the measurement and instrumentation problems revealed themselves only during the course of study and hence several modifications were made to improve the system after the first configuration was created. The final form of the apparatus is presented here with some developmental notes as necessary.

6.2 DESCRIPTION OF APPARATUS

As mentioned before, the objective of the design of experimental set-up was to enable safe operation of a high pressure refrigerant with measurement accuracies at the level required for this study. The set-up consisted of two loops –the refrigerant loop and the coolant water loop, as shown in Figure 6.1. The parts of these loops are described in the following sections.

6.2.1 DESCRIPTION OF REFRIGERANT FLOW LOOP

The refrigerant loop consisted mainly of a tube evaporator or vapor generator, a condenser test section, a visualization section down stream of the condenser, a sub-cooler, a fluid reservoir/gas-liquid separator, a ceramic particulate filter and finally a micro-pump with a built-in flow measurement mechanism.

6.2.1.1 *Tube Evaporator*

The purpose of the evaporator located upstream to the condenser test section was to provide adequate heat input to the refrigerant flow with which to generate saturated and superheated vapor conditions at the entrance to the condenser test section.
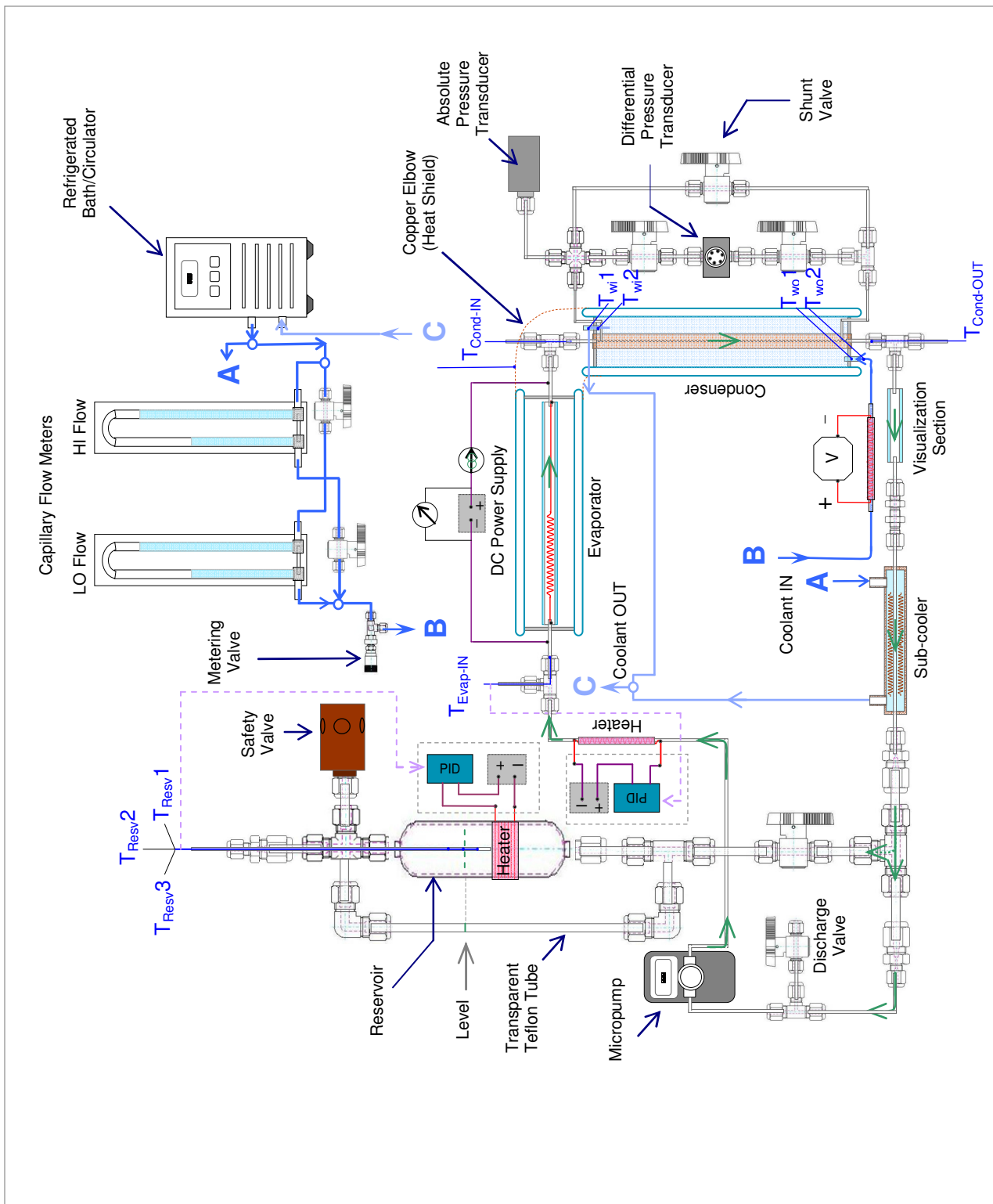
Figure 6.1: Schematic of the experimental setup

The evaporator consisted of a coil of heater wire housed in a 3/16 inch I.D. thick-walled Pyrex® glass tube (wall thickness 2.0 mm) and 80 mm length and fitted with thin-walled stainless steel inlet and outlet flow ports (wall thickness 0.1 mm thick). A transparent Pyrex tube was used as the housing for the heater element to enable visual observation of the flow at the exit of the evaporator. The thin-walled stainless steel tubing for the inlet and the outlet was used to minimize the axial conduction of heat along the port walls. The ports were connected to the Pyrex piece with high temperature epoxy resin with carbon fiber reinforcement to prevent cracking of the glass. A tightly wound coil of Nichrome wire (80% nickel, 20% chromium) that served as the electrical heating element was inserted into the Pyrex glass tube and the two ends of the heating element were brazed to the inlet and outlet ports, respectively. Thus the inlet and the outlet ports also acted as electrical leads. This helped to eliminate the need for a complicated fluid connector through which external power supply leads could get access to the heating element. This reduced complexity in plumbing which in turn reduces possibility of refrigerant leakage.

It was estimated that the maximum heat input requirement amongst different test conditions would be about 70 W. The net resistance of the heating element including the resistances at the braze contacts and the lead arrangement described previously was about 54 Ω. This value was decided upon *apriori* because the D.C. power supply acquired for heat input to the evaporator was equipped with an ammeter with having range of 0 - 1.2 A. The net resistance value exhibited a variation within 10% for different flow and heat input conditions. This was expected as the Nichrome wire resistivity varies as wire temperature varies. However, the heat input was calculated

based on input voltage and current measurements and hence heater resistance change did not influence the data.

The evaporator test section was pressure-tested in a separate loop consisting of a reciprocating oil pump and absolute pressure gage. The evaporator was subjected to an internal oil pressure of 400 psia sustained for a period of few hours while it was kept in an oven with an internal temperature of 70 C. It was concluded that the high temperature epoxy joint did not degrade at the elevated temperature and pressure and hence was acceptable for operation in the loop. Figure 6.2 shows the evaporator configuration described here.
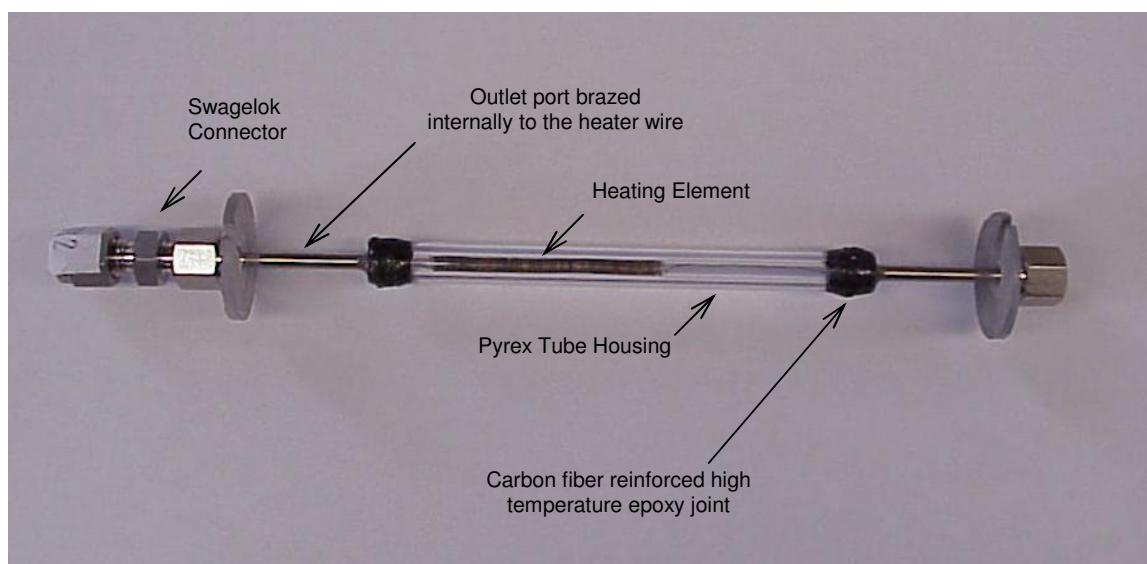
Figure 6.2: Tube evaporator with the labels indicating the various parts described in text.

Both the evaporator and the condenser test sections were placed in double-walled Pyrex Dewar cylinders as shown in Figure 6.3. The reason for using a Dewar was to minimized heat loss/gain to the system. A high vacuum (2 millibars) created between the Dewar walls eliminates the possibility of convective heat losses. Each Dewar shell was 50.8 mm O.D. and 25.4 mm I.D. As an additional measure of safety, the tube evaporator was placed inside a ½ inch I.D. transparent plexi-glass pipe of appropriate length before

the assembly was placed inside the eEvaporator Dewar shell. This was to prevent any damage to the Dewar cylinders in case the evaporator happened to shatter under high pressure.
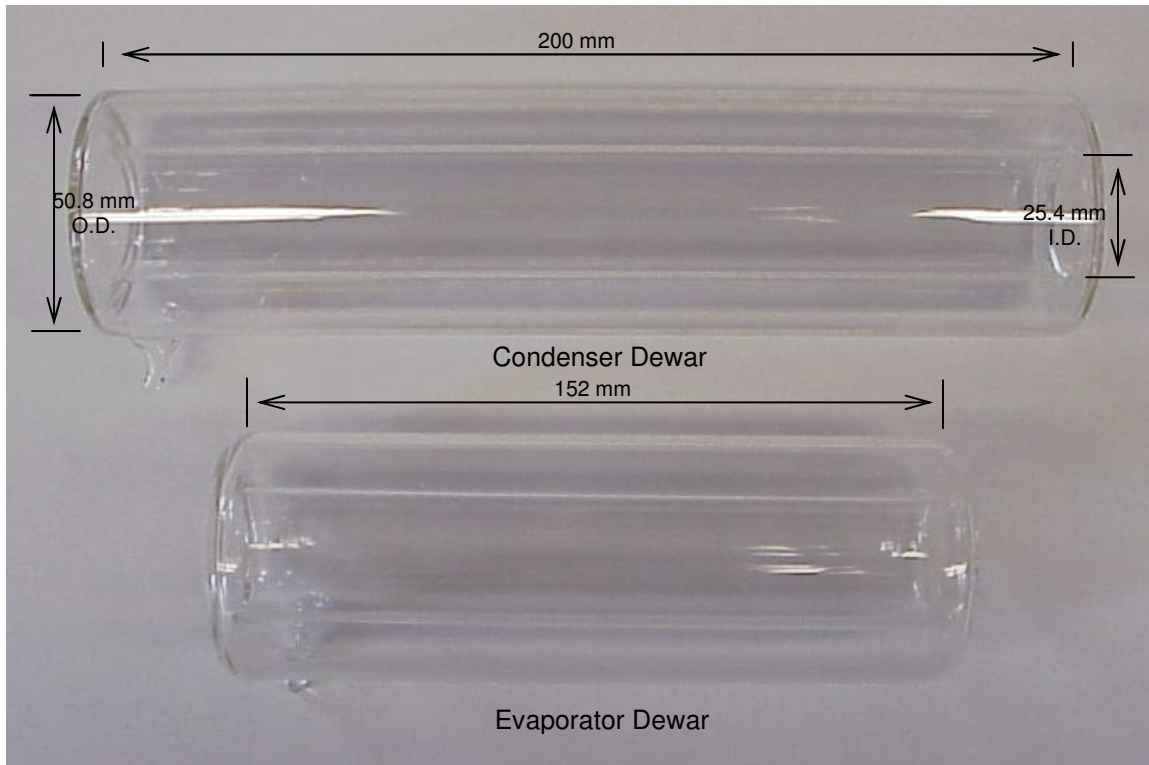
Figure 6.3: Photograph of the two heat-insulating double-walled Dewar cylinders used in the experimental apparatus.

6.2.1.2 *Micro-channel Condenser Test Section*

The design and fabrication of the micro-channel condenser test structure was described in details in chapter 5. This subsection elaborates on the integration and assembly of the test section structure with the refrigerant loop.

Five type-T thermocouples were embedded into the wall of the condenser test channel. The two halves of the type-T thermocouple are copper and constantan. Since 99.9% pure oxygen-free copper was used as the material for the micro-channel structure, it was appropriate to use the channel wall itself to represent one half of the type-T

thermocouple. Hence, five AWG 24 Teflon-sheath insulated constantan wires were soldered onto the channel wall at equi-spaced location. The diagram in Figure 6.4 indicates the electrical connections forming the five thermocouple junctions.

It was found necessary to use thicker gage constantan wires as thinner wires are more fragile and are often broken, thus resulting in disconnection. However, if for each thermocouple, a set of two wires were used, there would have been too many wires to be routed out of the Dewar cylinder and this might prevent the coolant to be uniformly distributed across the flow cross-section. Thus, using the material of the channel wall as "the second arm" of the thermocouples was helpful in reducing complexity.
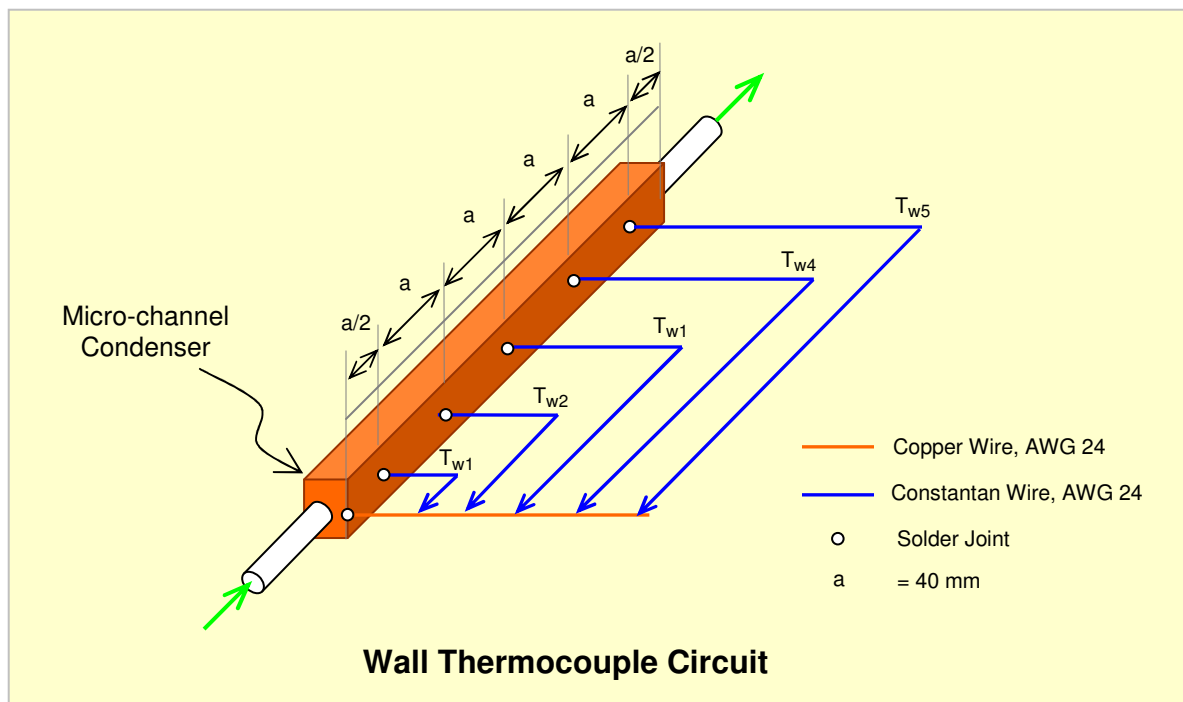
Figure 6.4: Diagram depicting the thermocouple junctions formed by Constantan soldered to the copper micro-channel structure.

As described in the above section, Dewar cylinders were used as heat-insulating casings for the evaporator and the condenser test section. In case of the condenser test

section, the Dewar cylinder additionally acted as a coolant water jacket as depicted in Figure 6.5.
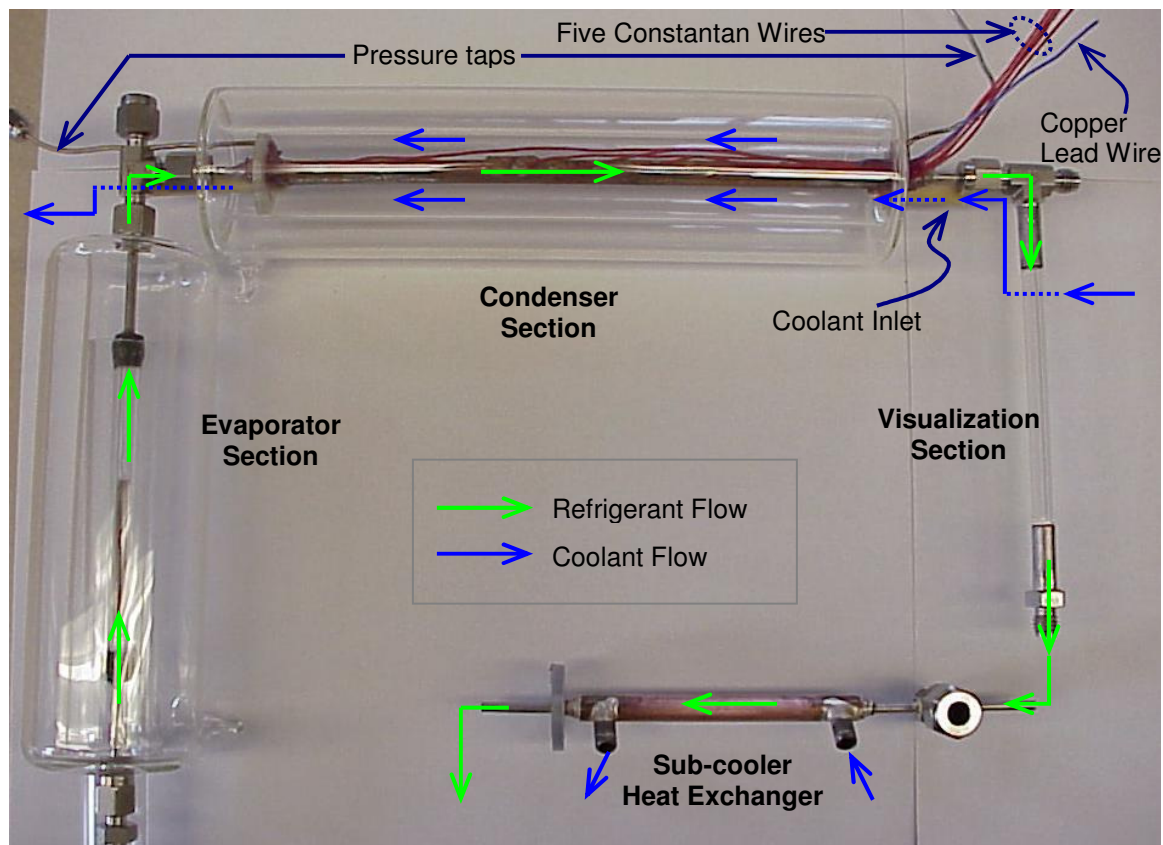
Figure 6.5: Part of the refrigerant loop indicating the evaporator and condenser test section encased in double-wall glass Dewar cylinders.

It was critical to contain the heat loss from the metal interconnect between the evaporator and the condenser section. Traditional heat insulations such as glass wool fillings and rubber foams were not appropriate, as this portion of the refrigerant flow path was somewhat complex and it was difficult to apply such insulations to this portion of the setup. First, this inter-connect provided an access to the thermocouple measuring temperature of the refrigerant at the inlet of the condenser. Second, this region also contained connections for coolant outlet and connection to the pressure port. Due to these connections, it was necessary to check for any refrigerant leakages by sniff tests which

would be difficult with traditional insulation. An alternative approach was therefore adopted. As shown in Figure 6.6, the two glass Dewar Cylinders were bridged by a 2 inch diameter copper elbow connected that was split in half.
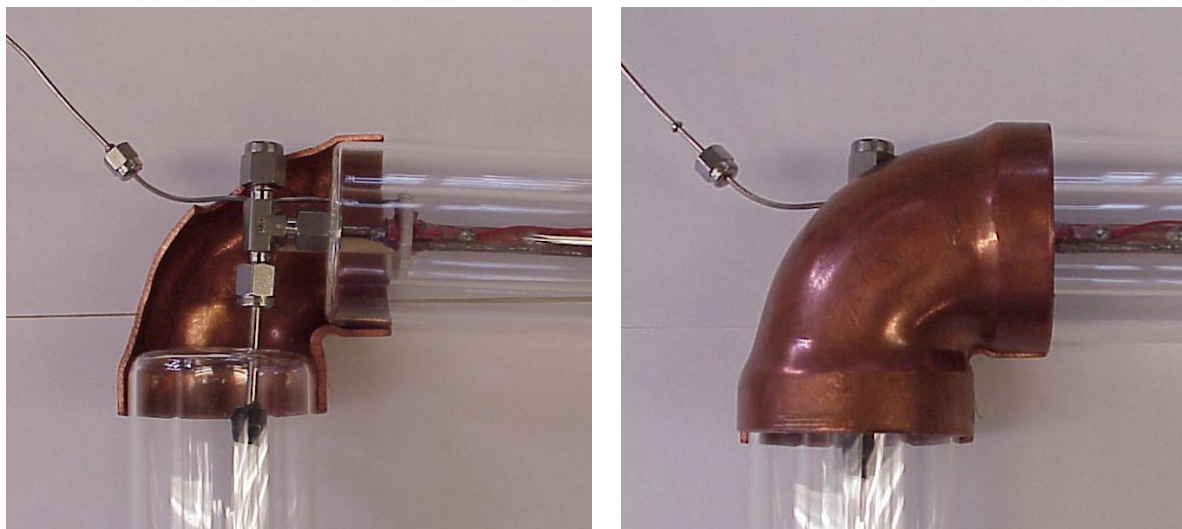
Figure 6.6: *Left* – The bottom half of the Copper elbow bridging the evaporator and condenser Dewar segments. *Right* – The top half of the elbow placed to complete the active heat shield.

On the outer surfaces of the two halves of the copper elbow, two Kapton® film heater patches were affixed and a thermocouple was soldered on to the surface of the elbow to monitor its temperature. Heat inputs to these two heater patches were controlled manually by a variac so that the reading of the above thermocouple was kept close to the temperature reading of the refrigerant inlet thermocouple. Thus the split copper acted as an active heat shield and eliminated formation of convection currents within its volume that would cause heat dissipation. Even then, some heat losses were expected due to conduction along the pressure port tube and the connection to the absolute pressure transducer. However, this arrangement provided the necessary flexibility of monitoring refrigerant leakages and also provided access to the inter-connect when needed.

6.2.1.3 *Visualization Section*

The visualization section downstream to the condenser allowed visual confirmation of the completion of the condensation process. Figure 6.5 includes an image of the visualization section and indicates its location within the refrigerant loop.

There is a difference between thermodynamically complete condensation and visually complete condensation, as described in the next chapter. In the former, the average enthalpy of the refrigerant at the outlet to the condenser is equal to the enthalpy of a saturated liquid. However, even at this condition, small vapor bubbles exist within a sub-cooled liquid. The condensation and elimination of all vapor bubbles require a certain period of time for heat dissipation. In order to completely suppress all vapor bubbles immediately at the exit of the condenser, sufficient sub-cooling was necessary. The amount of sub-cooling depended on the operating mass flux, and was found to have a range between 2 and 4 C. However, this sub-cooling effect was also dependant on the outlet geometry of the condenser and hence the sub-cooling levels necessary for the present test section and test conditions might not be replicated in another condenser with similar channel geometry. Also, the tests run at the two different outlet conditions – thermodynamically-complete and visually-complete – produced results for heat transfer coefficient that differed by up to 5%. Since the amount of sub-cooling necessary to reach the visually-complete state depended on test condition and outlet geometry and also because accurate control of sub-cooling temperature was found difficult, it was determined that the thermodynamically-complete state was a better target.

Therefore, the visualization test section served as a monitoring window to identify the above difference between two exit conditions. The fabrication and pressure testing of

this section was similar to that of the tube evaporator, which has been already been discussed.

6.2.1.4 *Sub-cooler Section*

The purpose of the sub-cooler section was to further extract heat from the refrigerant flow coming out of the condenser in order to suppress all remaining vapor bubbles. The necessity to suppress the bubbles was to ensure that only liquid refrigerant was passed into the micro-pump. Also, if sufficient sub-cooling was provided, the possibility of cavitation inside the micro-pump was eliminated.

The sub-cooler heat exchanger was a simple tube-in-tube heat exchanger in which coolant water flowed in the outer tube and refrigerant in the inner tube. To increase the heat transfer coefficient on the coolant side of the heat exchanger, copper wire mesh was inserted in the cavity between the inner and the outer tubes. The presence of the wire mesh enabled flow mixing. It should be noted that the sub-cooler was designed to take a heat load of no more that 10 W. Figure 6.5 indicates its location in the refrigerant loop.

6.2.1.5 *Fluid Reservoir and Vapor-Liquid Separator*

The fluid reservoir served several important functions in the refrigerant loop. First, as its name implies, it acted as a reservoir for holding excess liquid refrigerant in the loop. In any refrigeration system, the refrigerant loop cannot be allowed to be filled with liquid only since the loop pressure would experience large differences due to the variation in operating temperature. Hence, the reservoir was meant to provide a "cushion volume" for extra refrigerant to flow into it, if the pressure level in the loop increased.

Second, the reservoir also acted as a separator of any non-condensable (or condensable) gas/vapor bubble that emerged from the sub-cooler heat exchanger before the flow entered into the micro-pump. Although great precautions were taken to secure the refrigerant loop against any possible air leaks during charging and operation of the system, it was possible that a miniscule amount of non-condensable gas might have existed inside the refrigerant loop. The reservoir provided an opportunity for any trace non-condensable gas to be segregated from the flow after a few trial test runs. For this function, it was necessary that the reservoir was to be kept as a higher elevation than the rest of the loop.

Third, the reservoir also acted as an essential component in the feed-back loop for control of absolute pressure in the system. In order to measure the saturation temperature of the refrigerant at the inlet to the condenser, an absolute pressure transducer was connected to the 4-way interconnect which also accepted the connection to the pressure port as shown in schematic in Figure 6.1.

The reservoir cylinder, as shown in the photograph in Figure 6.7, was a Swagelok® double-ended 316 stainless steel sample cylinder with an internal volume of 300 cc. The top end of the reservoir cylinder was fitted to a 4-way connector. A 350 psia spring-loaded safety valve was fitted to this connector. A thin-walled 1/8-inch stainless steel tube, which was blinded at one end, was inserted into the reservoir in such a way that the blinded end of the tubing reached the mid-section of the reservoir cylinder. Three calibrated thermocouples were inserted into the tubing so that their tips were successively placed 1 inch apart as shown in the schematic. Due to varying levels at of the refrigerant at different operating points, it was best not to locate the tips of the three thermocouples

at one place only. The average readings of the three thermocouples would be a better estimate of the saturation temperature of the mixture.

A 3/8-inch Teflon tube was connected in parallel to the reservoir; its function was to enable monitoring the fluid level inside the reservoir during the refrigerant charging process. It was desired that of the three thermocouples, the middle thermocouple was to be kept approximately close to the vapor liquid interface inside the reservoir for typical operating conditions, and the level monitoring tube served as a visual tool to ensure that. During the heat transfer experimentation, the liquid level inside the reservoir typically shifted by about 2 to 3 mm due to presence of vapor in the evaporator and condenser sections.

The reservoir was provided with a heater element wrapped around it at about the location of the liquid level. Power input to this heater was supplied by a DC power supply. In order to control the operating absolute pressure at the entrance to the condenser, the voltage signal from the absolute pressure transducer was fed to a PID controller which controlled the heat input to the reservoir heater. At a steady state operation of the system, the PID controller altered between a "switched on" and "switched off" states; the duration of the stay at each state was affected, primarily, by the ambient conditions.

However, during the actual operation of the experimental apparatus, it was found that the controller was ineffective in dampening the fluctuation of pressure in the system. This was possible for two reasons. Firstly, there was a response delay between the instant the reservoir heater was "switched on" and instant when pressure increase was noted by the absolute pressure transducer. This was because there were several steps in this control

operation: the increase in the surface temperature of the reservoir translated to increase in the saturation pressure of the two-phase mixture contained in the reservoir. This pressure increase altered the effective average pressure inside the condenser which needed some time to stabilize. Once stabilization was reached, the corresponding pressure signal directed the PID controller to switch off and the surface temperature of the reservoir gradually reduced, thus completing the feed-back loop. These several steps contributed to the response delay. Secondly, due to the boiling process inside the tube evaporator, the absolute pressure transducer experienced certain low amplitude fluctuation which perhaps caused a certain amount of difficulty/delay for the controller in its switching decision and may have resulted in pressure "swings" about the control point.

In order to minimize the response delay and to measure the system's operating pressure with greater accuracy, the signal from one of three thermocouples (in the tube that was inserted into the reservoir) to measure the saturation pressure was used as the control signal for the PID controller. It was observed that this significantly improved the response delay and the overall stability of the system.
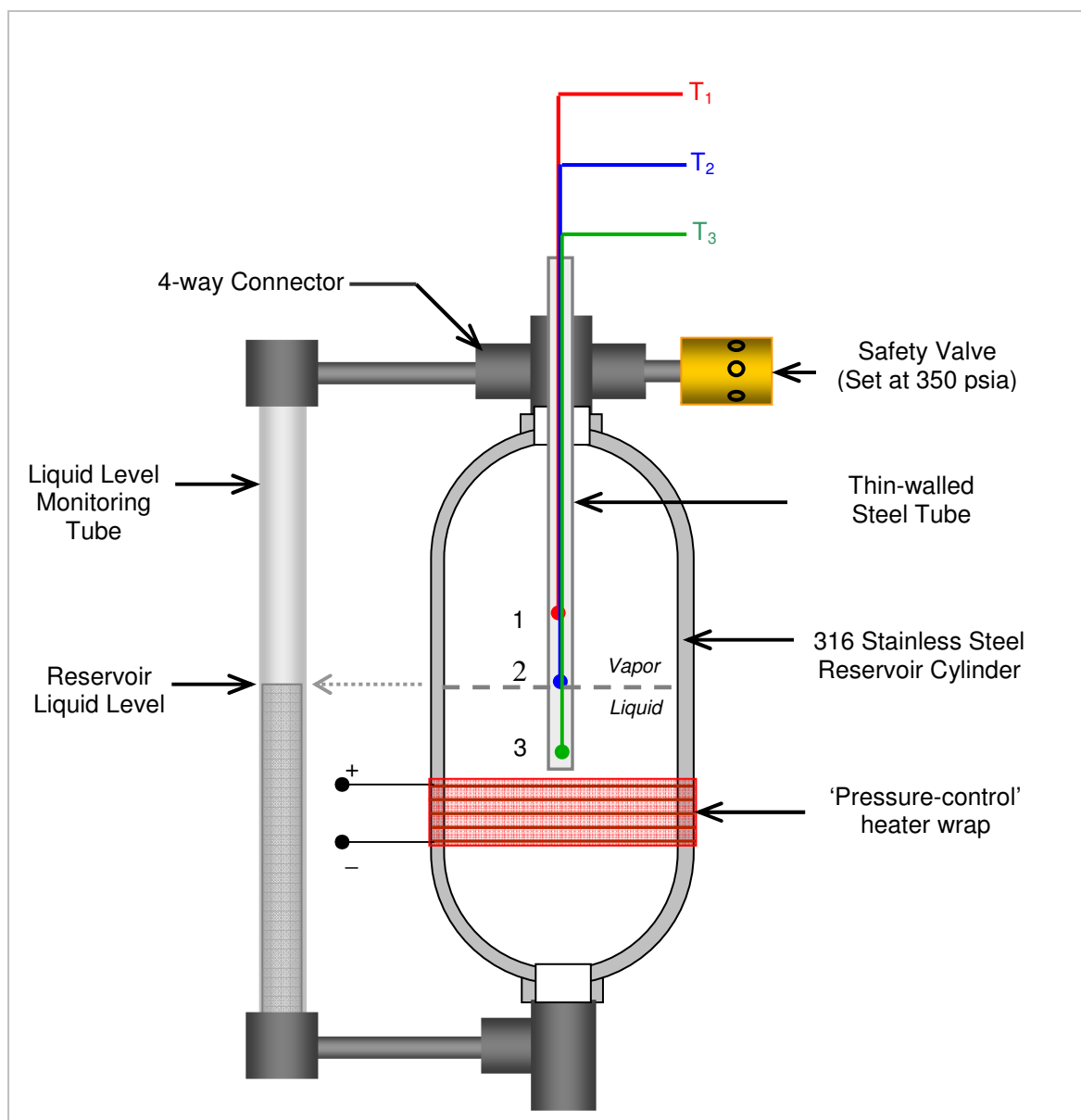
Figure 6.7: Schematic illustrating the various parts of the Reservoir System

6.2.1.6 *Micro-pump*

An ISMATEC® MCP-Z Standard gear-based micro-pump was selected as the prime-mover for the working fluid. The pump was equipped with control electronics which monitored, under different menu-based choices, the rotational speed, dispensed volume or the number of rotations. The flow range of the pump was 0 to 180 ml/min and it could be calibrated. The pump gear head was reported by the manufacturer to consist of

accurately machined parts and the product of swept volume per rotation to the rotational speed of the gear head constituted the flow rate delivered by the pump. Due to a unique "suction shoe" arrangement in the gear-head, the flow was unidirectional and the flow rate was independent of the temperature and pressure drop across the pump for the operating range. Also, the flow was observed to be nearly pulse-free.

The micro-pump flow rate was calibrated using distilled water at room temperature. A fixed number of rotations were allowed and then the weight of the dispensed water was measured to generate a flow calibration curve. The calibration factor, thus generated, was incorporated in the control memory of the pump so that the digital readout reflected the calibrated flow rate.

Since the micro-pump was sensitive to any particulate in the flow, as a precaution, a 2 μm porous ceramic filter was inserted in the refrigerant loop upstream to the micro-pump.

6.2.1.7 *Refrigerant Loop Controls and Measurements*

The purpose of this section is to list the various measurements that were made at different locations of the refrigerant loop. Also, various control loops were created to maintain constancy of pressure or temperature and these will be discussed in the present subsection as well.

Several thermocouple-based temperature measurements were made at different locations in the refrigerant loop. Primarily Omega® type-T AWG32 thermocouples with Teflon wire insulations were used. The copper and constantan wires of each thermocouple were butt-joined by a spark discharge and melting process which

consistently created small ball shapes. Also, unlike solder joints, this process of creation of the thermocouple junction did not introduce a foreign metal into the joint. Therefore it was expected that the thermocouple junctions would exhibit temperature responses close to each other.

Temperature measurements were made at the inlets to the evaporator and to the condenser and at the exit of the condenser. In each case, the thermocouple tips were inserted into the tubing up to the entrance or exit location. Temperature measurements were also made by the five thermocouple junctions that were created on the wall of the micro-channel as described in Section 6.2.1.2. However, these thermocouples, unlike the other thermocouples in the system were AWG24 gage. Three thermocouples that measured the liquid-vapor interface temperature (or the saturation temperature) inside the reservoir cylinder as described in Section 6.2.1.4. A thermocouple was implanted on the wall of the copper elbow bridging the two Dewar cylinders to measure the surface temperature of the elbow. Split-wire thermocouples that were inserted into the refrigerant flow path to measure the flow directly were encased in small pieces of 1/8 inch stainless steel tubing filled with epoxy. The epoxy was necessary to create a leak-free connection. The piece of tubing was then inserted into the flow path by typical Swagelok® connectors.

There were two pressure measurements in the refrigerant loop. A Setra® absolute pressure transducer was used to measure the condenser inlet pressure. It was discussed in Section 6.2.1.4 that a better way of measuring this pressure was to determine the saturation temperature inside the reservoir and convert it into saturation pressure. Still the absolute pressure transducer served as a corroborating value. The other pressure

measurement was the measurement of the differential pressure by means of diaphragm-type differential pressure transducer from Validyne Corp. The differential pressure transducer was connected to the micro-channel pressure ports by 1/16 inch stainless steel tubing. The use of a tube with such small cross-section helped dampen the rapid fluctuations in the pressure signal experienced due to active boiling process. The differential pressure transducer was protected from sudden pressure surges, possible during the charging process, by two quarter-turn plug shut-off valves at its either port and was shunted by another such valve, as shown in Figure 6.1.

There were three instrumented control loops in the refrigerant system, of which two were mentioned before. The first one was the control of the copper elbow heat shield temperature which was maintained close to the temperature at the inlet to the condenser. It was observed that a small input power to the patch heaters was sufficient for a stable control of this temperature and hence this input was manually adjusted from time-to-time making a PID controller unnecessary. The second control loop was the control of the saturation temperature inside the reservoir. As mentioned before, a Watlow® microelectronic PID controller was used for this purpose. A third active feed-back control loop was created to control the temperature of the sub-cooled liquid refrigerant at the inlet to the tube evaporator. It was observed that as ambient temperature or air draft across varied, this temperature exhibited a drift. Since the evaporator heat input was calculated based on this inlet temperature, it was necessary to stabilize it at a value above the ambient range. For that end, a small heater wire element was wound on the stainless steel tube and connected to a DC power supply; the heater power was governed by a second PID controller which received the evaporator inlet temperature as its input signal.

This completes the description of the various components of the refrigerant loop. A photograph of the loop is shown in Figure 6.8. In this image, the condenser section and the reservoir are shown with insulation covering.
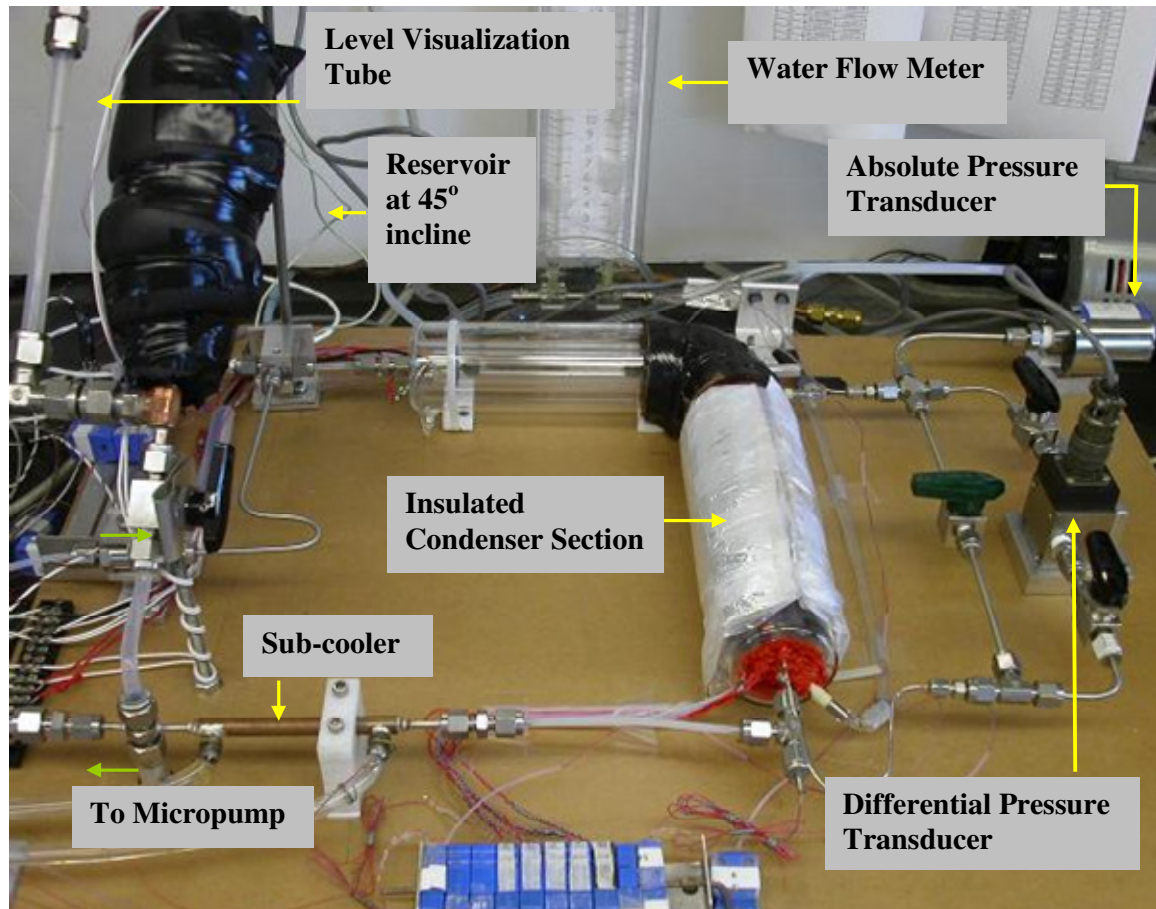
Figure 6.8: Photograph of the refrigerant loop assembly

6.2.2   DESCRIPTION OF COOLANT (WATER) FLOW LOOP

The coolant water flow loop consists of a refrigerated bath circulator, coolant flow measurement and metering system and temperature-control heater.

6.2.2.1 *Refrigerated Bath Circulator*

The 300 W NESLAB refrigerated bath/circulator was selected to maintain a coolant water flow at a desired temperature in the coolant loop. It consisted of an internal refrigeration system and a water circulating centrifugal pump. The temperature control system consisted of a micro-electronic circuit and a digital read-out. The bath/circulator was capable of controlling water temperature in the range of 5-95 C at an accuracy of ±0.03 C. To prevent fouling in the coolant loop and also inside the bath/circulator, distilled water was used as the working coolant.

6.2.2.2 *Coolant Flow Measurement and Metering System*

. The coolant flow from the refrigerated bath/circulator was split into two streams – one flowing through the condenser section (named B in schematic in Figure 5.1) and the other flowing through the sub-cooler heat exchanger (named A). The flow measurement and metering system for the coolant stream through the condenser section consisted of two capillary flow meters connected in parallel and a metering valve down-stream of the flow meters. This metering valve, together with a control heater, was used to vary the coolant flow rate through the condenser and its temperature difference across the condenser.

To decrease the variation in the wall temperature of the condenser, as will be further described in the next chapter, it was desired to keep the temperature difference between the coolant inlet and coolant outlet of the condenser at 2 to 2.5C. It was also observed during the analysis of errors in the system that the uncertainty in heat transfer coefficient decreased with the increase in the above difference of coolant inlet and outlet

temperatures. A value less than 2 C, if chosen, would significantly increase the uncertainty. For each test condition at the inlet to the condenser, a value of the flow rate of coolant was arrived at by calculation. This value was set by the flow measurement system described above. After the required flow was thus set, the heat input to the control heater was varied gently using a variac until the desired steady state coolant temperature difference was achieved.

There was no measurement system provided for the other coolant stream A that was flowing through the sub-cooler. This led to a situation in which the outlet temperature of the sub-cooled refrigerant varied. However, as described in Section 6.2.1.6, the refrigerant temperature was stabilized using a feedback controlled heating section upstream to the evaporator. Hence the lack of instrumentation and control on the sub-cooler did not cause a difficulty. This concludes the description of the coolant loop.

6.3 INSTRUMENTATION AND MEASUREMENT SYSTEM

In this section a summary of the various instruments and measurement devices, belonging to the three categories of measurements and/or controls in the refrigerant and coolant loops – temperature, pressure and flow – will be provided. It should be noted here that all thermocouple and pressure data were recorded using an Inlet Pentium® computer and Agilent® Data Acquisitions System (DAS) containing two 20-channel multiplexer data cards that were vendor-calibrated. Data for the flow measurements were monitored during an experimental run and were manually recorded.

6.3.1 MEASUREMENTS OF TEMPERATURE

As referenced in the earlier sections and also indicated in the Figure 5(i), there were several locations in the two flow loops where accurate temperature measurements were necessary. AWG32 type-T thermocouples that were calibrated in the refrigerated bath/circulator using an accurate RTD reference device were used in the refrigerant loop. The measurements were made at the evaporator inlet ($T_{Evap-IN}$), condenser inlet ($T_{Cond-IN}$) and condenser outlet ($T_{Cond-OUT}$). The system pressure was calculated based on the three thermocouples suspended inside the reservoir (T_{Resv} $i,$ $i = 1, 2, 3$). The reservoir heater was controlled using a self-tuned Watlow PID controller. The heater upstream to the evaporator was similarly controlled using another PID controller.

Each of the coolant temperatures at the inlet and outlet of the condenser was measured using two AWG32 calibrated thermocouples (T_{wi1} and T_{wi2}). It was observed that the energy balance and estimated average heat transfer coefficients, as discussed in Chapter 7, were heavily dependant on these measurements, and hence two thermocouples were used at each location. In order to improve the accuracy, the thermocouples were later replaced with four Thin-film platinum resistance temperature detectors (RTDs). Further a Y-junction arrangement, as shown in Figure 6.9, allowed proper positioning of the RTD sensors and a wire mesh placed in the flow before it reached the RTDs was also helpful in mixing the flow, so that the temperatures measured corresponded to the coolant bulk temperature.
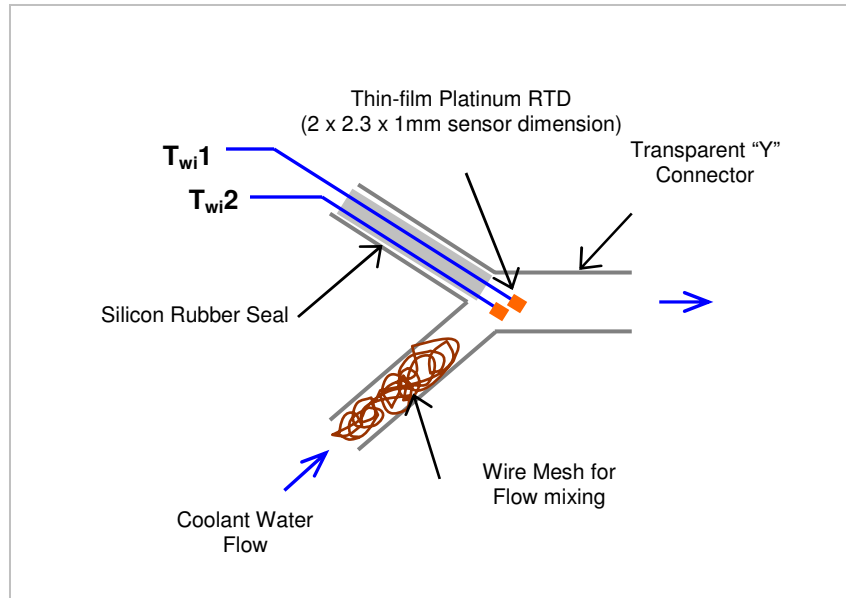
Figure 6.9: Y-connection indicating the location of RTDs for accurate coolant temperature measurement at the inlet to the condenser. A similar arrangement was provided at the coolant outlet.

6.3.2   MEASUREMENTS OF PRESSURE

The two pressure measurement devices were the Setra® absolute pressure transducer with a range of 0-500 psi, and a Validyne DP-15 differential pressure transducer with a differential pressure rang of 0-14 kPa. As mentioned earlier, the system pressure was derived using the measurement of the saturation pressure inside the reservoir. The absolute pressure signal was used to corroborate this value.

6.3.3   MEASUREMENTS OF FLOWS

As mentioned earlier, the refrigerant flow was measured by the calibrated micro-pump which was provided with micro-electronic control and digital readout.

The flow measurement for the coolant stream B (ref. to Figure 6.1) was measured using two capillary flow meters placed in a parallel configuration in such a way that flow was directed through one of the meters for a given test condition using the shut-off valves,

shown in Figure 6.1. It was found after a survey of commercially available and affordable rotameters that the expected accuracies of such meters were within ± 2 to 4% of full-scale. It was decided that it would be better to create two customized capillary-pressure-drop-based flow meters for two flow ranges necessary. In these flow meters, the flow was measured by the pressure drop across the capillaries, of a selected lengths and internal diameters, measured by the heights of water in the two columns located at the upstream and down stream of the capillary. The difference in heights (Δh) of the water levels in these two columns indicated the difference in static pressure ($\Delta p = \rho_w g \Delta h$) across the capillary. The correspondence between the static pressure difference, Δp and the flow rate passing through the capillary was found by calibration. The height difference was measured by a millimeter scale with a least count of 0.5 mm. Therefore, the accuracy of this measurement was 1.0 mm. An appropriate choice of capillary was made so that the measurement accuracy was kept at or below ±2% of reading. As mentioned earlier, two different flow meters were fabricated and calibrated to serve the different flow ranges (20 to 130 ml/min and 140-550 ml/min) necessary for different refrigerant test conditions.

6.4 INSTRUMENT CALIBRATION

In this section, the procedure to calibrate various instruments will be discussed, including calibration of thermocouples and RTDs, pressure transducers, and flow meters.

6.4.1 CALIBRATION OF THERMOCOUPLES

For the purpose of calibration, all thermocouple and RTDs wires were put in a bunch in such a way that the sensor tips of the RTDs and the thermocouple junctions were closely located. The calibration was performed between the ranges of 10 to 90 C in steps of 10 C in a water bath inside the refrigerated bath/circulator which maintained a set point water temperature within ± 0.03 C stability. An RTD probe with accuracy of ± 0.003 C was inserted into the water bath with its tip in close proximity to those of the thermocouples and RTDs. Temperatures were observed by a DAS software, and upon reaching stability for a continuous period of 5 minutes the data were recorded at each calibration point. It was found that the RTD's as well as the thermocouples exhibited linearity with a correlation coefficient greater than 0.9999. For the sake of brevity, only the calibration chart for the RTDs is shown in Figure 6.10.

The five thermocouple junctions that were created on the wall of the micro-channel structure were calibrated *in situ*. After calibration of all other instruments and sensors and their assembly in the experimental apparatus, these five thermocouples junctions were calibrated. Coolant water was circulated in the coolant jacket while refrigerant was circulated inside the micro-channel. Refrigerant was prevented from boiling inside the micro-channel by increasing the system pressure sufficiently. The refrigerant temperature was controlled by power input to the heater upstream of the
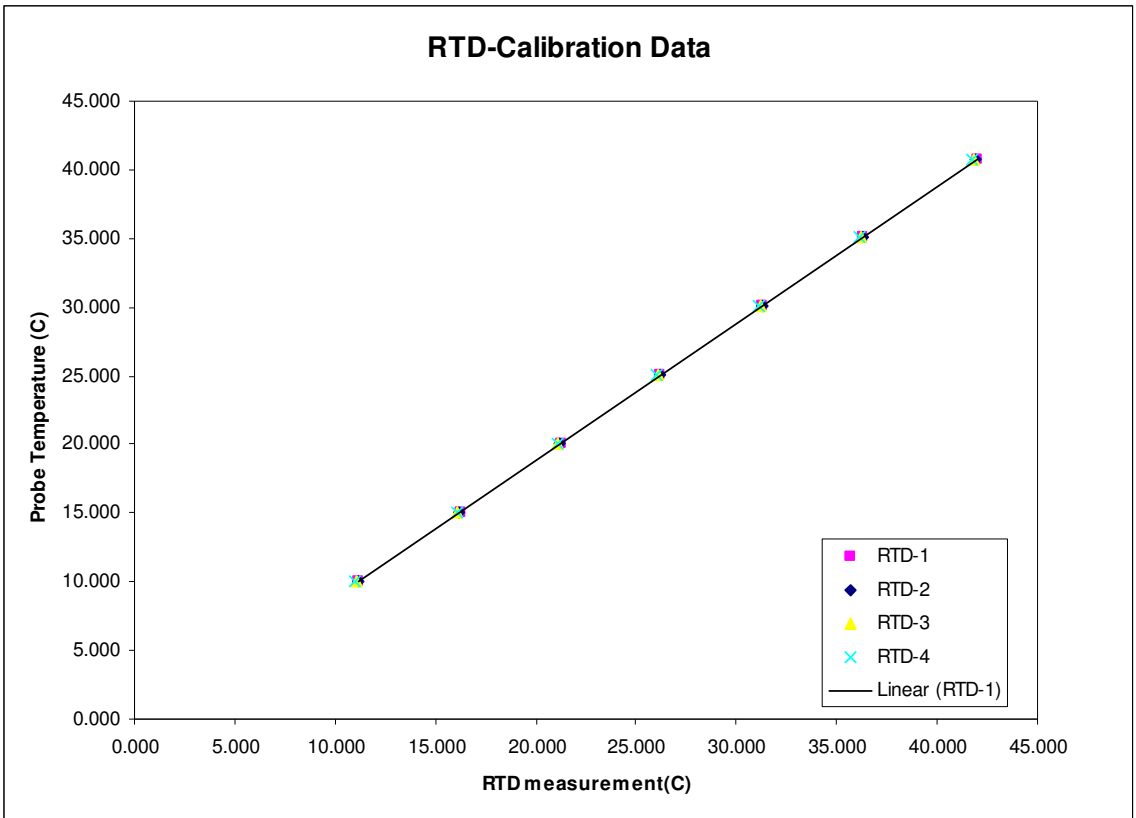
Figure 6.10: Calibration chart for the Thin-film Platinum RTDs that measured the coolant inlet and outlet temperatures.

evaporator. The inlet and outlet temperatures of the refrigerant and the coolant water for the condenser test section were kept equal and observations were made to detect any possible temperature drift over a sufficient period of time. When assured of stability, temperatures were recorded and translated into the calibration chart shown in Figure 6.11.

**Calibration of Micro-channel
Wall Thermocouple Junctions**

Tw 1: y = 1.031x - 0.9806
         R^2 = 0.9999

Tw 2: y = 1.021x - 0.7872
         R^2 = 1

Tw 3: = 1.0106x - 0.4742
         R^2 = 1

Tw 4: y = 1.0112x - 0.5082
         R^2 = 1

Tw 5: = 1.0151x - 0.6435
         R^2 = 1

Average Water Temperature

Wall Thermocouple Temperature (C)

Tw1
Tw2
Tw3
Tw4
Tw5
Linear (Tw1)
Linear (Tw2)
Linear (Tw5)
Linear (Tw4)
Linear (Tw3)
Linear (Tw3)
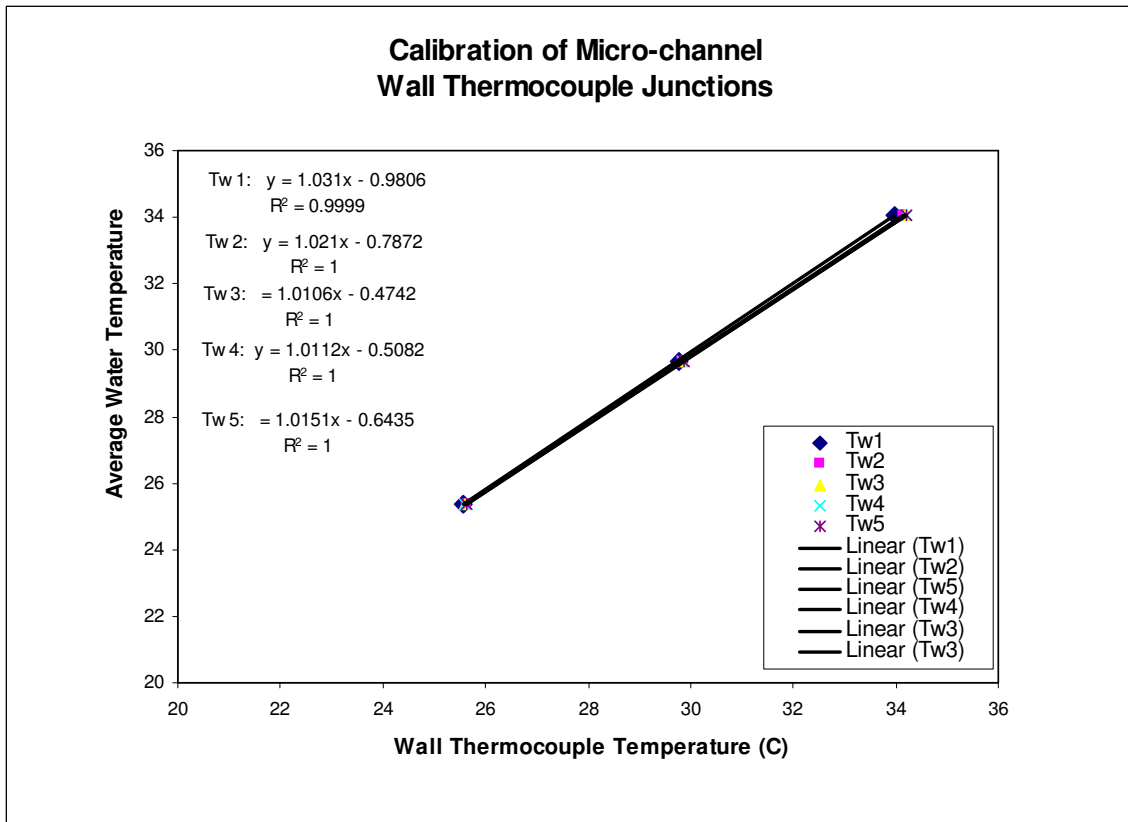
Figure 6.11: Calibration chart for condenser wall thermocouples.

6.4.2   CALIBRATION OF DIFFERENTIAL PRESSURE TRANSDUCER

The Validyne® DP-15 bidirectional differential pressure transducer is a diaphragm-type transducer with a diaphragm having a range of 14 kPa. It was calibrated using a vertical graduated U-tube manometer-like setup. The U-tube manometer was created with ¼" Tygon® tubing, with one arm of the U-tube connected to one of the ports of the differential pressure transducer. The other arm of the U-tube and the remaining port of the transducer were both kept open to atmosphere. Water was poured into the free arm of U-tube using a squeeze bottle. Care was taken so that the water column in either arm of the U-tube was devoid of bubbles or air locks which might alter the calibration results. The pressure differences, estimated from the difference in the heights of the water

columns in the two arms of the U-tube, were thus exerted on one port of the differential pressure transducer and its voltage outputs were recorded. The transducer connection was reversed and the procedure was repeated. Figure 6.12 shows the calibration results from the above procedure.

Calibration of DP Transducer: Validyne DP-15-32 (0 - 14 kPa)

$y = 1.3959x$
$R^2 = 0.9999$

Experimental Data

Linear (Experimental Data)
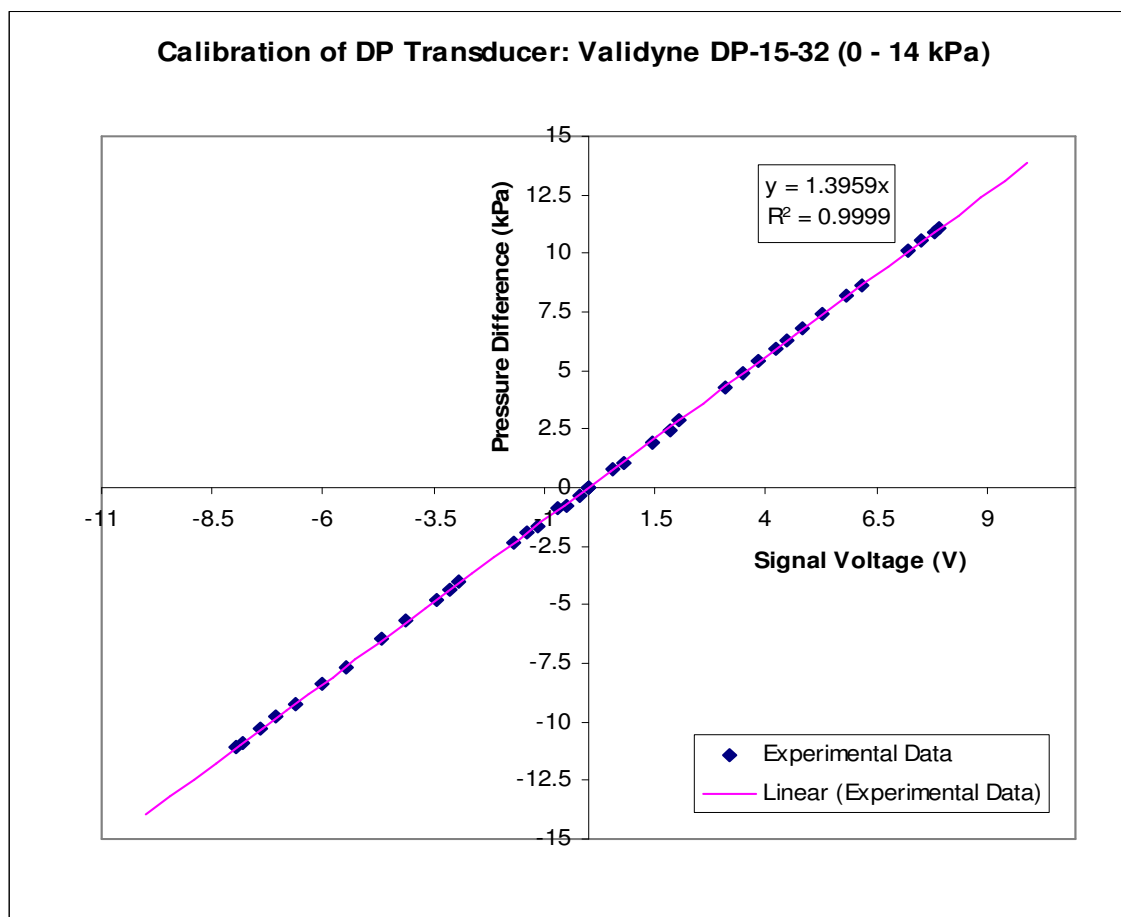
Figure 6.12: Calibration results for Validyne® differential pressure transducer using U-tube manometer.

6.4.3   CALIBRATION OF THE ABSOLUTE PRESSURE TRANSDUCER

The Setra® absolute pressure transducer with a range of $0 - 550$ psia was purchased with a factory calibration of $\pm 0.11\%$ full scale accuracy. The transducer was measured against another accurate reference pressure transducer (pre-calibrated by dead weight method) by pressurizing both transducers, kept in parallel configuration, using

compressed air. The pressure transducer was calibrated in the operating pressure range of 0 – 300 psia. The results of the two calibration runs, as shown in Figure 6.13, were deemed repeatable, linear and acceptable within the factory accuracy.

Calibration of Setra 0 - 550 psia Absolute Pressure Transducer
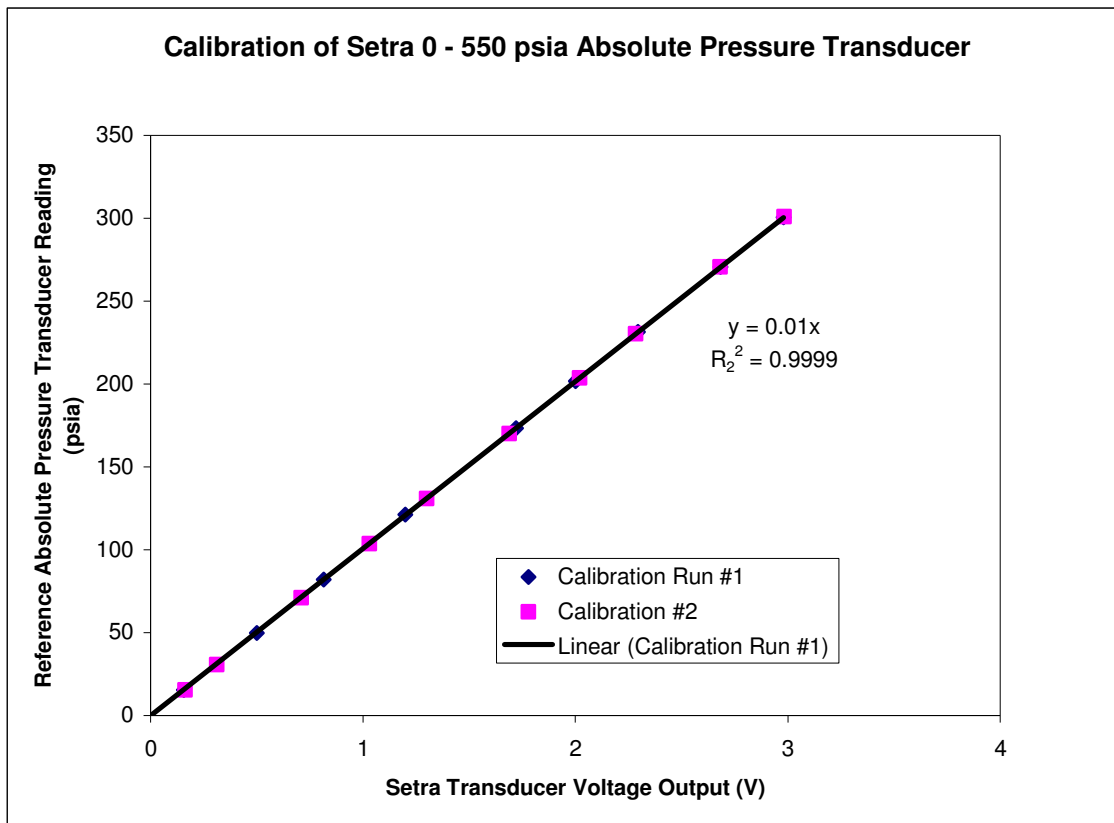
Figure 6.13: Results for the corroboration of the linearity and accuracy of factory calibrated Setra®
absolute pressure transducer.

6.4.4   CALIBRATION OF FLOW METERS

The low-flow and high-flow coolant water flow meters were calibrated by measuring the water flow rate passing through their capillary passages and recording the difference in the heights of the water column in each arm of the flow meter. Figures 6.14 and 6.15 indicate the calibration charts for the capillary flow meters. The calibration

process was repeated a few times and the graphs indicate the cumulative calibration data used to derive the calibration correlation.
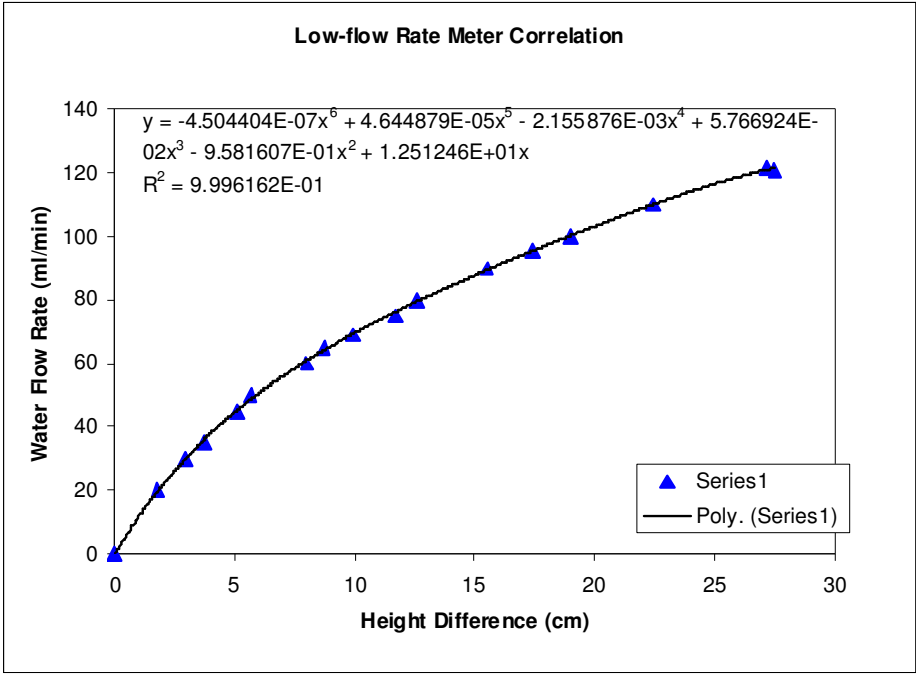
Figure 6.14: Low flow water flow meter calibration chart
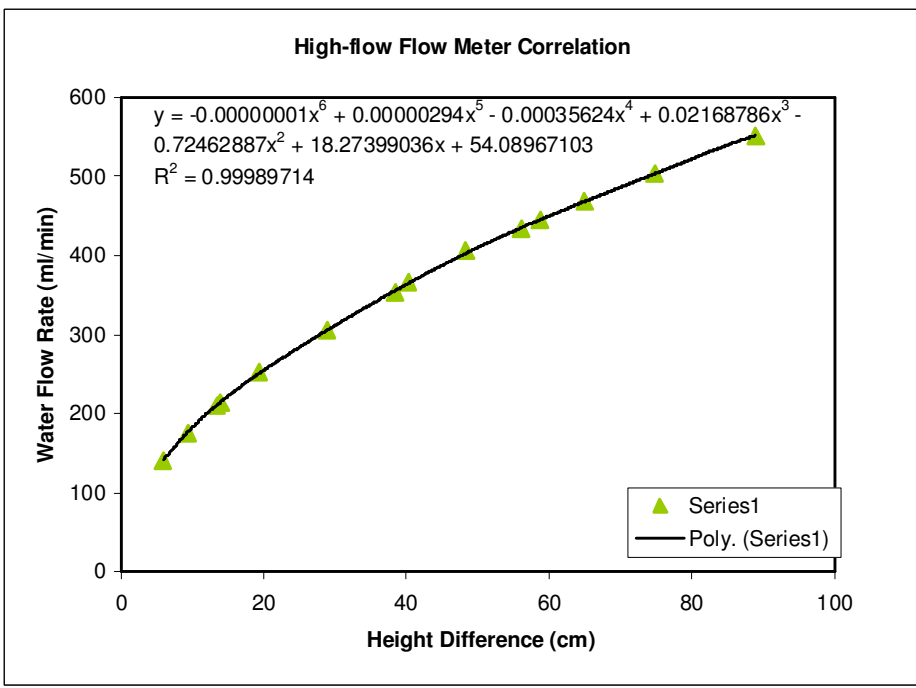
Figure 6.15: High flow water flow meter calibration chart

6.4.5   CALIBRATION OF MICRO-PUMP FLOW METER

The Ismatec ® micropump internal flow measurement system was calibrated by timed dispensation of water flowing through the pump at different monitor readings. Figure 6.16 indicates the linear response of the flow meter.
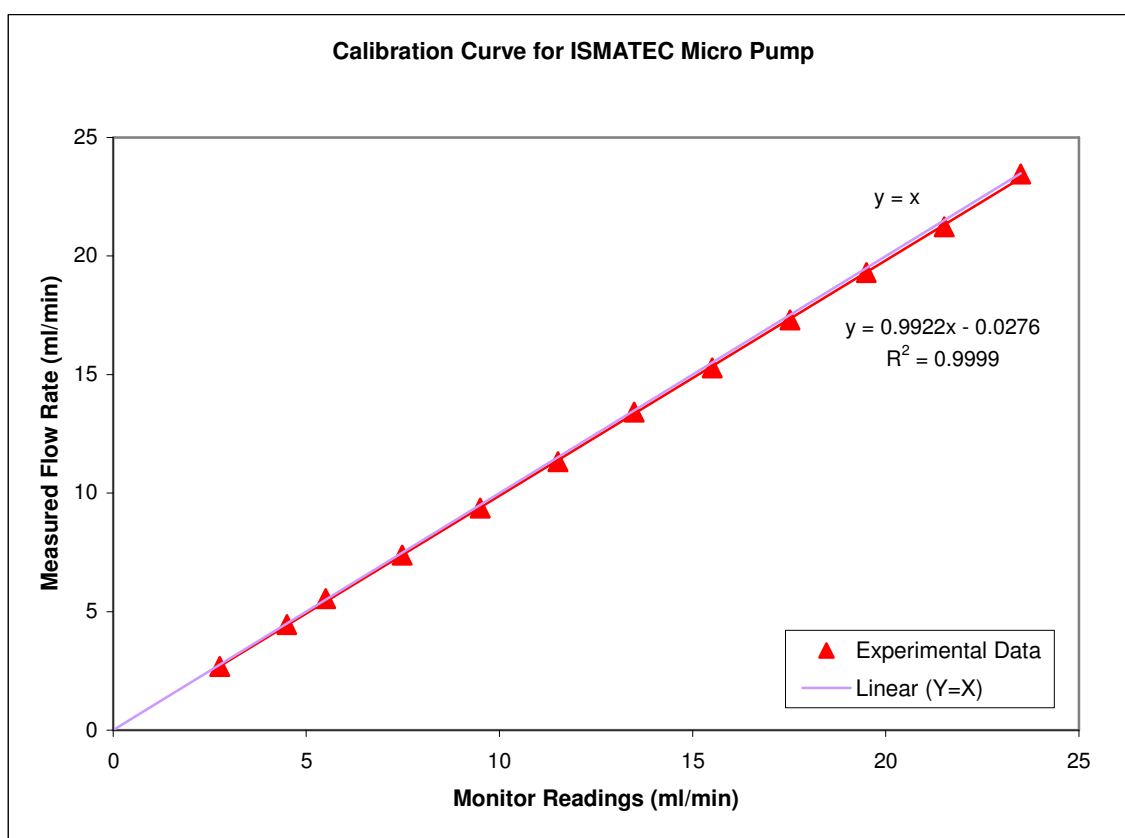
Figure 6.16: Flow response versus monitor readings of the Ismatec micropump internal flow meter.

6.4.6   TUNING OF PID CONTROLLERS

A PID (Partial-Integral-Derivative) controller is a feedback mechanism which attempts to correct the error between the measured process variable and the desired set-point by measuring the error value and outputting a corrective signal to remedy that error. The PID control algorithm involves three separate parameters – the proportional parameter determines the reaction to the most current error, the Integral parameters

determines the reaction based on the sum of the recent errors, and finally the derivative parameter determines the reaction to the rate at which the error value is shifting. The weighted sum of these values is used to control the process via a control element, which in the present cases were heaters operated at a constant DC voltage. The PID controllers have a primitive option of acting as a control switch (heater circuit simply turned 'ON'/ 'OFF' depending on the sign of error). The success of such a control strategy depends largely on the proportion of the corrective action to that of the measured fluctuations and also on the delay in reaction. However the utility of the PID controllers stems from its micro-electronic logic circuit with auto-tuning features. Although on certain occasions, manual tuning of the PID parameters was found convenient, in most cases the auto-tuning feature was used to set the most optimum parameters. Figure 6.17 indicates the difference between the control effects from manual adjustments and auto-tuning of the reservoir PID controller on the system pressure. To enable visibility on one graph, different desired set-points (16 and 25 psi) were chosen for the two cases.
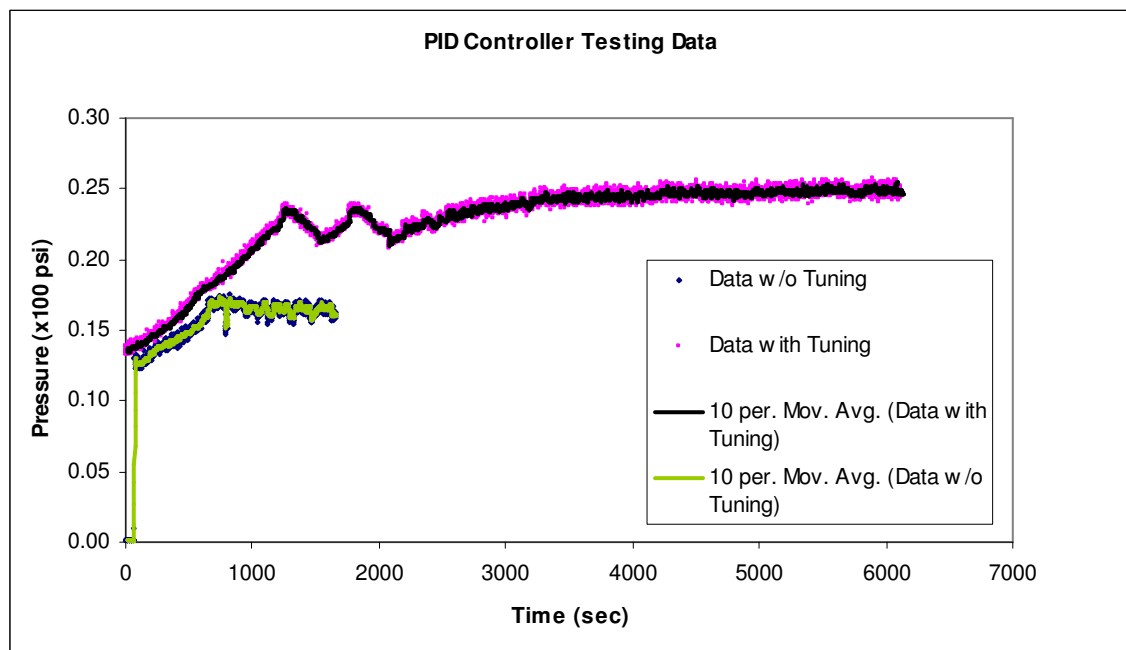
Figure 6.17: Effects of different control options on the absolute pressure of the system.

6.4.7 SUMMARY OF CALIBRATION RESULTS

Sufficient care was adopted in the calibration of various instruments and meters present in the system. The calibration runs were repeated several times in order to verify the stability of the calibration process and the repeatability of the results. Final sets of calibration data were used in generating correlations that were presented in this chapter. Table 6.1 below indicates a summary of various instruments, their operating ranges and other specifications and error limits obtained from their calibration results.

Table 6.1: Summary of Measurement and Control System for Experimental Apparatus

Measurement /Operation	Operating Range	Instrument	Accuracy
Refrigerant Flow Rate	0.06 – 0.6 gm/s	ISMATEC® Micro-pump Flow Meter	±1% of rate
Water Flow Measurement	0 – 550 ml/min	Calibrated Capillary Flow Meter	< ±1% of FS
Absolute Pressure Transducer	40 – 320 psi	Setra 205 Transducer	±0.11% of FS (FS: 0 – 500 psi)
Differential Pressure Transducer	0 – 14 kPa (0 – 2 psi)	Validyne DP15-32 Differential Pressure Transducer	±0.25% FS
Temperature Measurement	0 – 100 C	AWG 24 & 32 T-type Thermocouples and Platinum RTDs	±0.1 C & ±0.08 C
Pressure Stabilization	0 – 5 V input	Watlow® Series SD PID Controller	±0.1% of Span
Cooling for Refrigerant loop	0 – 300 W	Neslab Bath/Circulator	Stability: ±0.03 C

6.5 SELECTION OF WORKING FLUIDS

Refrigerant R134a was selected as the first of the two working fluids for the present study. R134a is a high pressure refrigerant commonly used in the refrigeration and air-conditioning markets, including automotive HVACs. Further, the literature survey indicated that some relevant data with R134a were available from recent publications that might be useful for comparison with the data obtained in the present study.

As mentioned in Section 6.1, it was intended that test data be generated in the range of 30 to 70 C for R134a.Therefore, with a view to use R134a in the system, the test loop was prepared and its parts were pressure-tested up to 400 psig pressure. However, it was decided that the second refrigerant to be chosen should have applications at lower saturation pressures such as in electronics cooling. It was also important that this refrigerant should have low environmental impact so that such a refrigerant would be acceptable within environmental regulations anticipated in near future. Table 6.2 contains a comparison of the relevant thermo-physical-environmental properties of a selection of currently available refrigerants with low or zero Ozone Depletion Potential (ODP). In Table 6.2, the properties of water are included for reference. Although water is regarded as one of the best coolants available in nature, due to corrosion and other issues, water is generally not accepted as a choice of refrigerant.

Initially, it was thought that HFE-7100 would be a relevant choice for the second refrigerant, because it is liquid at room temperature and hence useful as a coolant in electronics cooling and other cooling applications that have preference to no using high pressure refrigerants. Furthermore, HFE-7100 has been categorized as a replacement fluids for several phased-out refrigerants and also has comparable or better heat transfer

properties, compared to other liquids of its category. Additionally, HFE-7100 is a low-GWP (Global Warming Potential) substance and is already accepted as a dielectric fluid now commonly used for miniature liquid cooling loops e.g. those for power electronics. However, during trial runs in the apparatus, it was observed that there were several drawbacks for using this refrigerant in the present setup. First, the refrigerant was reported to have significant affinity for absorbing and retaining moisture from the atmosphere. Since the saturation pressure of the refrigerant at 30 C is below normal atmospheric pressure, a portion of the desired test conditions would require the setup to be run under partial vacuum conditions for which the apparatus would need additional instrumentation and arrangements. First, this increased the possibility of leakage of atmospheric air into the system which would be difficult to detect. Second, this fluid has high viscosity and consequently would exhibit high pressure drop in the system for the flow ranges desired. Since its saturation temperature is very sensitive to pressure, it was estimated that there would be significant variation of saturation temperature (as much as 10 to 15 C across the channel) for this fluid when high mass flux tests were to be conducted. In such a situation, it would be difficult to obtain the desired operating saturation conditions with this fluid. Also, it affected the calculation of heat transfer as wall axial conduction would dominate due to a wide variation of saturation temperature.

For these reasons, HFE-7100 was rejected as a choice for the working fluid.. Eventually, a new low-to-intermediate pressure refrigerant, R245fa was selected for study. Its ODP is zero and GWP is less than that of R134a and its operating saturation pressures were lower than R134a.

Table 6.2: Comparison of thermo-physical-environmental properties of some common refrigerants

	HFC-134a		HFC-125		HFC-143a		HFE-7000		HFE-7100		Water[*]
Saturation Temperature (^{o}C)	30	70	30	60	30	70	25	34	30	61	100
Saturation Pressure (bar)	7.71	21.18	15.68	31.71	14.35	28.77	0.695	0.969	0.3415	1.045	1.013
Liquid Density (kg/m^3)	1187	996.3	1159	870.3	908.4	728.9	1414	1388	1455	1369	958.4
Liquid Absolute Viscosity (cP)	0.01827	0.01065	0.01259	0.00636	0.01162	0.005391	0.04251	0.03798	0.06556	0.06	0.02819
Liquid Surface Tension (Dynes/cm)	7.42	7.148	3.261	3.261	4.068	4.068	12.4	12.4	13.6	136	5.891
Liquid Specific Heat (kJ/kg.K)	1.446	1.804	1.462	3.247	1.722	2.712	1.088	1.388	1.134	1.158	4.217
Heat of Vaporization (kJ/kg)	173.1	124.3	104.6	51.78	152.5	94.01	135.3	132.7	120.9	111.2	2257
Liquid Thermal Conductivity (W/m.K)	0.081	0.059	0.058	0.043	0.068	0.05679	0.07426	0.0725	0.06785	0.063	0.6651
GWP ** (100 year ITH)	1600		3800		5400		350		280		N/A
Atmospheric Lifetime (years)	13.6		32.6		53.5		4.9		4.1		N/A

* For comparison purposes only
** Global Warming Potential – 100 year Integrated Time Horizon.

Further, its thermal properties are comparable or better that R134a. These reasons make R245fa a competitive choice as a future replacement of R134a. Table 6.3 provides a comparison of the thermo-physical properties of R245fa with R-134a.

Table 6.3: Comparison of thermo-physical properties of the two working fluids used in the present study

	T_{sat} (^{o}C)	P_{sat} (kPa)	Density (kg/m^3)	Enthalpy (kJ/kg)		Viscosity (µPa.s)		Surface Tension (mN/m)
			liquid	liquid	vapor	liquid	vapor	
R-134a	30	770	1187.5	241.7	414.8	185.8	12.04	7.42
	70	2116	996.2	304.3	428.7	106.4	14.65	2.61
R-245fa	30	179	1325.1	239.6	427.5	376.4	10.51	13.41
	70	610	1204.7	295.7	456.6	226.8	12.0	8.35

6.6 SUMMARY

The present chapter describes the details of design and fabrication of the experimental apparatus and the calibration of various instruments. Various design concepts were presented and logical choices were made in creating the final form of the experimental setup. The chief criterion in the design was to contain the error in energy balance and heat transfer coefficient estimates in the data. To that end, several modifications were incrementally made to the design to improve accuracy and data repeatability. The various parts and instruments used in this apparatus are commonly available and hence this apparatus may be reproduced with ease. This chapter also contains a brief description of the thought process of the selection of the two working fluids used in this study.

Chapter 7

EXPERIMENTAL RESULTS

7.1 INTRODUCTION

In this chapter, the experimental procedure and data reduction process will be described, following which the data on heat transfer coefficient and pressure drop will be presented for the two fluids R134a and R245fa.

Since different researchers have adopted various experimental apparatus and investigative techniques, it is essential to understand both the process adopted in consistently executing the experiment in the experimental domain and also the data reduction technique that was used subsequently. A few data sets that have been found to be available in the literature contain data on investigation of condensing flows of R134a in micro-channels of similar size to that presented in this work. Although the experimental conditions of these data sets was not closely matched to those in this work, nevertheless, a comparison has been made with those data sets to assess the proximity of the results, since, as has been noted earlier, several investigations have found widely varying and even opposite results from similar test conditions. A comparison of the data with correlations based on data from conventional diameter channels and micro-channels will be made to show the applicability of available correlations.

7.2 EXPERIMENTAL PROCEDURE

An experimental procedure had been adopted to consistently execute all test points in the experimental domain. The procedure involved controlling and/or monitoring *four* experimental parameters/inputs during a test:

a) Refrigerant Flow rate (INPUT)

b) Refrigerant-side heat input (to the evaporator) (INPUT)

c) Water flow rate (INPUT)

d) Water inlet temperature (CONTROL)

The steps of the experimental procedure are presented below:

1. Determine desired inlet condition to the condenser (i.e., saturation temperature, vapor quality, degree of superheat) and desired refrigerant mass flux.

2. Switch on the refrigerated bath/circulator and provide coolant flows in the condenser and the sub-cooler.

3. Provide input to the PID controller for the reservoir heater to maintain a steady system pressure equal to the desired saturation pressure in the system. Provide input to the micro-pump to create a steady refrigerant flow in the loop to maintain the desired refrigerant mass flux. Provide input to the PID controller that controls the input to the heater on the refrigerant line located upstream of the evaporator so that a steady sub-cooled liquid temperature is established and maintained at the evaporator inlet through out the execution of the test point. Then provide input to the evaporator heater by controlling the power level to the desired value to maintain the refrigerant thermal condition desired at the inlet of the condenser. Also provide heat input to the copper elbow heat shield to keep its temperature close to the desired temperature of

the refrigerant at the condenser inlet. Thus the average temperature of the copper heat shield is closely maintained at the refrigerant saturation temperature, and hence reducing the convection losses from the refrigerant line in this region.

4. Observe prevailing refrigerant saturation temperature (T_{sat}) and sub-cooled evaporator inlet temperature ($T_{evap,in}$) and review these inputs to maintain the desired condenser inlet condition.

5. Calculate the amount of heat that would have to be extracted from the refrigerant flow in the condenser in order to achieve full thermodynamic condition i.e. $x_{th} = 0$) at the condenser outlet. Also calculate the corresponding flow rate of coolant water required if the difference between the coolant inlet and coolant outlet temperatures is kept at 2 C (in some cases 2.5 C due to a limitation of the apparatus for water mass flux).

6. Determine whether the range of the low-flow or high-flow meter is suitable for the above coolant flow rate. Apply this coolant water flow rate with the appropriate choice of water flow meter and monitor the steadiness of the flow continually. The only remaining parameter to be controlled is coolant water inlet temperature.

7. Increase or decrease the set-point temperature of the refrigerated bath/circulator to a desired level. Then control the coolant heater power input to get a steady state temperature difference of 2 C between the inlet and outlet of the coolant stream in the condenser.

8. Monitor all inputs and outputs until steady state is reached. Capture the data for 10 minutes and transfer it to a computer for analysis while the system remains at steady state. While the system is in operation, calculate the inlet and outlet thermodynamic states of the refrigerant. If the calculated values are sufficiently close to the desired conditions, the experiment is concluded. Otherwise perform adjustments to the inputs and capture a new set of data. Repeat this process until a desired condition is reached.

7.2.1 DEFINITION OF THERMODYNAMIC STATE OF CONDENSATION

Two definitions for completion of condensation at the condenser outlet can be adopted:

- *Thermodynamic* state of condensation – The calculated vapor quality at the condenser outlet is 0%. That is, the calculated enthalpy at the condenser outlet is equal to enthalpy of the saturated liquid. In this case, at the condenser outlet, small vapor bubbles will exit the condenser channel along with sub-cooled liquid, and, if an adiabatic flow section is provided after the condenser, these bubbles will eventually collapse to form complete liquid, without further heat extraction.

- *Visual* condensation – The fluid refrigerant at the outlet of the condenser channel is liquid and completely devoid of bubbles, which is verified visually in the sight glass. However, in this case, the refrigerant at the outlet of the condenser channel is sub-cooled, and the calculated value of outlet quality is *negative.*

From preliminary experiments, we have seen that, irrespective of the choice of refrigerant mass flux used for the test, the heat transfer coefficient, and to some extent the

channel pressure drop, are measurably different for the above two cases (about 20-30% change to average heat transfer coefficient value). The reason is that in the case of visual condensation, the end portion of the condenser is used for sufficient sub-cooling (beyond thermodynamic saturation state) so as to condense the bubbles completely before they leave the channel. Thus this end portion of the channel contains smaller vapor bubbles and larger slugs of liquid, and the rate of heat transfer (also pressure drop) is predominantly from single-phase liquid which is less than that for two-phase flow. Also, by decreasing the coolant temperature overall, the condensation rate is enhanced along the entire length of the channel, which increases the length of the condenser channel containing low quality liquid flow (x < ~ 0.1).

Hence, it is crucial to consistently adopt *one* of the above definitions for completion of condensation. Because the rates of outlet sub-cooling and the collapse of remaining vapor bubbles depend largely on outlet header design, the definition of *visual* condensation will not be an objective one. Therefore, any data collected, based on visual condensation will not be helpful for future design requirements. Hence, we adopt the definition of *thermodynamic* state of condensation to be appropriate for our investigation.

7.3 EXPERIMENTAL DOMAIN

The experiments conducted with the two refrigerants R134a and R245fa as working fluids are summarized in the Table 7.1. Results are given for tests with R134a for condenser inlet conditions at several different qualities, two different mass fluxes and at different inlet superheats. However, for the refrigerant R245fa only the tests with fully

saturated or superheated vapor inlet conditions were conducted, since no available data or correlations have been reported for this relatively new refrigerant.

Table 7.1: Domain of experiments with R134a and R245fa as working fluids

	R134a	R245fa
Refrigerant Mass Flux ($kg/m^2.s$)	150, 200, 300	50, 100, 150, 200, 250
Refrigerant Saturation Temperature (^{o}C)	30, 40, 50	30, 40, 50, 60, 70
Refrigerant Condition at Inlet	$x_{inlet} = 0.2 - 1.0$	Superheat = $0 - 20^o$C
	Superheat = $0 - 15^o$C	

7.4 ENERGY BALANCE OF EXPERIMENTAL APPARATUS

The system energy-balance is expressed as a percentage of the heat input to the evaporator, as shown in the Equations 7.1 and 7.2, where $Q_{parasitic-loss}$ represents the net value of heat losses and/or heat gains to the system shown in Fig. 7.1.

$$Q_{in} + \dot{m}_{ref}\left(i_{ref_1} - i_{ref_3}\right) = \dot{m}_{water}\left(i_{water,in} - i_{water,out}\right) + Q_{parasitic-loss} \tag{7.1}$$

$$EB\% = \frac{Q_{parasitic-loss}}{Q_{in}} \times 100 \tag{7.2}$$

The error in the system energy-balance can have different values under different conditions of input parameters as described in the experimental domain. For example, at low heat input ($x_{inlet} = 0.2$) or low water inlet temperature (significantly below room temperature), the energy balance error can be significant. In order to determine the range and trend of variation of the error in energy balance, a series of experiments was conducted varying one of the input parameters and keeping the others fixed.

Several other experiments were also conducted close to settings required for data points (*ref.* Table 7.1). However, the percentage error in energy balance was found to vary, however, consistently within ± 6%. The absolute value of the percentage energy balance was lower when the heat input requirements were higher. From these experimental tests, we are confident that error in energy balance is between 0 to ±6%.
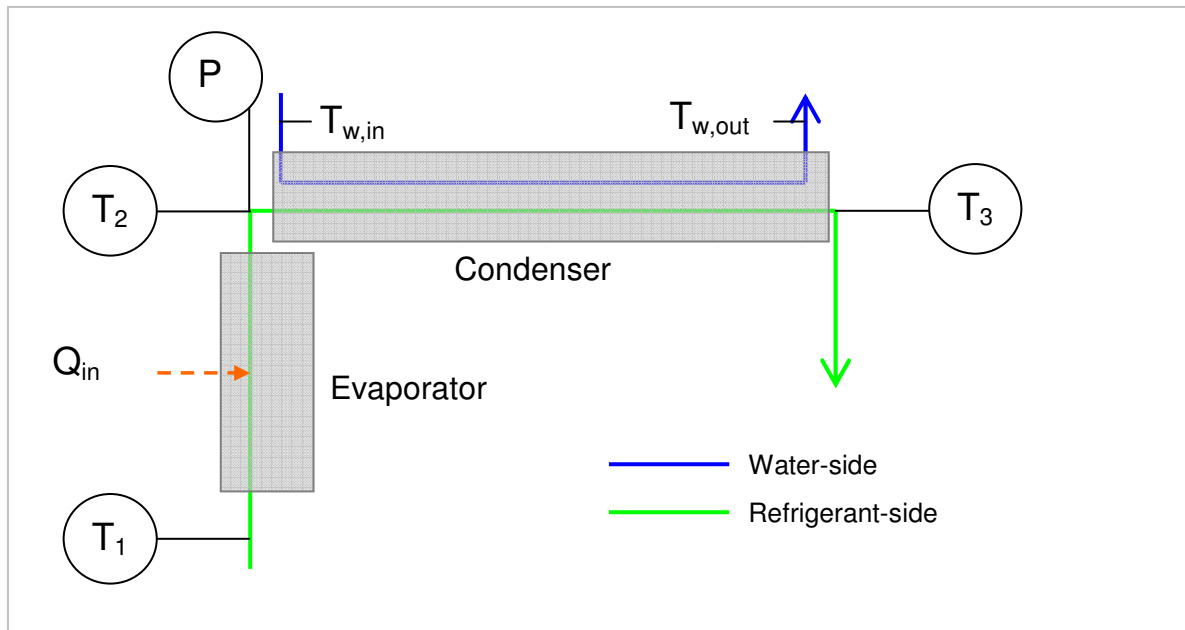
Figure 7.1: Schematic depicting the parameters used for calculating percentage energy balance.

It may be mentioned here that amongst the various parameters measured for energy balance analysis, the parameters which have greatest influence on the energy-balance are the water-side temperatures. Hence, as described in the previous chapter, the water-side temperatures were measured with two Platinum RTD's at each of the inlet and outlet locations to minimize the energy-balance and heat transfer data analysis.

7.5 DATA REDUCTION PROCEDURE AND DATA UNCERTAINTY ANALYSIS

7.5.1 SCHEME FOR FINDING AVERAGE HEAT TRANSFER COEFFICIENT

In this sub-section, the steps for finding average heat transfer coefficient are described. The first task in data reduction is to identify the average *inner* wall temperature and saturation temperature of the refrigerant in the condenser. As described previously in the description of the micro-channel condenser test prototype, there are five thermocouples embedded in the outer wall of the channel, and the wall thickness of channel is 0.002 m. Therefore, the average *outer* wall temperature is given by

$$T_{outer-wall,average} = \frac{\sum_{j=1}^{5} T_{wall,j}}{5} \tag{7.3}$$

where T_j, j=1 to 5 represent the temperature readings of the wall thermocouples.

The *inner* wall temperature must be a value higher than $T_{outer-wall,average}$ due to an outward average heat flux given by

$$q''_{wall-heat-flux} = \frac{Q_{water}}{2(a+b+2t)L} \approx k_{Cu} \frac{\Delta T_{wall-average}}{t} \tag{7.4}$$

where a = 0.0004 m and b=0.0028 m are the dimensions of the rectangular cross-section of the channel, t = 0.002 m is the channel wall thickness, L=0.2 mm is the length of channel and $\Delta T_{wall-average}$ is the approximate estimate of the temperature difference between the outer wall and the inner wall. Therefore, the *inner* wall temperature is given by

$$T_{inner-wall,average} = T_{outer-wall,average} + \frac{t.q''_{wall-heat-flux}}{k_{Cu}}$$ (7.5)

It must be noted here that typically $\Delta T_{wall-average} < 0.2$ C, and hence warrants the approximation in Equation 7.4. The average saturation temperature of the refrigerant is the average of the saturation temperatures at the inlet and the outlet of the channel, the difference of which is a function of the pressure drop in the channel and the nature and operating conditions of the fluid. The outlet saturation temperature is taken as the average of the temperature readings of the three thermocouples in the reservoir, as described previously, and is stated as

$$T_{outlet-saturation} = \frac{\sum_{j=1}^{3} T_{reservoir,j}}{3}$$ (7.6)

where $T_{reservoir, j}$, j=1,2,3 are the readings of the three thermocouples in the reservoir. The average saturation temperature is therefore the $T_{outlet-saturation}$ plus a correction term ($\Delta T_{saturation-correction}$) indicating the influence of the pressure drop. This correction term is found to vary linearly with pressure drop, since the pressure drop is less than 15 kPa and can be considered insignificant.

$$T_{average-saturation} = T_{outlet-saturtion} + \Delta T_{saturation-correction}$$ (7.7a)

where

$$\Delta T_{saturation-correction} = 0.5(T_{saturation}\big|_{P=Pinlet} - T_{saturation}\big|_{P=Pinlet-\Delta Pchannel}) \approx c.\Delta P_{channel}$$ (7.7b)

where $\Delta P_{channel}$ is the pressure drop in kilo-Pascal units and 'c' (in C/kPa units) represents a constant whose value must be identified at each saturation temperature level. Again, this approximation is warranted as there is only a small change in saturation temperature due to channel pressure drop. Next, the average heat transfer coefficient is based on the water-side heat transfer and is given as

$$h_{average} = \frac{Q_{water}}{A_{surface}\left(T_{average-saturation} - T_{inner-wall-average}\right)}$$
(7.8)

where

$$Q_{water} = \dot{m}_{water}\left(\frac{i_{water,out,1} + i_{water,out,2}}{2} - \frac{i_{water,in,1} + i_{water,in,2}}{2}\right)$$
(7.9)

and,

$$A_{surface} = 2(a+b).L$$
(7.10)

Here $i_{water,in,j}$ and $i_{water, out, j}$, j=1,2 represent the water inlet and outlet enthalpy readings from the RTD's. It may be noted here that the water-side heat transfer, Q_{water} is used for calculation of average heat transfer coefficient since the electrical heat input is typically a higher value as it includes the $Q_{parasitic-loss}$. Enthalpies of water are calculated at normal atmospheric pressure neglecting pressure drop in the water jacket. The mass flow rate of water is measured as a function of δ_h (in mm), the difference in heights of the two water columns in the water flow meters and is given by the following correlation equations:

HIGH FLOW (i.e. $\dot{V}_{water} > 120 ml \,/ \min$):

$$\dot{V}_{water-high} = -1 \times 10^{-8} \delta_h^6 + 2.94 \times 10^{-6} \delta_h^5 - 3.5624 \times 10^{-4} \delta_h^4 + 2.169 \times 10^{-2} \delta_h^3$$
$$- 7.2463 \times 10^{-1} \delta_h^2 + 18.2739 \delta_h + 54.0897$$

(7.11)

LOW FLOW (i.e. $\dot{V}_{water} < 120 ml \,/ \min$):

$$\dot{V}_{water-low} = -4.5044 \times 10^{-7} \delta_h^6 + 4.6449 \times 10^{-5} \delta_h^5 - 2.15588 \times 10^{-3} \delta_h^4$$
$$+ 5.7669 \times 10^{-2} \delta_h^3 - 9.5816 \times 10^{-1} \delta_h^2 + 12.51246 \delta_h$$

(7.12)

7.5.2   DATA UNCERTAINTY ANALYSIS

For the analysis of uncertainty, the usual method of root sum square (RSS) of weighted individual parametric uncertainty is adopted. The analysis has been conducted in the Engineering Equation Solver (EES®) software which uses this method as per guidelines given in the Guidelines for Evaluating and Expressing the Uncertainty of NIST Measurement Results, National Institute of Standards and Technology Technical Note 1297, 1994.

If $Y=f(X_j)$, j=1 to n, then the uncertainty of the calculated value of Y may be expressed in terms of the uncertainties in X_j,s as

$$U_Y = \sqrt{\sum_{j=1}^{n} \left(\frac{\partial Y}{\partial X_j} \right)^2 U_{X,j}^2}$$

(7.13)

where U_α represents the uncertainty of the variable $\alpha = Y$, X_j, j=1 to n.

As with the energy balance analysis, the data uncertainty of the computed value of average heat transfer coefficient, taking into account uncertainties of individual parameters, varies from one data point to another. Table 7.2 lists the uncertainties of individual parameters and their impact on the overall uncertainty value. The overall uncertainty values of different test points are different but lie within ±10% band. Accordingly, the test data are reported with an uncertainty of ±10% for all data points

Table 7.2 Uncertainty Analysis of Average Heat Transfer Coefficient (R134a)

Parameter	Uncertainty, $U_{X,j}$	Partial Derivative, $\left(\dfrac{\partial Y}{\partial X_j} \right)$	% of Total uncertainty
a	±0.00004 (m)	-1.27×10^{-6}	4.72
b	±0.00005 (m)	-1.27×10^{-6}	6.68
L	v0.001 (m)	-21561	0.76
t	±0.0002 (m)	18776	0.03
k_{Cu}	±5 (W/m^2.K)	-0.0963	0.00
$\Delta P_{channel}$	±40 Pa	-14.86	
δ_{left}	±0.0005 (m)	86.38	3.39
δ_{right}	±0.0005 (m)	-86.38	3.39
$P_{atmosphere}$	±5 kPa	-2.57×10^{-7}	0.00
$T_{wall, j}$, j =1-5	±0.1 ^{o}C	133	0.33
$T_{reservoir, j}$, j =1-3	±0.1 ^{o}C	-221.7	0.89
$T_{water,in, j}$, j=1,2	±0.08 ^{o}C	-1284	19.17
$T_{water, out, j}$, j=1,2	±0.08 ^{o}C	-1285	19.20
Total:			100
Computed Uncertainty for this test point $h_{average}$: ± 5.77 %			

7.6 EXPERIMENTAL RESULTS WITH R134a AS WORKING FLUID

The experimental data with R134a as the working fluid will be discussed in this sub-section. Specifically, different combinations of four effects that have been studied with this fluid are the effect of change in:

1. inlet quality (0.2 to 1.0)

2. refrigerant mass flux (150, 200 and 300 kg/m^{2}s)

3. refrigerant saturation temperature (30 C, 40 C)

4. inlet superheat (0 to 15 C)

The average heat transfer coefficient and total channel pressure drop will be discussed along with relevant comparisons of the data with literature or available correlations.

7.6.1 EFFECT OF VARIATION IN INLET QUALITY

Figures 7.2 (a) and (b) show the effect of change in inlet quality at three different mass fluxes on the average heat transfer coefficient and overall channel pressure drop, respectively. A cursory inspection of the data reveals that the average heat transfer coefficient values exhibit a fair degree of repeatability within uncertainty margins, whereas the pressure drop values exhibit a higher repeatability. It may be mentioned here that the pressure drop values are averages of instantaneous readings from the differential pressure transducer over the period of data recording. In general, for all inlet conditions, especially for the conditions with inlet quality, $x_{in} < 1.0$, a high but stable fluctuation in instantaneous pressure drop readings was noticed, with amplitudes reaching ~ 2 kPa for

higher flow cases. This was possible due to the influence of in-tube boiling in the evaporator section upstream of the condenser channel. The scale in pressure fluctuations was relatively less for cases with inlet quality of 1.0 or inlet superheat since single-phase vapor may transmit less pressure fluctuation to the pressure port in the condenser channel.

The heat transfer coefficients for different mass fluxes tends to collapse at inlet quality <0.1, since the flows with very low inlet qualities are dominantly forced convective single-phase (liquid) flows. At higher inlet qualities, and especially at and near the channel inlet, the slug-bubble flow pattern is expected, for which the dominant mechanism of heat transfer is the forced-convective effects in the thin liquid films separating the vapor bubbles from the channel wall. Even then a major portion of the channel will still be dominated by liquid slugs between bubbles. The pressure drop data is much more repeatable and coherent. At each quality, the channel pressure drop tends to form a parabolic rise with mass flux. For a given mass flux, especially for 300 kg/m^{2}s, the pressure drop curve indicates a steep rise for initial qualities of $0 \leq x_{inlet} \leq 0.5$. However, at higher qualities the curves tend to flatten. This may indicate that there is a significant change in the flow pattern for low to medium qualities, but at high qualities ($x_{inlet} \geq \sim 0.8$) the flow pattern is essentially stable.

(a)

(b)
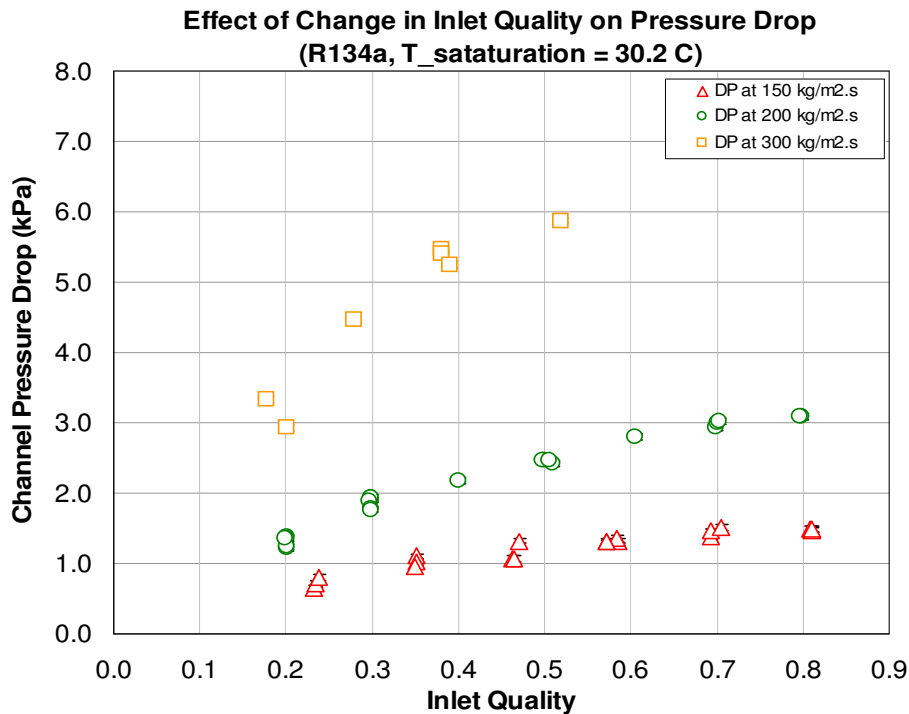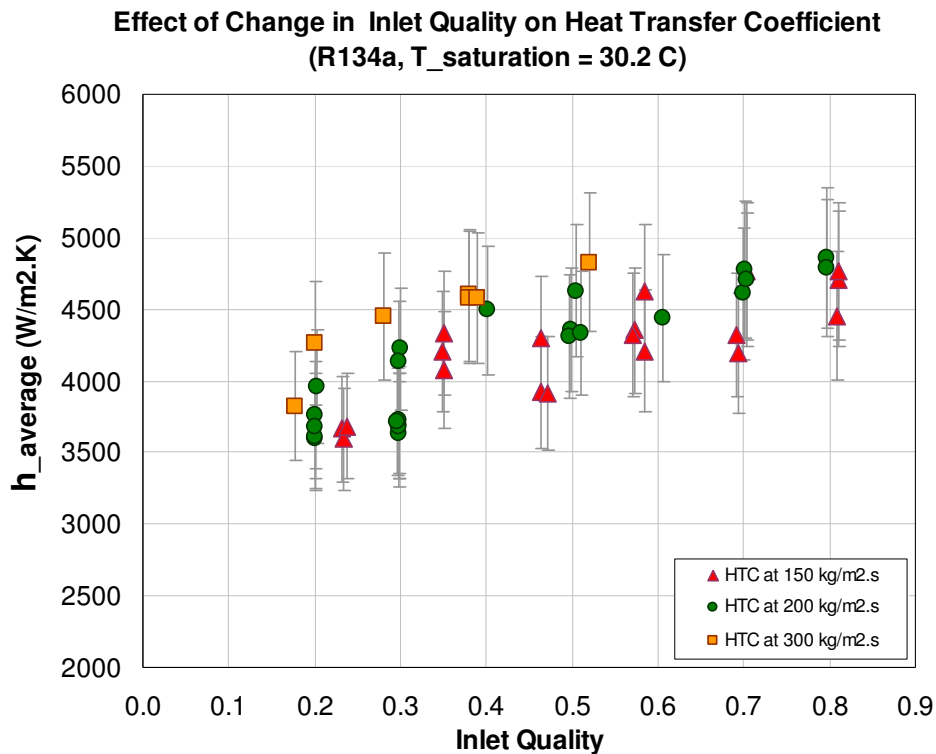
Figure 7.2: Effect of change in inlet quality on (a) average heat transfer coefficient (b) total channel pressure drop (R134a)

Figures 7.3 (a) – (c) show the different wall temperature profiles at different inlet conditions and mass fluxes. Insights into the local heat transfer coefficient along the channel would require the heat flux profile of the channel together with the wall temperature profiles. The heat flux profile is briefly discussed in the next sub-section employing computational techniques.

Wall Temperature Profile at Different Inlet Qualities
(R134a, Mass Flux = 150 kg/m2.s)

(a)

Wall Temperature Profile at Different Inlet Qualities
(R134a, Mass Flux = 200 kg/m2.s)

(b)

**Wall Temperature Profile at Different Inlet Qualities
(R134a, Mass Flux = 300 kg/m2.s)**
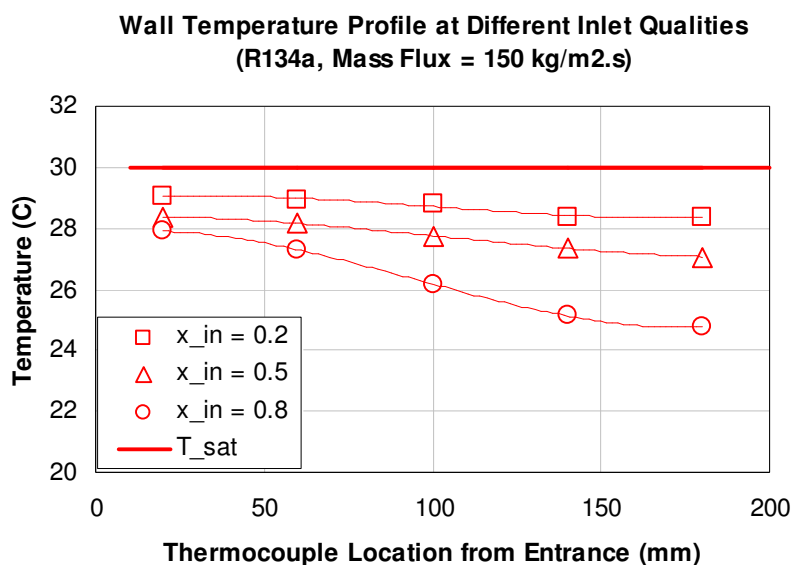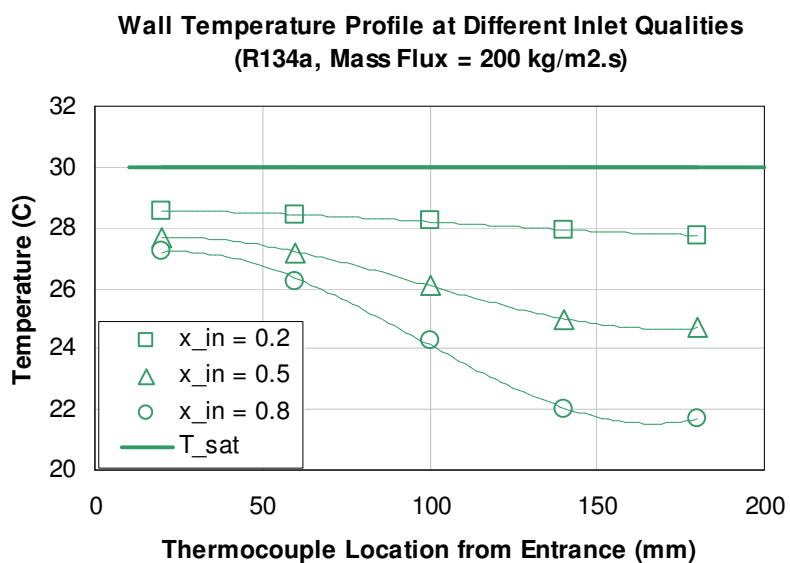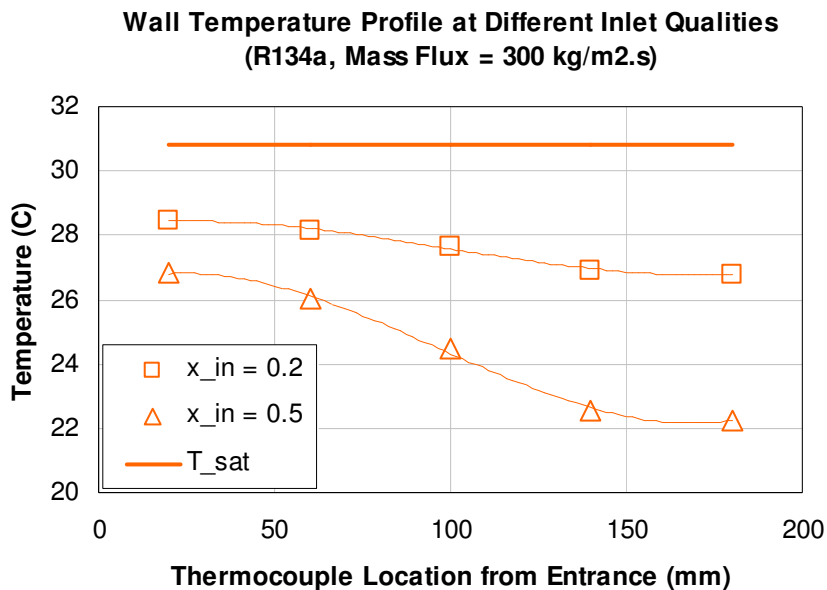
(c)

Figure 7.3: Wall temperature profile at different inlet qualities at refrigerant mass fluxes (a) 150 (b) 200 (c) 300 kg/m^2.s respectively (R134a)

However, here some observations can be made about the temperature profiles. The coolant water flowed in a counter-current direction with respect to the refrigerant, with a net rise of 2 C across the test section which is equivalent to a temperature gradient of 10 C/m, approximately. In the three different mass flow rates that are presented here, for the medium to high inlet qualities (x_{in} > ~0.5), the value of the overall *wall* temperature gradient exceeds the coolant temperature gradient (the difference between the readings of the first and fifth thermocouples is more than 2 C). Therefore, if the coolant were to flow co-currently with the refrigerant, the overall wall temperature gradient could have been reduced. As stated before, one goal was to minimize the wall temperature gradient, since the change in wall temperature can influence the liquid properties of the refrigerant and hence may unduly influence, albeit only slightly, the

condensation phenomenon in the channel. As stated in Chapter 2, some researchers have found weak influence of heat flux on condensation heat transfer coefficients.

7.6.2 EFFECT OF VARIATION IN SATURATION TEMPERATURE

As shown in Figures 7.4 (a) and (b), a relatively smaller sample of test results with two different saturation temperatures were available in the present study to understand this effect for R134a. Across the range of inlet qualities, the effect of this variation on pressure drop is more prominent than on the overall heat transfer coefficient, the latter being observable only at inlet qualities higher than 0.5.

Effect of Saturation Temperature on Heat Transfer Coefficient (R134a, Mass Flux = 200 kg/m2.s)

(a)

**Effect of Saturation Temperature on Pressure Drop
(R134a, Mass Flux = 200 kg/m2.s)**
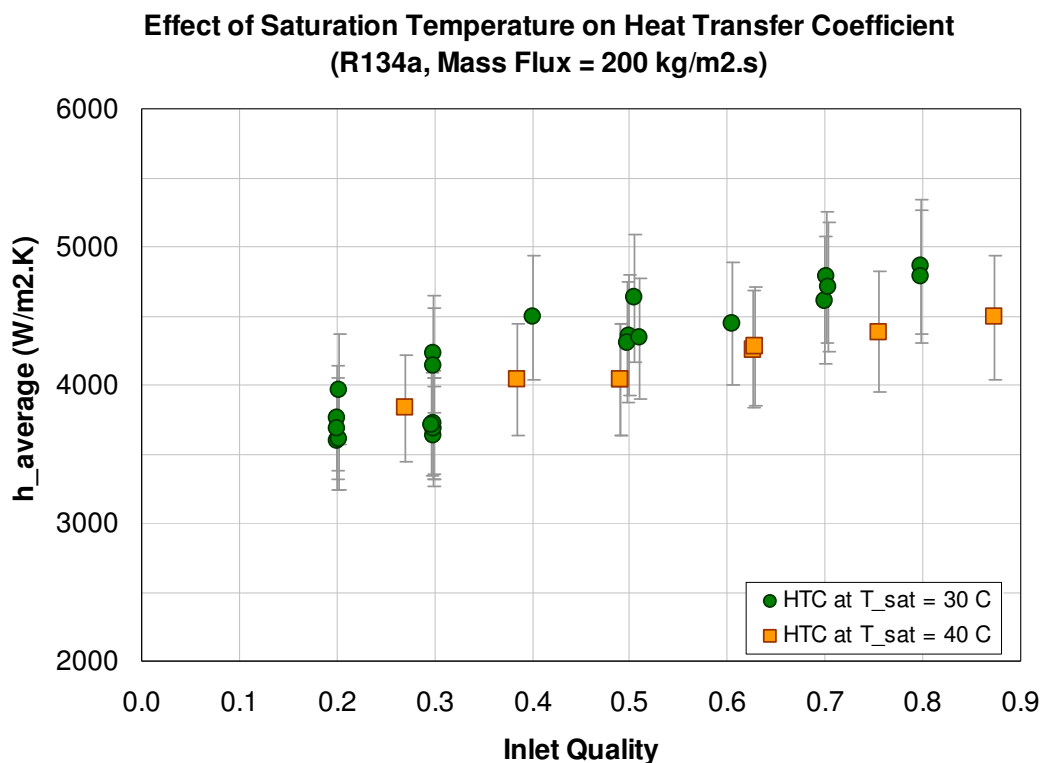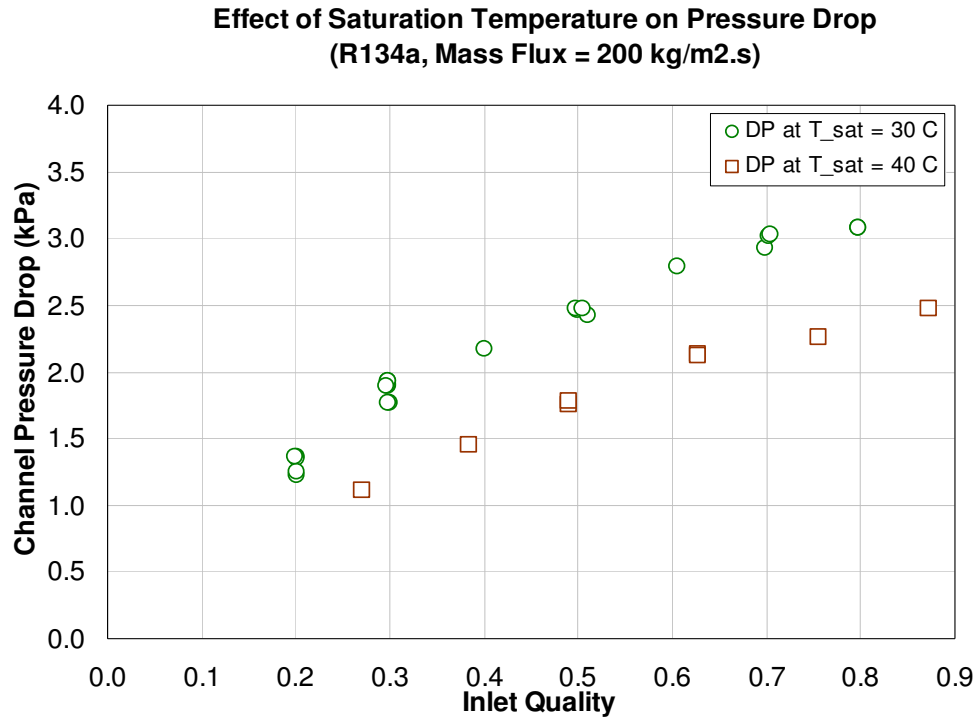
(b)
Figure 7.4: Effect of change in saturation temperature (a) average heat transfer coefficient (b) total channel pressure drop (R134a)

The decrease in heat transfer coefficient and increase in overall pressure drop due to increase in saturation temperature is primarily due to the changes in the Prandtl Number and kinematic viscosity of the refrigerant as shown in Table 7.3.

Table 7.3: Variation of relevant properties with saturation temperature of R134a

$T_{sat}(^{o}C)$	$P_{sat}(kPa)$	$\mu_{liq}(kg/m.s)$	$\mu_{vap}(kg/m.s)$	$\rho_{liq}(kg/m3)$	$\rho_{vap}(kg/m3)$	$Prandtl_{liq}$
20	572.1	0.000207	1.18E-05	1225	27.8	3.392
30	770.6	0.000183	1.22E-05	1187	37.56	3.271
40	1017	0.000162	1.27E-05	1148	50.12	3.192
50	1319	0.000142	1.32E-05	1102	66.32	3.151

7.6.3   EFFECT OF CHANGE IN INLET SUPERHEAT

The effect of inlet superheat is shown in Figures 7.5 (a) and (b). The level of superheat was restricted to below 20 C because it was not advisable to conduct tests with superheat levels beyond 20 C due to the possibility of heater burnout caused by dry-out in the evaporator exit region.

Although sufficient resolution of the wall temperature near the channel entrance is not available, we may suppose that just at the downstream of the entrance, there was a region of single phase vapor cooling zone. In this pure vapor zone, which was experiencing the highest fluid velocity in the entire loop, a thermal boundary layer was established such that the sub-layer of vapor within the thermal boundary layer adjacent to the wall had a temperature sufficiently close to the saturation temperature to precipitate condensation. This was the condensation incipience zone. Subsequent to the start of condensing zone, which marked the beginning of annular flow with a thin liquid layer separating the wall from the vapor, the vapor was more likely to be in a superheated state and would possibly continue to retain superheat up to a certain length downstream before reaching the equilibrium saturation temperature. Downstream of the condensation incipience zone the vapor velocity was significantly high, and the thin annulus of liquid driven by this high vapor shear may experience a high degree of turbulence and therefore exhibit high convective heat transfer. Since the wall heat transfer coefficient may be expected to be significantly high just downstream of the condensation incipience zone, the average temperature of the thin liquid layer of the annulus might be expected to be close to the wall temperature or at-least slightly sub-cooled. The direction of thermal energy transport was from the vapor core to the liquid layer. However, the mass transfer

might not necessarily be in the same direction since some evaporation or re-entrainment of sub-cooled liquid molecules into the vapor stream might take place thereby further driving down the superheat in the vapor core. This is a matter of conjecture in the present context, and although it is not within the scope of this study to understand where and by what mechanism the vapor core temperature would reach the local saturation temperature of the fluid, this is an interesting problem and needs microscopic observations to confirm the 'near entrance' phenomena. The reason the 'near entrance' phenomenon is of concern is because it is influenced by the wall temperature which is subject to variation depending on the choice of the coolant, the local coolant temperature and the mechanism of coolant flow. As mentioned in 7.6.1, the direction of the coolant flow (with respect to the refrigerant flow direction) and the coolant temperature may influence the local wall temperatures and thus alter the condensation process and flow patterns in the interior of the channel.

The first wall thermocouple, located 20 mm downstream to the channel entrance, exhibited a noticeable although small increase in temperature with an increase in superheat. The readings of other wall thermocouples were indistinguishable from their values for saturated vapor inlet condition, as were the pressure drops at different superheats. This indicated that the region of interest was near the entrance and that the flow downstream was not noticeably affected by the inlet superheat. Although limited to the near entrance zone, the significantly high heat transfer coefficient at this location noticeably influenced the overall average heat transfer coefficient value for superheats greater than or equal to 10 C.

Effect of Inlet Superheat on Heat Transfer Coefficient
(R134a, T_saturation = 50.10 C)

(a)

Effect of Inlet Superheat on Pressure Drop
(R134a, T_saturation = 50.10 C)
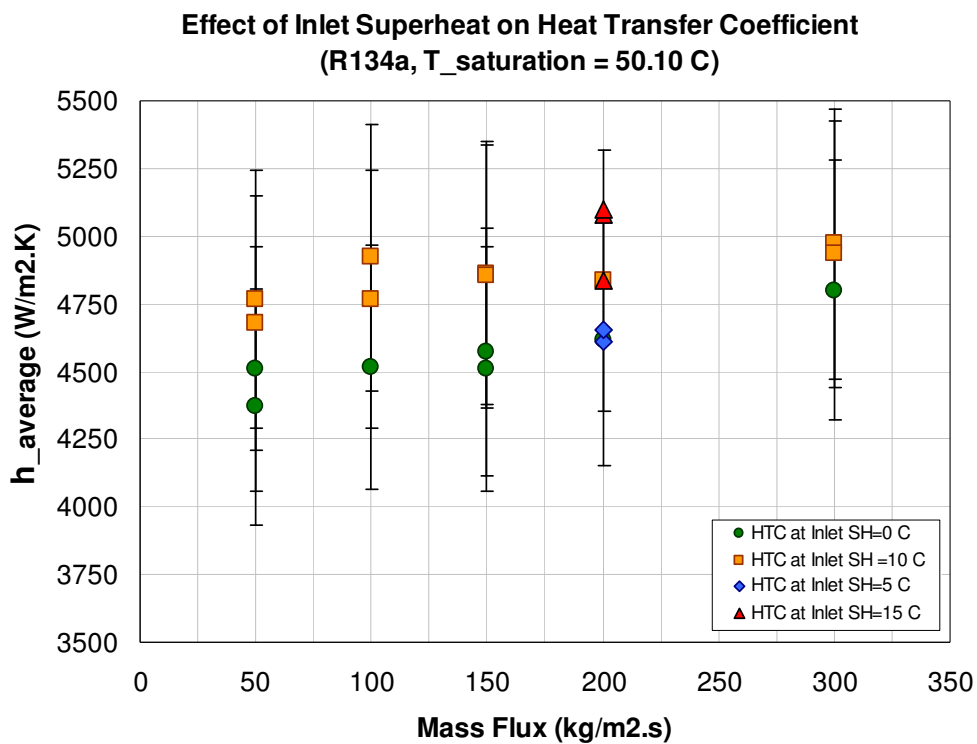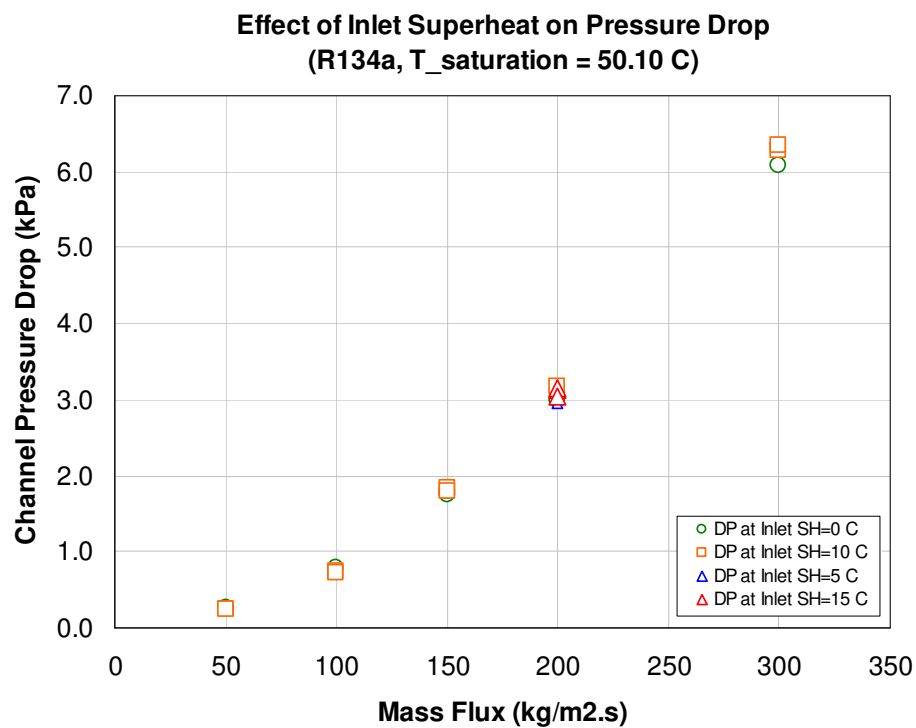
(b)

Figure 7.5: Effect of change in inlet superheat on (a) average heat transfer coefficient (b) overall channel pressure drop. (R134a)

7.6.4. CFD-BASED APPROXIMATE INVERSE HEAT TRANSFER STUDY

A purely 2-D analytical approach was initially attempted to obtain information about the local heat flux profile on the inside walls of the micro-channel condenser. This approach involved inverse heat transfer analysis with the wall temperature profile as one of the source functions. However, this approach required an assumption for the outer wall (i.e. water-side) heat flux or outer wall heat transfer coefficient profile along the channel length. Moreover, the flow in the coolant jacket was not radially symmetric and varied along the channel length which would lead to error. Instead, a CFD-based approach, involving manual iterations was adopted to estimate the desired local heat flux profile for a limited data set. This approach, though laborious and still an approximate estimate, reveals a better understanding of the coolant flow and heat transfer.

Figure 7.6 shows a sketch of a conjugate heat transfer model used for the CFD-analysis. It consisted of the coolant jacket enclosed around the condenser micro-channel. The coolant entrance and exit passages were modeled closely to the actual prototype.
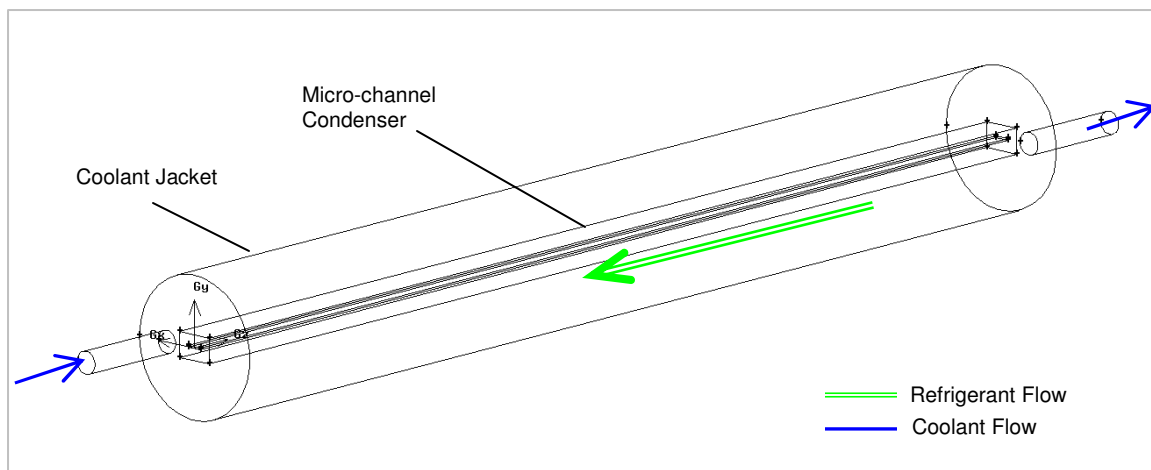
Figure 7.6: CFD-model to study the combination of convective heat transfer in the coolant jacket and heat conduction in the channel wall.

The various surfaces and points used for monitoring and measurements during the post-processing of the CFD results are shown in Figure 7.7. In the CFD model, several temperature monitoring points were chosen underneath the outer surface of the channel. T_a through T_e, respectively, corresponds to the locations of the wall thermocouples T_{w1} through T_{w5} that are embedded in the wall as described in an earlier chapter. $T_{beginning}$ and T_{end} were two fictitious temperature-monitoring points close to the refrigerant entrance and refrigerant exit ends of the channel to complete the temperature profile on the channel surface. Although there are no actual thermocouples at the locations marked by $T_{beginning}$ & T_{end} , the purpose of monitoring the temperatures at these locations is to ensure that the values from the model are realistic.
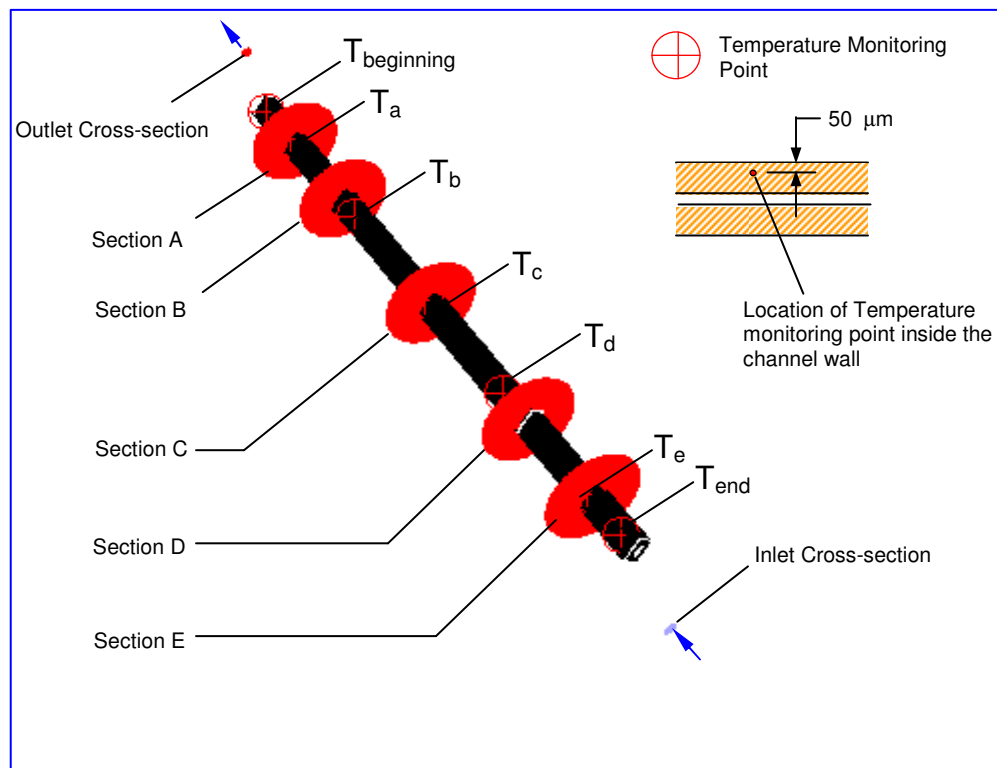
Figure 7.7: Schematic indicating the surfaces and points used in the post-processing analysis of CFD results.

For the purpose of the CFD-based inverse heat transfer study, three relevant experimental test points were chosen, as shown in Table 7.4. These R134a test points represent the effect of variation in refrigerant mass flux on local heat transfer coefficients in the channel and the results may be compared with data from literature.

Table 7.4: A sample of three tests with R134a as working fluid chosen for CFD-based analysis

Simulation ID #	Experimental Inputs		Experimental Results used as Inputs to Computation Model		
	Refrigerant Mass Flux (kg/m^2.s)	Refrigerant T_{sat} (^{o}C) & Inlet Quality (x_{in})	Water Mass Flow Rate (kg/s)	Water Inlet Temperature (^{o}C)	Q_{water} (W)
1	100	50.1 , 1.0	0.0020121	42.12	18.47
2	200	50.1 , 1.0	0.00391773	36.45	34.08
3	300	50.1 , 1.0	0.00485172	30.19	50.68

A CAD-model, as shown in Figure 7.6, meshed with tetrahedral and hexahedral cells, totaling approximately 3.8 million, was created with the aid of Gambit ® software and the analysis was conducted with the CFD software tool, FLUENT ®. The computation involved the conductive heat transfer (in the channel walls) and convective heat transfer (caused by the coolant flowing in the coolant jacket). The wall of the coolant jacket and the walls of the coolant inlet and outlet ports were assigned adiabatic boundary condition. It has been mentioned in an earlier chapter that the inlet & outlet ports of the condenser channel were made with thin-walled stainless tubing to prevent heat leakages into or from the test prototype by wall conduction. Based on this, the faces of the channel at the inlet and outlet were also assigned adiabatic conditions, whereas the surfaces of the channel interior to the coolant jacket (i.e. the outer faces of the channel wetted by the coolant) were exposed to convective heat transfer. The inlet to the coolant jacket was assigned a mass flow boundary condition with a mass flow rate value chosen from the Table 7.4 as per the simulation ID. The outlet to the coolant jacket was assigned a pressure boundary

condition and the coolant-jacket inlet pressure is automatically adjusted during computational iterations to a level that allows the boundary condition coolant mass flow value to reach at the inlet of the jacket.

With the given boundary condition assignments in place, an assumed polynomial profile of refrigerant wall heat flux, as given in Equation 7.14a under condition given in Equation 7.14b, was assigned as a boundary condition on the inner wall of the micro-channel through a User Defined Function (UDF).

$$q' = f(z) = C_0 + C_1 z + C_2 z^2 + C_3 z^3 + C_4 z^4 \quad \text{(W/m)} \tag{7.14a}$$

$$\int_0^{0.2} q' dz = \int_0^{0.2} f(z) dz \approx Q_{water} \tag{7.14b}$$

Thus, the coefficients of the polynomial function, C_j, where $j = 0$ to 4, may vary, but the total heat rejected by the refrigerant will remain *approximately* equal to the heat absorbed by the coolant. A slight difference (within a few percent) between the total heat calculated from the imposed heat flux profile and the Q_{water} value is allowable due to expected inaccuracies in the measurements on the coolant side. Several trials with different heat flux profiles were used for the simulation and the results of the temperature values of the monitoring points ($T_{beginning}$, T_a, T_b, T_c, T_d, T_e, T_{end}) for each were compared with the actual temperatures at those locations. Modifications to the trial profile were made until the output temperature profile closely matched most of the experimentally measured values within ± 0.5 C and in some cases within ± 1 C. Figure 7.8 (a) and (b) show the trial heat flux profiles and the corresponding results of the trial runs for Simulation ID#2 (ref. Table 7.4). The value of $T_{beginning}$ may be expected to be within the range: $T_{sat} \geq T_{beginning} \geq T_{w1}$, whereas the value of T_{end} may be expected to be

close to the value of T_{w5} since the quality of refrigerant near T_{w5} and T_{end} are close to or less than 0.1. Hence the heat transfer gradient was much less compared to the beginning or middle portion of the channel.

(a)

(b)
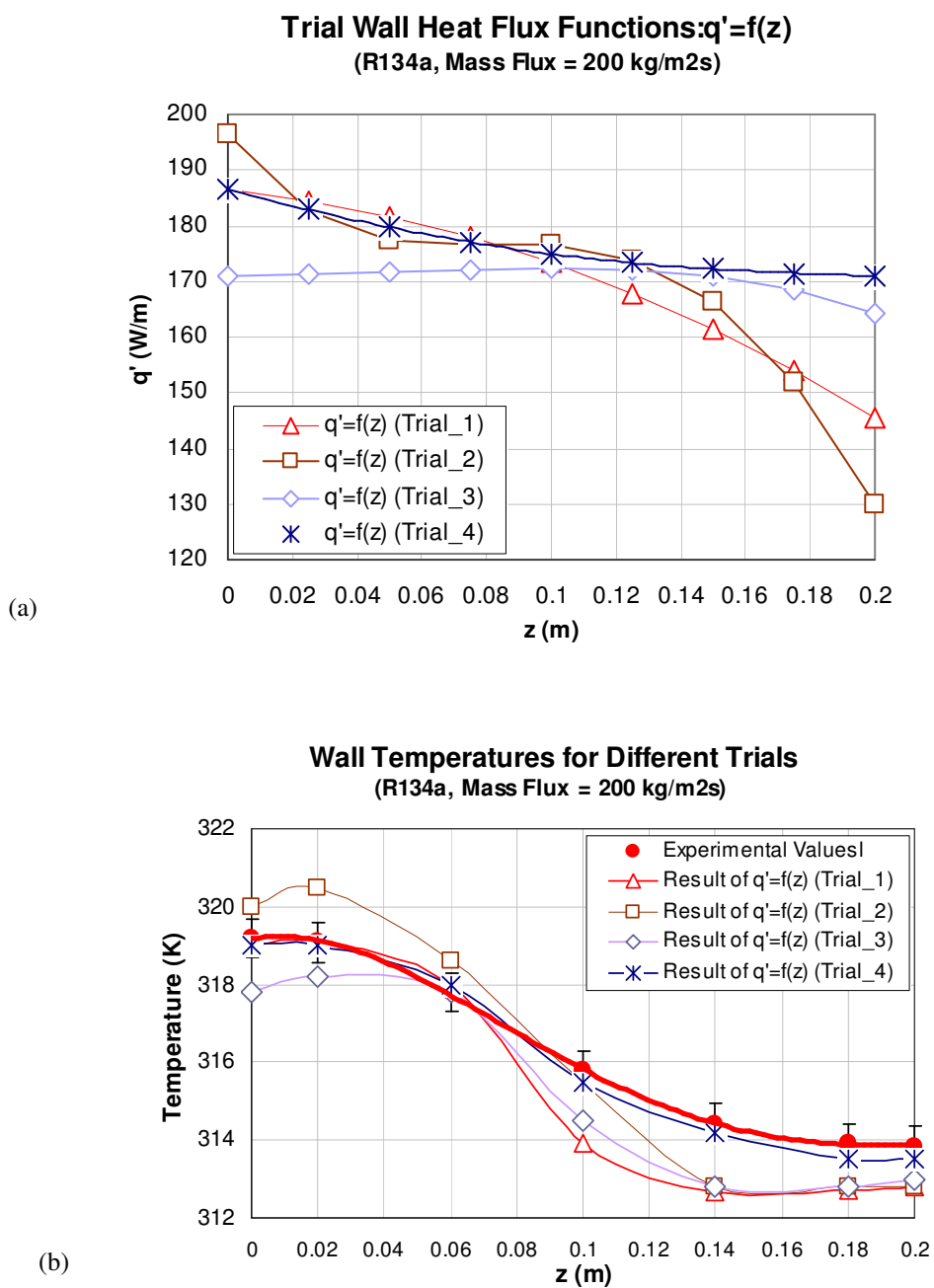
Figure 7.8: (a) Trial heat flux profiles along the channel as inputs to the FLUENT® model (b) Corresponding temperature profile as output to simulation.

Clearly, this numerical simulation technique for solving the inverse heat transfer problem is neither the optimum nor the most precise way to obtain the local heat transfer results. However, the initial scope of this study was to derive average results only and by means of this approximate technique we may have some measure of confidence about the accuracy of the heat balance and results of the heat transfer coefficient. Also, this analysis allows us to compare the results of this study with those that have been reported in the literature, which will be discussed later in this chapter.
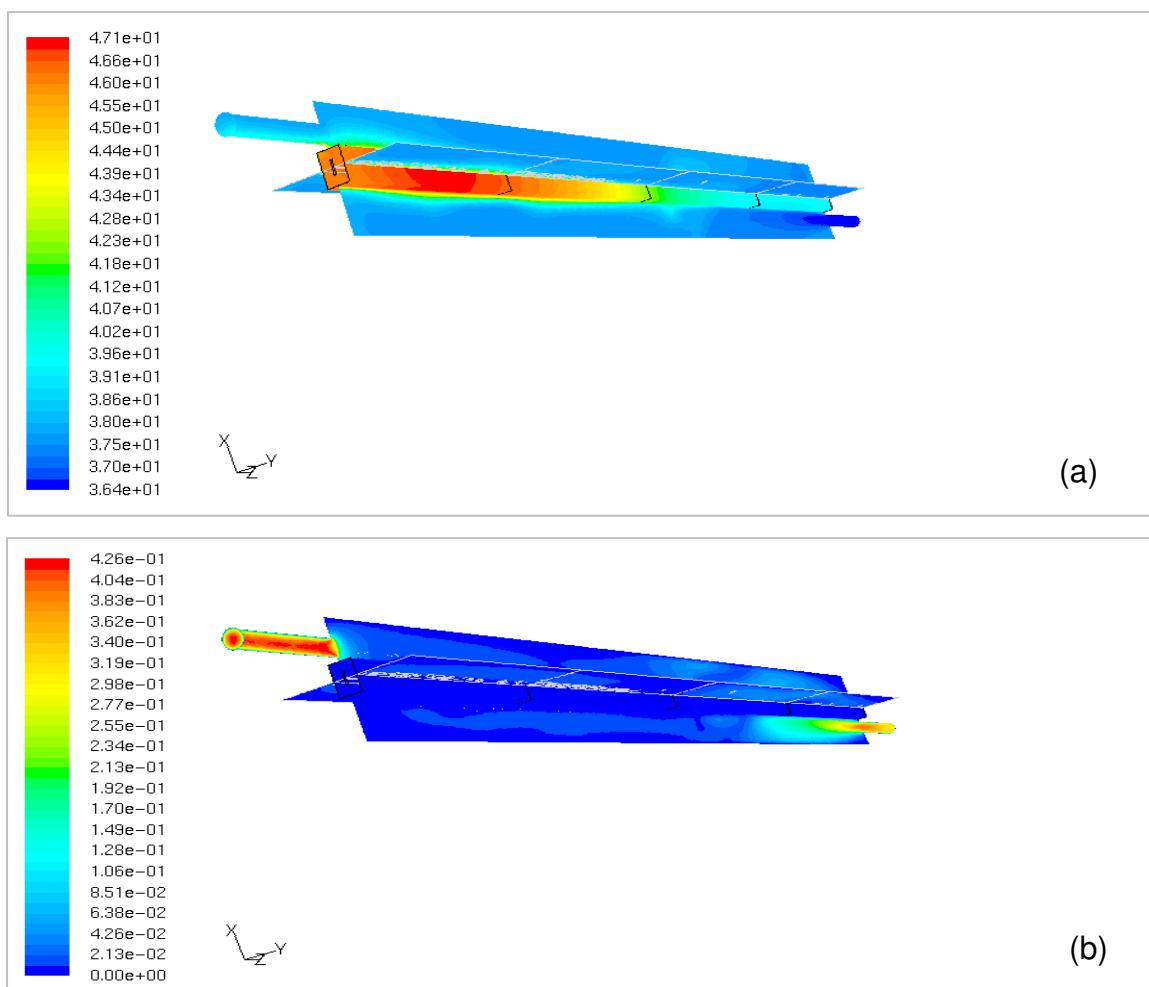
Figure 7.9: Contour Plots of (a) Temperature (in Centigrade); and (b) velocity (in m/s) of the coolant (shown with two orthogonal planes) and the outer channel along the length of the test section

Figures 7.9(a) and (b) show the temperature and coolant velocity contour plots along the entire length of the test section. A careful inspection of Figure 7.9(b) reveals that the highest temperature on the channel surface was not at the refrigerant entrance end but somewhat downstream. This is because the refrigerant entrance end of the channel fell in the 'shadow' of the coolant flow. As shown in Figure 7.10(a), the coolant path-lines (started from the coolant inlet), indicate that the main flow path of the coolant, crossed the channel axis near the temperature monitoring point T_a and approached the coolant exit, nearly missing the refrigerant entrance end of the channel. This caused channel surface in the neighborhood of the point T_a to experience higher heat transfer rate and hence exhibited a slightly higher temperature than the surface region near the point $T_{beginning}$. In fact, as shown by Figure 7.10(b), another view of the coolant path-lines indicate that the coolant flow twisted around the channel near the middle and end portion of the coolant path, thereby locally enhancing the coolant heat transfer coefficient. It may be recalled here that there was a heat flux redistribution effect due to axial and transverse conduction by the copper wall of the channel; this effect was more dominant in the region of higher heat flux gradient which was occurring near the refrigerant entrance end of the channel. The radial conduction effect is captured by the approximation given in Equation (7.5). Figure 7.11 (a) – (b) shows the temperature profile in orthogonal directions across the Section A. Slight asymmetry in the profiles indicate the tortuous nature of the coolant in the jacket. The transverse conduction within the channel wall indicates a difference of less than 0.2C between the outer and inner wall temperatures.
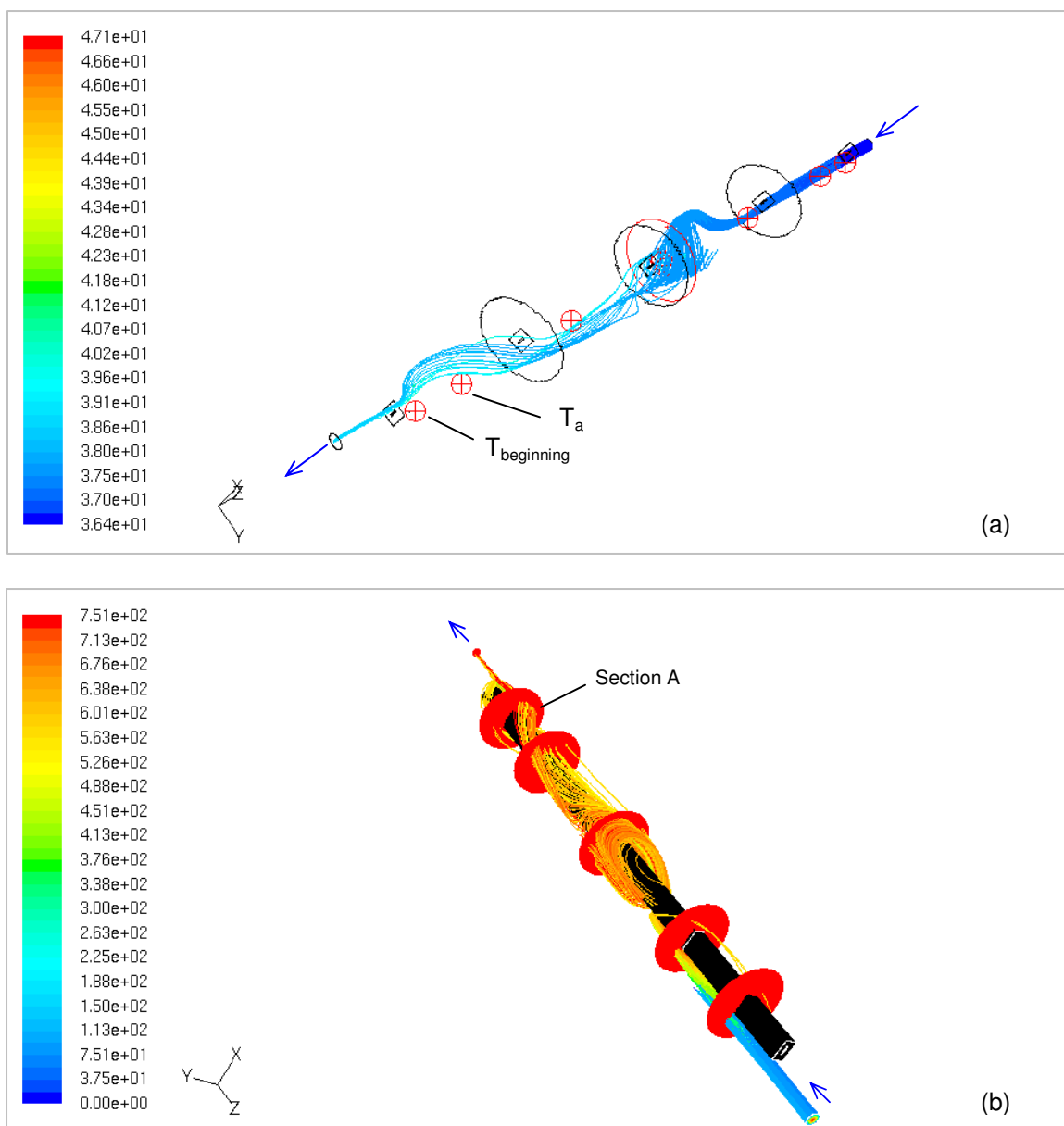
Figure 7.10: Path-line trace for the coolant flow colored by (a) temperature (b) particle ID indicting a twisted trajectory of the main flow of the coolant in the coolant jacket.
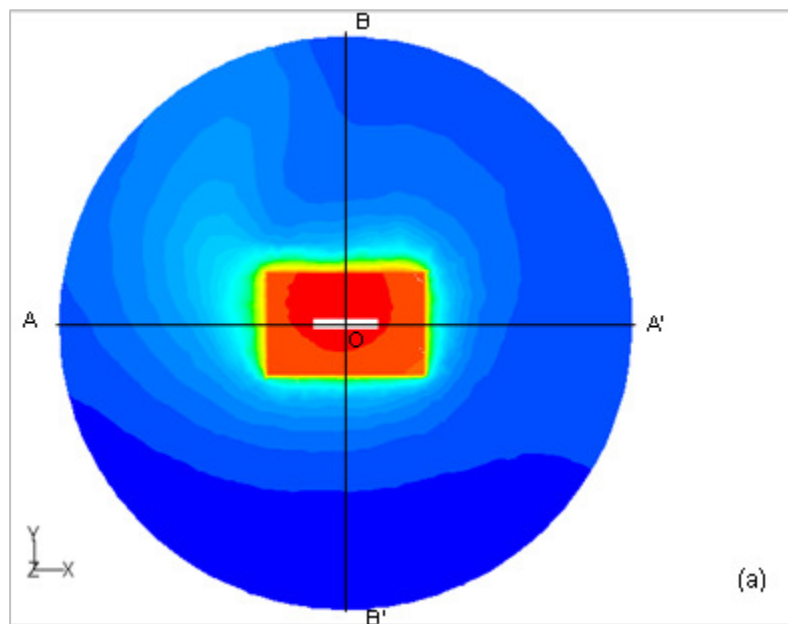
Temperature Plot on Crosshairs in Section A
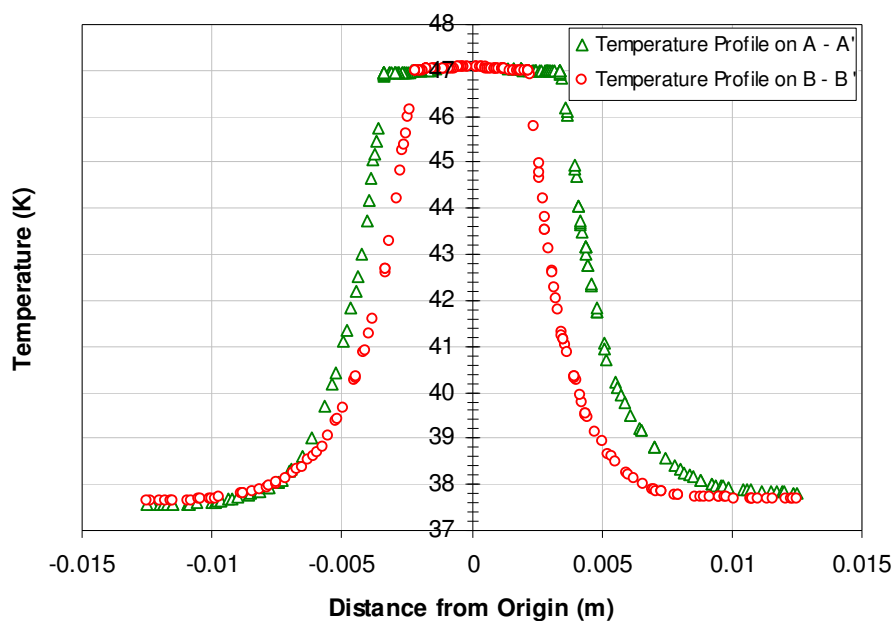
(b)

Figure 7.11: (a) Temperature contour plot (in Section A) and (b) temperature plot on Crosshairs A – A′ and B – B′

It may be mentioned here in the passing that the axial profile of wall temperature in the present study has similarity in trend to that obtained by Koyama et al. [29]. The

difference between their test section and that in the present study is in the length of the condenser channel. Whereas they employed a channel of effective heat transfer length of 0.6 m, the present study has used 0.2 m. The trend in their wall temperature also indicates the low gradients near the inlet and the outlet of the channel.
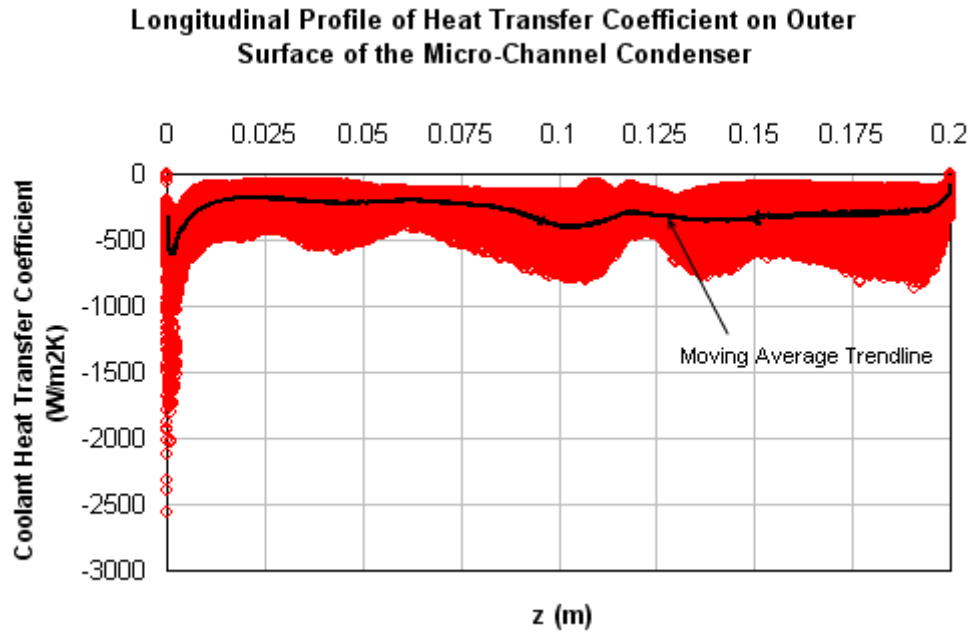
Figure 7.12: Axial profile of the heat transfer coefficient (negative value indicating heat rejection) on the outer surface of the channel wetted by the coolant (Position $z = 0$ m is close to the coolant exit end)

Figure 7.12 depicts the axial profile of the heat transfer coefficient on the coolant-side. For the zone with z: $0 \leq z \leq 0.1$m, the average heat transfer coefficient is lower that that of the other half of the channel. This, combined with the fact that the refrigerant side heat flux as well as the coolant temperature are higher for this zone, explains the change in gradient for the wall temperature profile, which was discussed in Section 7.6.1.

**Comparison of Computed Heat Transfer Coefficient vs. Local Quality with Literature Data
(R134a, Microchannel Dh < 1.0 mm)**
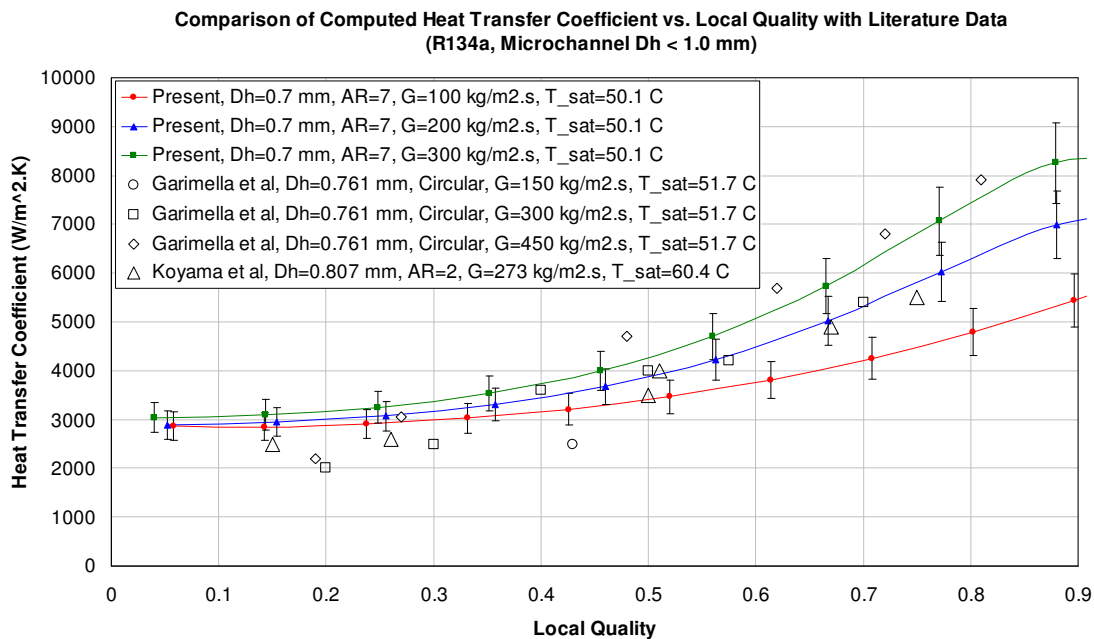
Figure 7.13: Comparison of computer heat transfer coefficient with most relevant experimental data from literature. (R134a)

**Comparison of Different Average Heat Transfer Coefficients
(R134a, T_sat=50.1 C, x_in=1.0)**
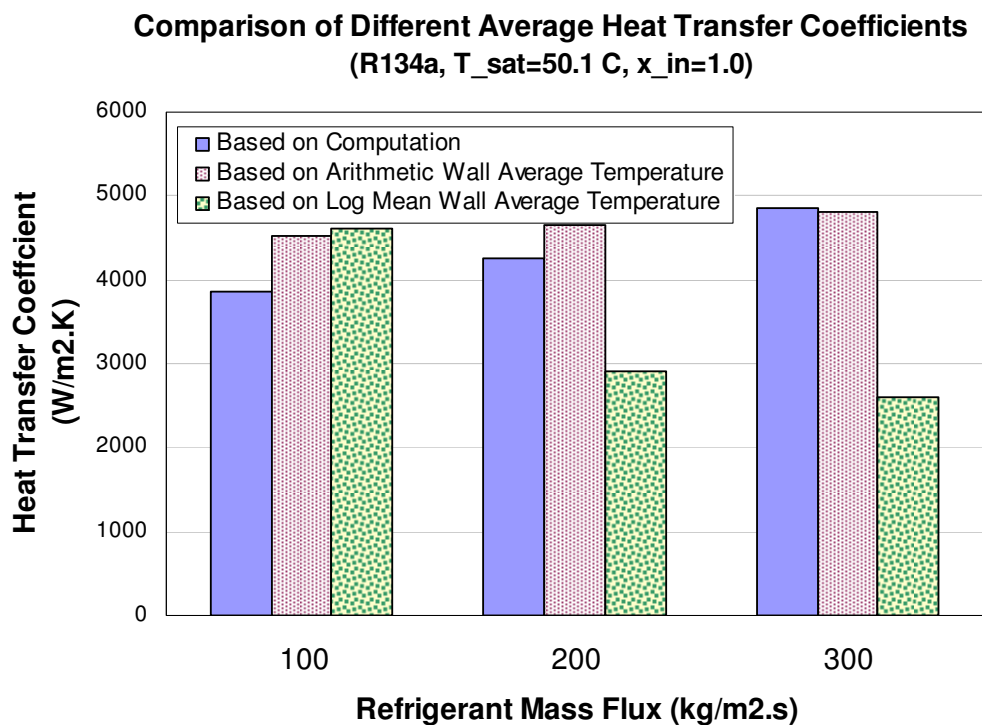
Figure 7.14: Comparison of average heat transfer coefficients from CFD-based technique with values obtained by different wall averaging techniques. (R134a)

From the different Trial runs, we obtained the most likely heat flux profile, say q' = $f_1(z)$ [W/m] on the inner surface of the micro-channel which causes temperature values at the monitoring points in the wall of the model channel to be approximately close to within ±0.5 C for most of the points. From this heat flux profile, and the actual wall temperature profile (from experimental data), $T_w = f_2(z)$, we can easily find the axial profiles of refrigerant quality and refrigerant heat transfer coefficient easily. Figure 7.13 shows a comparison of the computed heat transfer coefficient with the quality. In the same figure, these computed curves are compared with data obtained from literature published by Garimella [35] and Koyama [29].

In case of experiments performed by Garimella et al. [35], extruded micro-channel tubes with each port having a circular cross-section and hydraulic diameter of 0.761 mm were used and inlet and outlet qualities were maintained close to each other and the heat transfer coefficient data was presented against the average quality in the channel. The data was obtained at saturation temperature of 51.7 C, which was close to the present test condition. The test methodology of Koyama et al. [29] is more similar to the present study. They studied the condensation phenomenon of R134a in extruded tubes, with effective length of 600 mm and having rectangular ports of hydraulic diameters 0.807 mm (aspect ratio 2:1), at saturation pressure of 1.7 MPa (T_{sat} = 60.4 C). In their study, the flow of the coolant flow was in opposite direction to that of the refrigerant flow and local heat flux and local wall temperatures were measured along the tube.

Webb et al. [26] have published experimental data for condensation of R134a for micro-finned extruded tubes with hydraulic diameter 0.611 and 0.44 mm. However, the

local heat transfer coefficient data in their publication is limited only to mass fluxes of 600 and 1000 kg/m2.s and only at saturation temperatures of 65 C. Accounting for the difference of the saturation temperatures in their work from that of Garimella et al [35], and the fact that their micro-channel ports have smaller hydraulic diameters and contained micro-fin features, the heat transfer coefficient values obtained by Webb et al. [26] are lower than the data from Garimella et al. [35].

The heat transfer results of a 0.7 mm hydraulic diameter with high aspect ratio of 7.0 may be expected to be higher than data presented in these two studies with similar hydraulic diameters but lower aspect ratios or circular cross-sections, and that is observed in the comparison in Figure 7.13. This is supported by the analytical works of Wang and Rose [42, 43]. However, the general trend in the data is similar and lies within ±10% band as indicated on the computed curves. In case of high aspect ratio such as in the present study, the upper and lower corners of the channel cross-section tend to collect the liquid and thereby tend to stretch thin the liquid film along the longer sides of the channel. This increases the heat transfer coefficient in case of high aspect ratio micro-channels and this phenomenon is also observed in case of forced convective boiling studies as well. However, the effectiveness of the high aspect ratio is only available at millimeter or sub-millimeter scale channels since for larger channels the effect of surface tension to draw away the liquid from the flat wall of the channel to the corner regions is not effective due to larger film radius of curvature at the corners. For high aspect ratio micro-channels, the proportion of the channel length with annular and wavy annular flow pattern may also be expected to be relatively smaller than in the case of the channels studied by Garimella et al. [35] and referred here. Due to the close proximity of the liquid films on the sides of

the channel, the liquid surface instabilities or waves on the films, that are excited due to the difference in the velocities of the vapor in the core and liquid in the film, may lead to 'pinching' or contact of the side-wall films (Teng et al[55]). This bridging vapor leads to formation of slugs and may cause premature formation of large bubbles of vapor each followed by a smaller sized slug of liquid. This is referred to as the plug/slug flow by Coleman and Garimella [22] but it is suspected, in case of high aspect ratio channels, to occur at a quality higher than they expected for their lower aspect ratio channels. The process of formation of the slugs needs to be studied further by microscopic observation of the film thicknesses on the side walls.

The graphical comparison with the available data in literature in Figure 7.13 also reveals that the computed heat transfer coefficients differ with the trend of the data at the low qualities. As mentioned earlier in this chapter, the accuracy in the wall temperature profile segments close to the inlet and the outlet of the channel is wanting and this may result in error at very low and very high qualities.

The definition of average heat transfer coefficient (*ref.* Equation 7.8) used in the present study is based on the arithmetic average of the wall temperatures with the added correction of the transverse wall conduction, as given in Equation 7.5. Cavillini et al [56] used a logarithmic mean temperature difference between the wall and the refrigerant at the inlet and outlet, as given by

$$\Delta T_{\ln} = \frac{(T_{wall,in} - T_{wall,out})}{\ln\left(\dfrac{T_{sat} - T_{wall,out}}{T_{sat} - T_{wall,in}}\right)} \tag{7.15}$$

where $T_{wall,\,in}$ and $T_{wall,\,out}$ are the temperatures of the wall thermocouples embedded in

the wall near the inlet and outlet of the refrigerant flow and T_{sat} is the average saturation temperature. However, in their case the inlet and outlet qualities did not vary as widely as in the present study. This definition of temperature difference, used subsequently in computing the average heat transfer coefficient of the flow at average quality, is acceptable. A comparison of the three techniques for measuring the average heat transfer coefficient is shown in Figure 7.14. The computed average heat transfer coefficient in this graph is based on the computed heat transfer coefficient profile given in Figure 7.13 by the following equation:

$$h_{average,computed} = \frac{1}{L}\int_0^L h(z)dz \tag{7.16}$$

Clearly, due to wide variation of the quality and hence the wall temperature, the logarithmic mean temperature definition is not applicable for the present study. Even the arithmetic mean temperature, though it reflects the trend, does not follow the computed average value at lower mass fluxes.

7.7. EXPERIMENTAL RESULTS WITH R245fa AS WORKING FLUID

Shown in Figure 7.15 – 7.17, the trends in data for R245fa are similar to that presented for R134a. All data for this refrigerant has been taken for conditions with either saturated or superheated vapor at the inlet. A set of relevant property values is presented in Table 7.5. Comparing this with R134a properties given in Table 7.3, it is readily seen that the Prandtl number for R245fa is twice that of R134a at 30 $^{\circ}$C, which is the main reason why the heat transfer coefficient is nearly 50% higher at 200 kg/m^2.s and inlet superheat = 0 $^{\circ}$C. However, this comes with a three times higher pressure drop due to

higher liquid dynamic viscosity (nearly twice that of liquid dynamic viscosity of R134a at 30 C).

Effect of Mass Flux on Heat Transfer Coefficient (R245fa, T_sat= 50 C)

(a)

Effect of Mass Flux on Pressure Drop (R245fa, T_sat = 50 C)
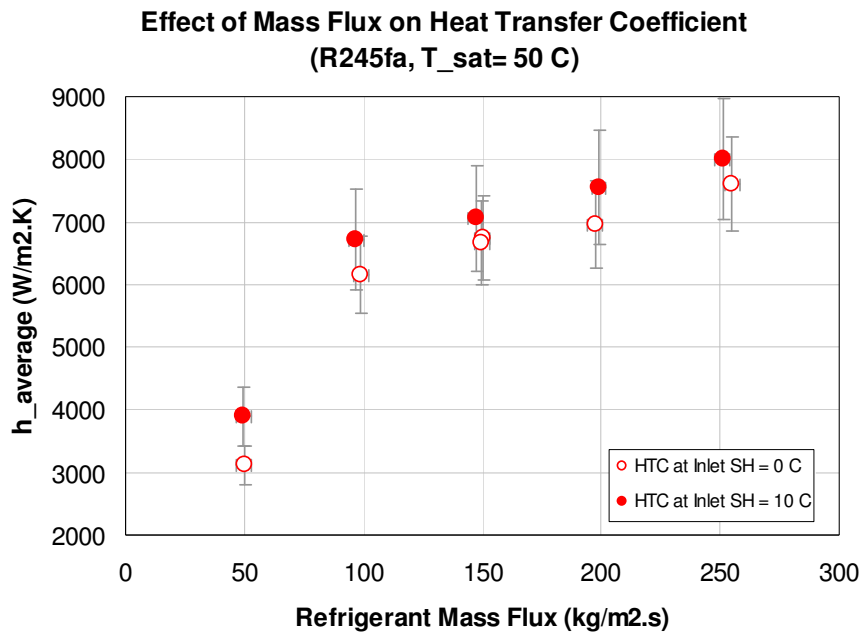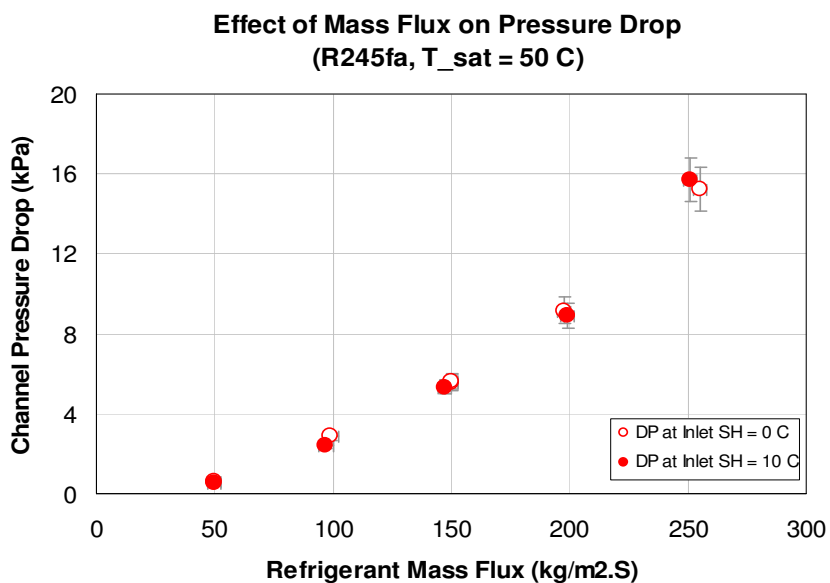
(b)

Figure 7.15: Effect of changing mass flux on (a) the average heat transfer coefficient and (b) channel pressure drop. (R245fa)

**Effect of Inlet Superheat on Heat Transfer Coefficient
(R245fa, T_sat = 50 C, Mass Flux = 200 kg/m2.s)**

(a)

**Effect of Inlet Superheat on Pressure Drop
(R245fa, T_sat = 50 C, Mass Flux = 200 kg/m2.s)**
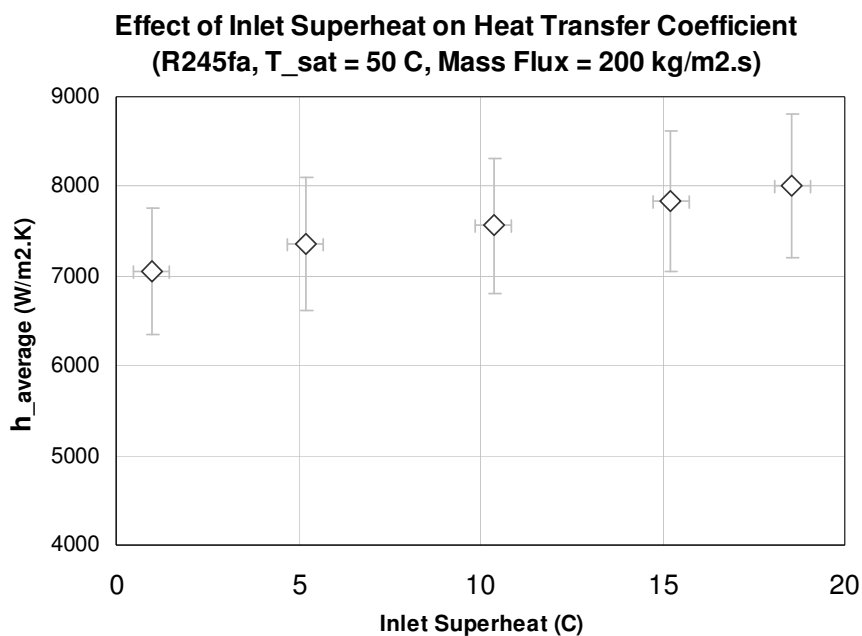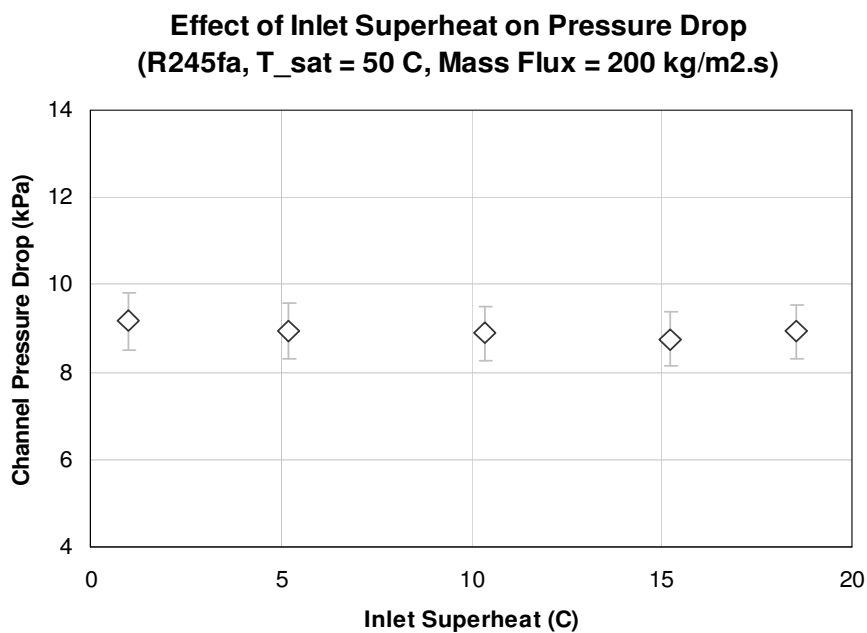
(b)

Figure 7.16: Effect of changing inlet superheat on (a) average heat transfer coefficient and (b) channel pressure drop. (R245fa)

Effect of Saturation Temperature on Heat Transfer Coefficient (R245fa, Mass Flux = 200 kg/m2.s)

(a)

Effect of Saturation Temperature on Pressure Drop (R245fa, Mass Flux = 200 kg/m2.s)
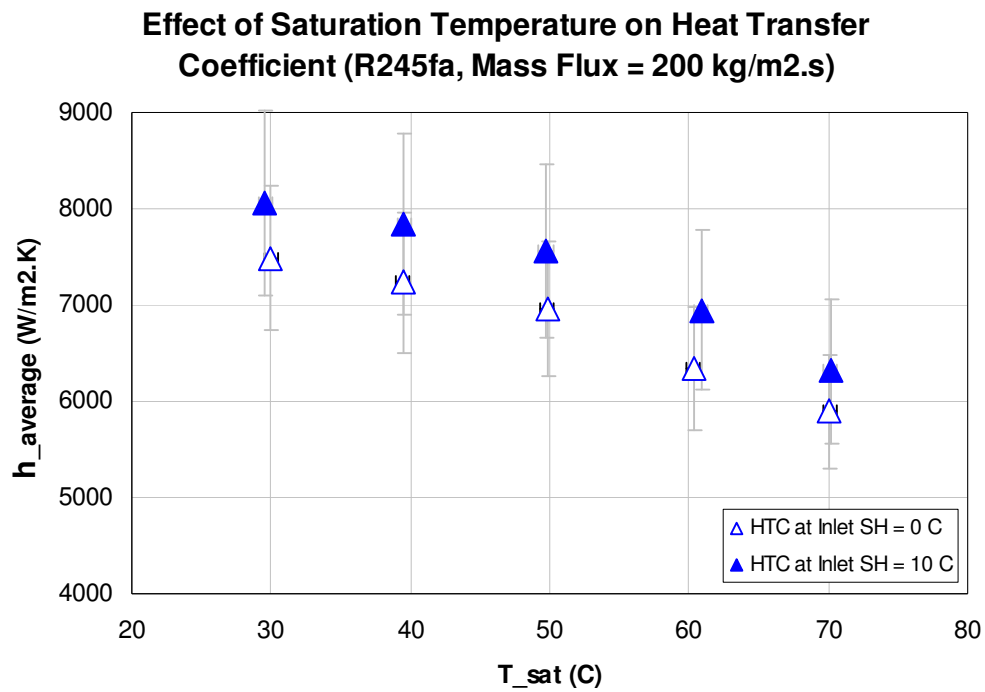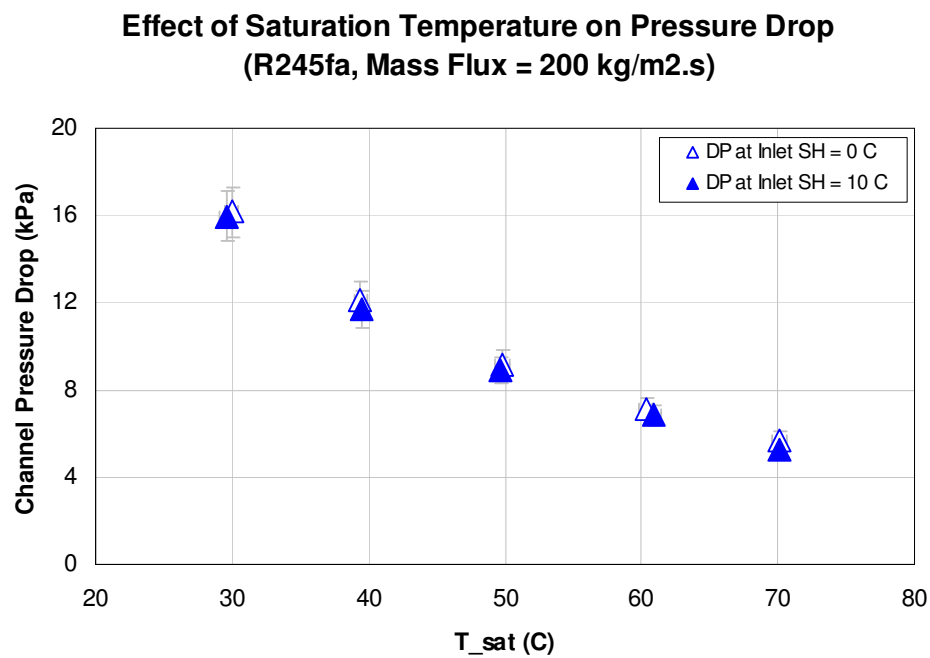
(b)

Figure 7.17: Effect of change in saturation temperature (a) average heat transfer coefficient and (b) channel pressure drop. (R245fa)

Table 7.5: Variation of relevant properties with saturation temperature of R245fa

$T_{sat}(^{o}C)$	P_{sat}(kPa)	μ_{liq}(kg/m.s)	μ_{vap}(kg/m.s)	ρ_{liq}(kg/m3)	ρ_{vap}(kg/m3)	Prandtl$_{liq}$
20	123.7	0.0004356	0.0000104	1352	7.121	7.011
30	178.9	0.0003791	0.00001079	1325	10.11	6.514
40	251.6	0.0003307	0.00001118	1297	14.01	6.059
50	345.2	0.0002893	0.00001159	1268	19.03	5.648
60	463.4	0.0002541	0.00001202	1237	25.41	5.282
70	609.8	0.0002242	0.00001247	1205	33.43	4.961

7.8 COMPARISON WITH CORRELATIONS FOR LOCAL HEAT TRANSFER COEFFICIENT

The three graphs in Figure 7.18 present the comparison of Nusselt numbers at specific vapor qualities against the Nusselt numbers based on the computed data (ref. Figure 7.13). The outstanding feature of these graphs is that for almost all correlations, the correlation predictions for qualities: x<0.1 and x>0.9 suffer significant deviations from the present computed data. As mentioned previously, the computed data is only accurate in as much as the temperature profile near the inlet and the outlet portions of the channel are correctly calculated from the wall thermocouple temperature profile. Hence, there is some ambiguity in this regard for these qualities since thermocouples were not placed close to the inlet and outlet to confirm the temperature profile in these regions. However, it should be pointed out that the heat transfer coefficient for x>0.9 is expected to be higher than that from the computation (Garimella [35]) and hence the two

correlations that seems to correctly capture this trend are the Cavallini[40] and Bandhauer-Garimella[35] correlations. The Koyama [29] correlation, which is a modified version of the Mishima-Hibiki [37] correlation, seems to under-predict most of the local data. It will be discussed in the next section that Koyama et al. [29] have found significant under-prediction of their data for mass fluxes less than 300 kg/m^2.s with the Moser [38] correlation. Cavallini [40] correlation seems to predict the data best, especially for lower mass fluxes and qualities: x>0.3. Since the uncertainty in the computed local data is not clearly understood, further judgment regarding the appropriateness of each correlation will not be made.
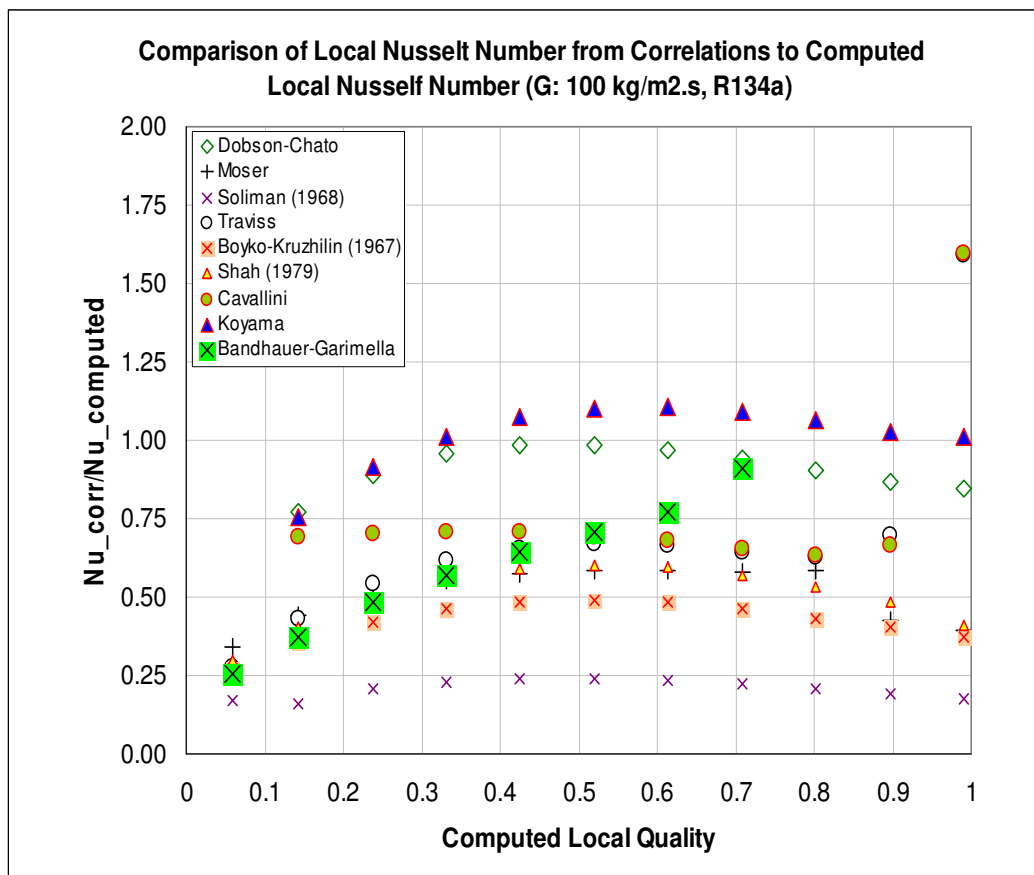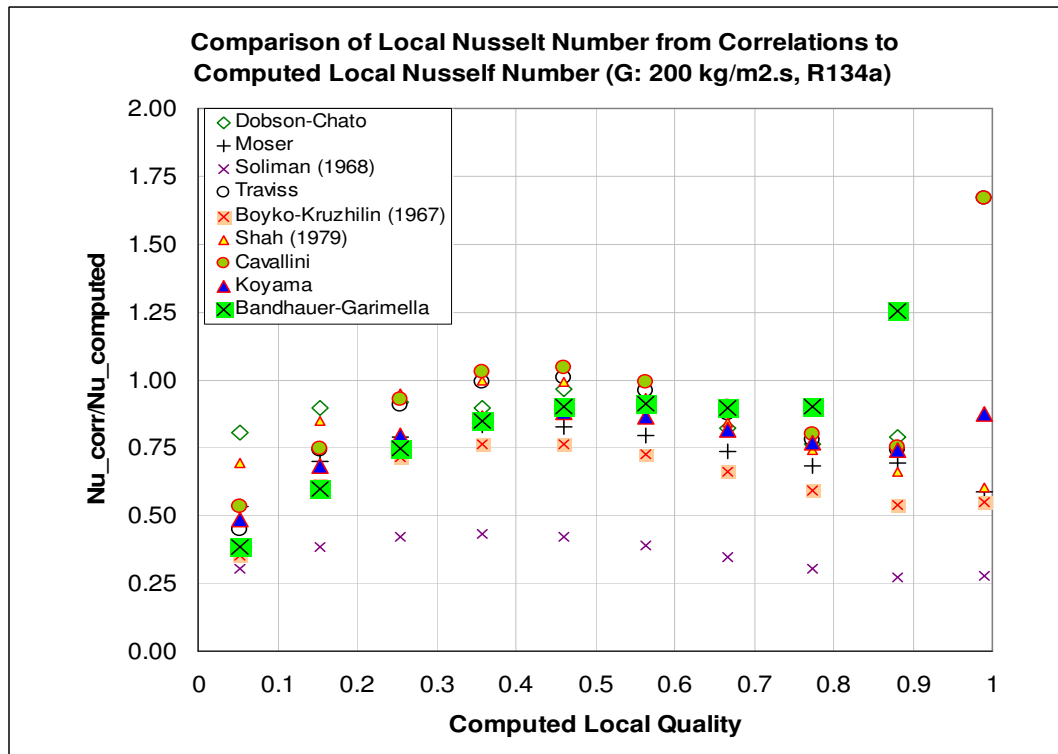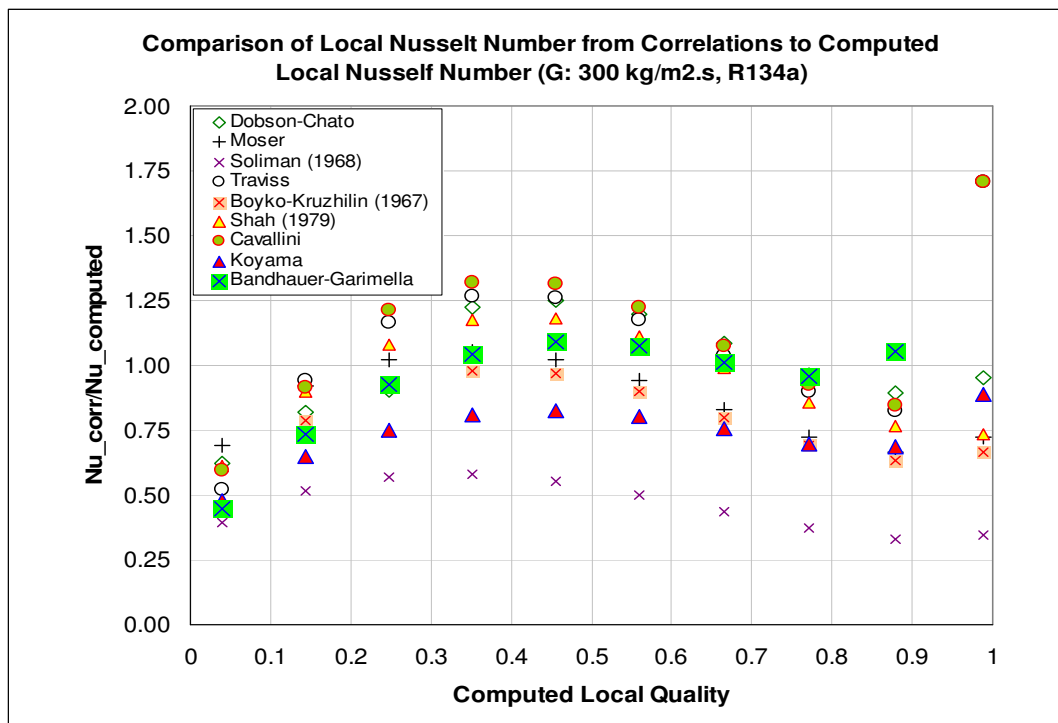
Figure 7.18: Comparison of correlation and computed local Nusselt Numbers (at specific qualities) at different mass fluxes.

7.9 COMPARISON WITH CORRELATIONS FOR AVERAGE CHANNEL NUSSELT NUMBER

7.9.1 *Scheme for deriving the average Nusselt number for a given correlation*

In order to compare with the average heat transfer coefficient data, presented in this chapter, with that from the literature, a scheme is used to find the average Nu from a given heat transfer correlation. In finding the experimental value of the average heat transfer coefficient (and hence average Nusselt number) in the present study, the refrigerant condition is set at the channel inlet and the coolant temperature is varied to reach a saturated liquid state at the channel outlet. Hence, the wall temperature is the variable to be adjusted.

In order to obtain the average Nusselt number from a given correlation, we can assume a similar hypothetical situation in which the desired refrigerant condition is set at the channel inlet and the wall temperature is iteratively varied so that when it reaches a particular value, $T_{wall, avg}$, the total heat transfer is such that the desired refrigerant condition (i.e. saturated liquid state) is reached at the channel outlet. Because the heat transfer coefficient profile of the refrigerant along the channel length is dictated by the correlation, the obtained $T_{wall, avg}$ may be different that the actual experimental value of the average wall temperature.

The situation is illustrated schematically in Figure 7.18. In this schematic, the channel is divided into (n+1) equal segments with length of each segment Δz. Since the inlet refrigerant condition is known (quality x_0: $0 < x_0 \leq 1.0$ & mass flow rate, $\dot{m}_{ref}$), the

heat transfer coefficient at $z = z_0$ can be computed from the given correlation. This heat transfer coefficient value, h_0 may be assumed to be valid for the channel length up to $z = z_1$, if Δz is sufficiently small. Therefore, for a choice of $T_{wall, avg}$, the amount of heat absorbed by the channel wall from $z = z_0$ to $z = z_1$ can be computed from

$$q_0 = h_0 P \Delta z \left(T_{sat,avg} - T_{wall,avg} \right) \tag{7.16}$$

where, P = channel cross-section perimeter = 2 (a + b), with a = 0.0004 m and b = 0.0028 m.

The quality x_1 of the refrigerant at $z = z_1$ can thus be calculated:

$$x_1 = x_0 - \frac{q_0}{\dot{m}_{ref} i_{fg}} \tag{7.17}$$

where, i_{fg} represents the difference of specific saturation enthalpies of vapor and liquid states at saturation temperature equal to $T_{sat, avg}$. The next step is to determine the value of heat transfer coefficient at $z = z_1$ corresponding to quality x_1 and repeat the procedure described above. The iterative process is terminated at z_j, $j = n+1$. It may be noted here that for this iteration, the initial choice for $T_{wall, average}$ is arbitrary and after completion of the run, the condition that is to be checked is given by

$$\frac{\left| Q_{iteration}^{total} - Q_{actual}^{total} \right|}{Q_{actual}^{total}} > 0.001 \tag{7.18}$$

where, $Q_{iteration}^{total}$ represents the total heat absorbed by the wall from $z = z_0$ to $z = z_{n+1}$ and is

given by $\sum_{j=o}^{n} q_j$, where q_j is the heat absorbed from the refrigerant at the (j-1)-th segment,

between $z = z_{j-1}$ and $z = z_j$; and, Q_{actual}^{total} represents the actual heat absorbed by the wall so

that the quality at the outlet of the channel reaches the desired value of 0.0. Therefore,

Q_{actual}^{total} is given by

$$Q_{actual}^{total} = \dot{m}_{ref} x_0 i_{fg} \tag{7.19}$$

If the condition given in Equation 7.18 is met, the next choice of $T_{wall, avg}$ is implemented

(by changing $T_{wall, avg}$ by a small amount $\Delta T_{wall, avg}$) and the iterative process is continued.

Thus, there will be some value of $T_{wall, avg} = \hat{T}_{wall,avg}$ for which the condition in Equation

7.18 will not be met, that is to say the computed quality at the outlet will be

approximately equal to the desired value (i.e. $x_{n+1} \approx 0.0$). For this value of the wall

average temperature, the average channel Nusselt number may be calculated by

$$\overline{Nu}_{corr} = \frac{D_h}{k_l} \left(\frac{Q_{actual}^{total}}{P.(n+1)\Delta z(T_{sat,avg} - \hat{T}_{wall,avg})} \right) \tag{7.20}$$

It may be readily observed that the average heat transfer coefficient derived above, may

also be represented as:

$$\overline{h}_{corr} = \frac{1}{P(n+1)\Delta z} \left(\sum_{j=0}^{n} h_j P\Delta z \right) = \frac{1}{(n+1)} \left(\sum_{j=0}^{n} h_j \right) \tag{7.21}$$

The concept in Equation 7.21 is schematically represented in Figure 7.18 which indicates that the total thermal resistance between the wall and the fluid is actually a parallel array of the wall thermal resistances from the individual segments of the channel, such that

$R_j = 1/(h_j P \Delta z)$, j = 0 to n.
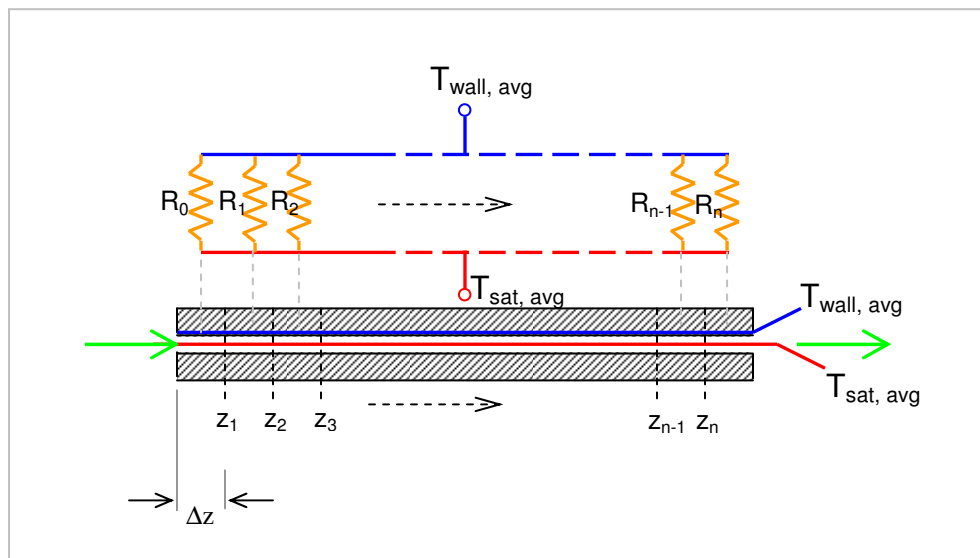
Figure 7.19: Schematic explaining the situation for deriving the average Nusselt number from a given heat transfer correlation.

7.9.2 *Comparison of average Nusselt number from correlation with that from data*

Figure 7.20 presents the comparison of average Nusselt numbers computed from four relevant correlations with Nusselt numbers obtained from experimental average heat transfer data from the present work. It is evident that all these correlations that have been recommended in the literature under-predict the present data by an average of 25%. Specifically, among the four, the Dobson-Chato [20] correlation is a better predictor of the average heat transfer data. We must keep in mind that most of these correlations are built on data-bases for larger hydraulic diameter tubes (>3 mm).
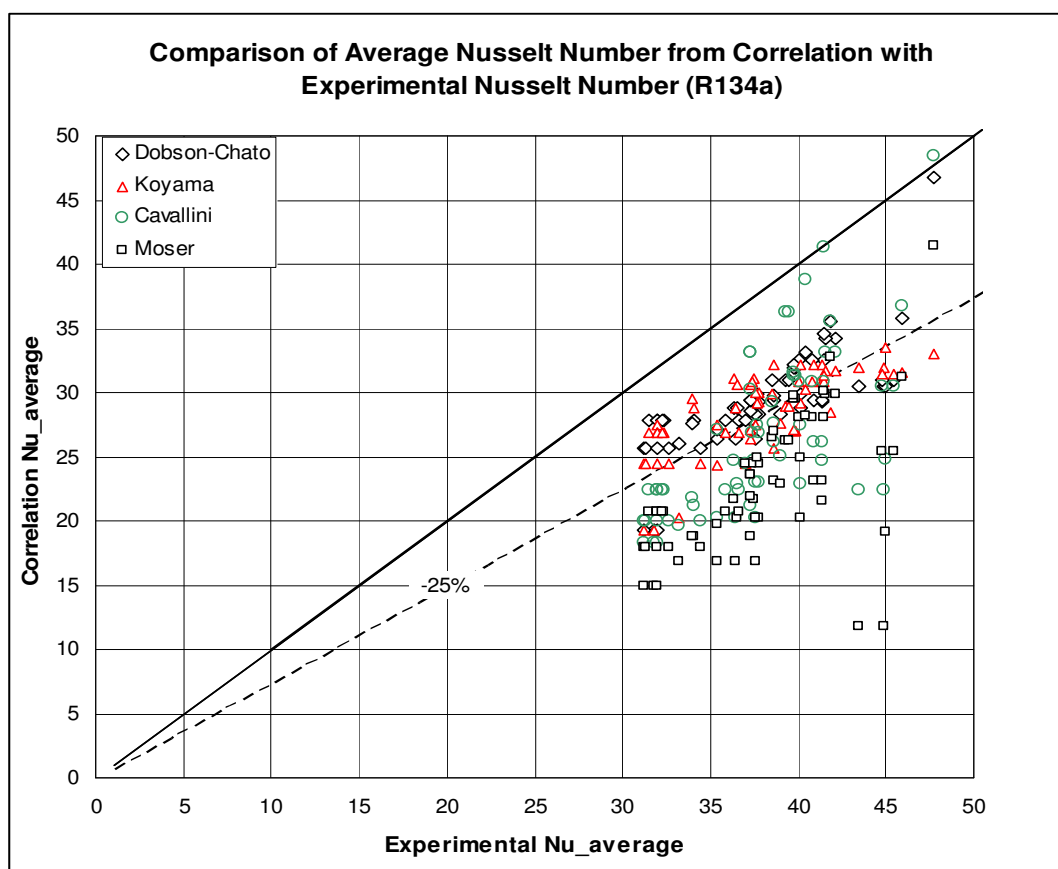
Figure 7.20: Comparison of average Nusselt numbers from correlations and from experimental data for R134a

In the present case, the high aspect ratio micro-channel is considered. As per boiling heat transfer literature, the higher aspect ratio of the channel is responsible for augmented heat transfer. However, the conclusion that higher aspect ratio is indeed responsible for higher heat transfer coefficients in case of condensation should be reserved only after further data is available with different channel aspect ratios at equivalent hydraulic diameter, preferably from a study that employs the same experimental setup (so as to have same entrance/exit characteristics, data collection process, and subject of similar data uncertainties).

Another issue regarding the deviation of the data from the different correlations could be due to the low mass fluxes that are studied in the present work and among them especially those cases in which the inlet quality is less than 0.5. As shown by Koyama et al. [29] in their data comparison, for micro-channels with aspect ratio 2:1 and R134a as fluid, the lower mass flux data (100 to 300 kg/m2.s) in general deviates from the Moser [38] correlation predictions by -30% to -70%. In the present case, the deviation with Moser correlation has been found to be beyond -50%. Cavallini et al. had similar conclusions (under-prediction) when they applied their conventional scale correlation to their data from 1.4 mm diameter channel.

The present analysis of data and comparison of them with some of the correlations indicate the possibility that there is an effect of the high aspect ratio of the present channel which has resulted in higher heat transfer coefficients than that from a lower aspect ratio or circular cross-section channels. This aspect ratio effect should be represented as a correction factor incorporated in the correlations. As an extension of the present work, tests on a few channels with smaller aspect ratios should be carried out to

directly prove this effect. That data would enable the formulation of the correction factor for the aspect ratio.

Lastly, it may be mentioned here that the average data for the refrigerant R245fa have not been compared with the correlations mainly due to the fact that the inlet qualities studied here for this refrigerant are mostly at or above 1.0 (i.e. inlet saturation or superheat condition). Most correlations fail to make predictions at x=1.0.

7.10 SUMMARY

In the present chapter, a detailed description of the test procedure and the average/overall heat transfer coefficient and pressure drop data has been provided for the present work with R134a and R245fa as the working fluids. Selected data from the R134a group have been taken for an approximate inverse heat transfer method using CFD software. This method generated local heat transfer coefficient data which have been compared with most relevant data available literature. Subsequently, this computed data and the average data on heat transfer for R134a have been compared against the available and most relevant correlations. It is acknowledged that the computed data is dependant on the accuracy of the axial temperature profile on the condenser channel wall near the inlet and the outlet. The data indicate that the most of the relevant correlations tend to under-predict the average Nusselt number data by about 25%.

Chapter 8

CONCLUSIONS AND RECOMMENDATIONS FOR FUTURE WORK

8.1 INTRODUCTION

In this last chapter a brief overview and major conclusions from the present work is provided. Additionally, since the present work   represents a research area of continued interest and with broad applications, a set of recommendations for future activities, both on the experimental as well as on the analytical fronts is made to provide a closure.

8.2. OVERVIEW AND CONCLUSIONS FROM PRESENT WORK

The present work mainly encompasses two areas:

1. fabrication of a micro-channel condenser employing the traditional batch fabrication techniques applied to MEMS, and

2.   the experimental heat transfer assessment of the condensation phenomenon in a single horizontal micro-channel with two refrigerants, R134a and R245fa as working fluids, under different test conditions.

In the first area of exploratory research, the feasibility of a design involving bonding of two silicon wafers with interfacing silicon nitride layers and embedded flow channel structures was explorer. Silicon nitride layer bonding methodology has been sparingly reported in open literature and in the knowledge of the present author, this is perhaps the first time such a nitride bond has been explored as a possible technique for creating flow structures. If this process was found successful and convenient, it would reduce the effort in making such structures in silicon wafer by eliminating the requirement of chromium-gold layers typically used as an etch mask for chemical etching of silicon. It was

concluded that the silicon nitride bonding was possible, as shown by some samples successfully bonded; however, the initial thickness of the silicon wafer need to be at least 1 mm in order to etch and bond flow structures as in the present case. Otherwise, the possibility of breakage was found to be significant, and the handling of the samples to be quite difficult. As a precursor to creating the silicon micro-condenser, a similar micro-channel structure conveniently machined in a brass piece was packaged and preliminary experiments were generated to indicate the functional design issues related to the micro-condenser concept.

In the second phase of research, the issue of sizing of condenser with the help of available correlations was explored. Since it was found from the literature survey that only few publications are available which concern the study of refrigerants condensing in sub-millimeter micro-channels, it was deemed necessary to first explore the condensation phenomenon of pressurized refrigerants, like R134a, in a compact condenser channel with high aspect ratio and sub-millimeter hydraulic diameter. Careful effort was made to design and fabricate this compact test setup to accommodate the required test conditions within certain limitations of time and cost. This compact setup provided data with predetermined accuracy and repeatability such that the associated over-all uncertainty for the heat transfer coefficient, was to be at or less than ±10%. The test setup, with modifications from the knowledge from the present work (as suggested later in this chapter), may also enable future experimental tests on micro-channels for just about any orientation with respect to the horizontal, including completely vertical or inclined positions. The typical micro-channels experimental work reported in the literature represents an array of channels with a manifold, rather than a single channel as in the

present study. With multiple channels and manifolding, the results are subjected to uncertainties such as channel internal geometry non-uniformity and flow mal-distribution in the channels.

The test data for heat transfer coefficient have been compared with the values generated from the empirical correlations reported in the experimental literature. Also, for selected test points, the local heat transfer coefficient values were extracted through a CFD-based approximate inverse heat transfer method and were found to be close to the values reported in recent literature. The newer models which take into account the natural effects of surface tension and viscosity in such small channels on the prevailing flow pattern appear to agree better with the present average heat transfer coefficients data than earlier correlations conventional scale tube correlations which did not take into account the small channel effects. This emphasizes the learning that future correlation development should include flow regime identification. Within the present body of work only preliminary visualization observations were conducted, giving insights to the different flow patterns that may exist at some of the test conditions. CFD-based approach on understanding the motion of vapor bubbles in micro-channels were also explored and its applicability was demonstrated to serve as a potential tool to understand the heat and mass transfer behaviors at the vapor-liquid interface which ordinarily cannot be performed without an intrusive technique. However, in order to implement this technique, the interfacial phenomenon needs to be properly modeled with experimental verification.

One of the important drawbacks in the present setup which needs to be eliminated in future research in this area is the resolution of the wall temperature and the wall heat flux

near the entrance and exit of the channel. A modification to that effect is suggested in more details in the recommendations for future work that follows next.

Below, the specific findings from the present work are enumerated to help understand their significance and applicability in the area of design and fabrication of compact condensers for two-phase cooling applications.

1. The research into the feasibility of employing the fusion bonding of two silicon wafers (with embedded flow structures) at their silicon nitride layer interfaces indicates that while this bonding technique is possible, it requires a very smooth and flat interface and also it requires significant effort in surface preparation to maintain surface cleanliness necessary to prevent the formation of voids or un-bonded regions in the interface. This poses as a challenge in a routine operation or in mass fabrication methods.

2. In order to have a robust embedded flow structure that can withstand the handling and packaging requirements, the channel structure must be created in silicon wafers thicker than 1 mm at least; otherwise possibility of breakage of the fragile channel structure is present.

3. The research in the understanding of the flow conditions and in using the present correlations for sizing of the condenser indicates that for high aspect ratio micro-channels, data from which is not reported previously in literature, the present correlations under-predict the overall heat transfer coefficients by about 25% on an average. An averaging technique has been explained to carry out this comparison. The reason for this under-prediction could stem from the fact that in

a high aspect ratio channel, such as used in the present work, the corners of the channel more effectively draw the condensate film towards them due to surface tension and maintain a thin film on the sides of the channel that promotes higher heat transfer rates. A recent analytical work by Wang and Rose [43] which explored only the annular condensation phenomenon alluded to this effect. Also, recent flow visualization data from Coleman and Garimella [22] that had explored the effect of channel shape on flow regimes also implied such an effect. Since most correlations are based on either circular or low aspect ratio rectangular cross-section channels, their under-prediction in the present case is possible. The experimental data at this size of channel is very limited. The comparison of these available data with the present data (derived through CFD-based inverse heat transfer technique), though not at exactly similar test conditions, indicates similar trends, which is encouraging to note.

4. An averaging technique for the comparison of the overall pressure drop data with that from the limited data set in the literature could not be carried out since it required the knowledge of surface heat flux profile along of the channel axis. It is explained why the measurements in the present case does not enable the derivation of this profile. However, it should be noted that the pressure drop levels were of the order of magnitude similar to that in the relevant literature.

5. The refrigerant R245fa which has significantly low GWP and ODP is a possible alternative to some of the present generation refrigerants. This being a new refrigerant, the data with this refrigerant is not available, as far as is known. In the present work, limited tests were carried out to understand the condensation heat

transfer potential of this refrigerant and the data so far is encouraging as it indicates that with this refrigerant, higher levels of heat fluxes can be achieved than with R134a. This helps in further miniaturization of the condenser footprint.

6. The effects of saturation temperature changes and superheat conditions at the inlet to condenser have been presented in addition to the typically studied effect of mass flux variation. The effect of superheat change on the heat transfer coefficient is understandable, but it should be noted that the superheat condition does not change the overall channel pressure drop. The effect of change in saturation temperature is also understandable since the saturation temperature alters the viscous and surface tension effects and also the Prandtl number of the fluid. The variation of the heat transfer and pressure drop as reported in the present work will be helpful in the sizing of the condensers if precise knowledge of the refrigerant conditions is not known.

7. Lastly, an outcome of the literature survey and research during preliminary study on adiabatic bubble hydrodynamics in a millimeter scale channel is the finding that a convincing interfacial mass and heat transfer phenomenon model is not available. If such a model is made available, with parameters defined for each fluid, the bubble motion model can be expanded to complement visualization work to understand the collapse of bubbles at different flow and wall temperature conditions. Also, the vortical structures in the liquid plugs ahead and behind a bubble (in a bubble train), alluded to in Chapter 3, can increase the heat transfer coefficient in the liquid plug and can be modeled easily if heat transfer is included in the model.

8.3 RECOMMENDATIONS FOR FUTURE WORK

Recommendations for future work are divided into two main categories, representing the experimental and numerical work conducted in the present work.

8.3.1 RECOMMENDATIONS FOR EXPERIMENTAL ANALYSIS

In the present experimental analysis, the test setup and test prototype enables measurement of only overall heat transfer coefficient and pressure drop to be obtained. In a practical situation, for the sizing of a compact condenser, such an approach is acceptable. However, as mentioned in the previous chapter, in order to compare the obtained data with available correlations, either an averaging technique needs to be applied or an inverse heat transfer technique needs to be devised to obtain local information for a direct comparison. A more involved approach would be to create a test prototype channel with possibility of direct local measurements of heat flux and wall temperatures, both on the refrigerant-side and the coolant-side. As was the experience in designing the current setup, such a test section having instrumentation for full-scale local measurements becomes too complicated to design and maintain. Also, the possibility of parasitic heat transfers (undesired losses/gains) encourages the design to be as un-intrusive and uncluttered as possible. Several experimentalists have used a pre- and post-condenser heat exchangers upstream and downstream to their test sections (*viz.* Koyama et al. [29]) so that the inlet and exit qualities for the test sections were maintained close to the desired value. (The difference between the inlet and outlet qualities is allowed to be only a few percent points, so that the heat and pressure drop data can be ascribed to the

average quality in the test section.) In such a case, the amount of heat transfer from the refrigerant-side is small and cannot be directly measured with high degree of accuracy due to overwhelming parasitic losses and instrument limitations. Garimella et al [35] has employed a thermal magnification technique which involved a second coolant loop to magnify the refrigerant-to-coolant heat transfer while maintaining the desired accuracy. However, in their case, an array of channels were employed instead not a single channel which, while assisting the data certainty, leaves behind the question of possible mal-distribution of flow in the channels. In any case, such a technique is desirable if the extra thermal loop and instrumentation for that loop can be afforded. However, whether or not the entrance and exit conditions to the test section (due to transition from pre- and post-condensers) are altered is also another important issue that needs to be considered.

Also, in the present test setup, the value of the coolant jacket flow diameter was so chosen as to enable wall thermocouple wires to be routed out of the jacket without significantly influencing the axial coolant flow. However, as evidenced in the results from CFD-modeling of this flow, which did not even consider the effect of the thermocouple wires, due to asymmetric inlet and outlet locations the flow tended to have a swirl and also the coolant-side heat transfer coefficient was not same at different axial locations of the channel outer surface. Due to this, a simple Wilson Plot technique could not be adopted to get the local information. Figure 8.1 below shows a sketch of an alternative design that may better serve the purposes of deriving local data. The three tier structure, with the refrigerant condenser channel sandwiched between two coolant tubes, will enable a predictable coolant flow pattern. If thermocouples (not shown) were inserted into the coolant flow and into the condenser channel wall at several appropriate

locations along the axis, the coolant-side local heat flux, coolant temperature and wall temperatures for both condenser and coolant tubes can be obtained. Since the condenser/coolant-tube wall temperature axial profile is obtained, the wall conduction can be computed within reasonable accuracy. With these measurements, it will be possible to obtain the refrigerant-side local heat flux axial profile and hence local heat transfer coefficients. If pressure ports with access into the refrigerant path are provided on the condenser wall at several places along the axis, local pressure measurements can be obtained as well. However, too many pressure ports can interfere with the internal flow dynamics and hence would not be advisable.

8.3.2 RECOMMENDATIONS FOR ANALYTICAL & NUMERICAL STUDIES

A few researchers have attempted to make simplified analytical models for the condensate films in small channels dominated by surface tension and vapor-liquid interfacial shear forces and to a less extent by gravitational acceleration.
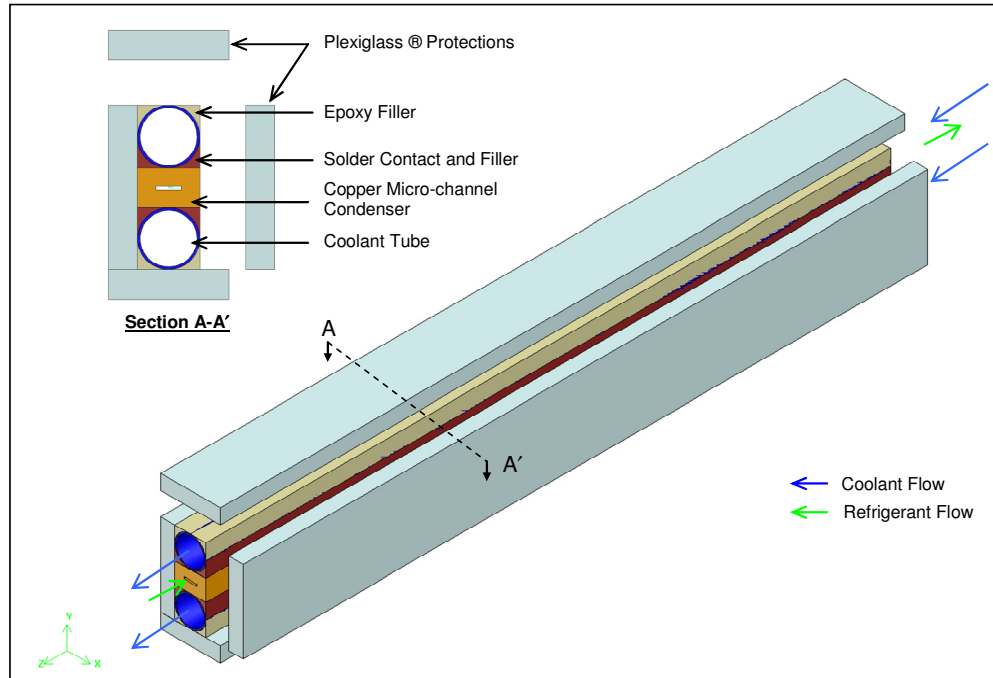
Figure 8.1: A semi-exploded sketch of a proposed improved test section

Notable among these attempts are those of Wang and Rose [42, 43] and Begg, Khrustalev and Faghri [41]. Bandhauer, Agarwal and Garimella [35] had attempted to create a semi-empirical model of the condensate film interfacial temperature based on an earlier work by Traviss et al. [13] and from there, they had attempted to calculate the local heat transfer coefficients. All of the above models depend heavily on much earlier works on the interfacial heat transfer, mass transfer and shear models based mostly on data from conventional scale tubes. For example, Wang and Rose's work has adopted the approach suggested by Mickley et al which was later used by Kays, Crawford and Weigand [45], and Cavallini [57]. The interfacial shear stress is given by:

$$\tau_i = 0.5 f \rho_v U_v^{2} \qquad (8.1)$$

where, the interfacial friction factor is denoted by f and the average vapor velocity by U_v.

The expression used for the interfacial friction factor is related to the condensation mass flux, $\dot{m}''$ and the zero transpiration (i.e. no net mass exchange) value of the interfacial friction factor, $f_{0,v}$ by:

$$f = \frac{\left(-\dfrac{2\dot{m}''}{f_{0,v}\rho_v U_v}\right)}{\exp\left(-\dfrac{2\dot{m}''}{f_{0,v}\rho_v U_v}\right)-1} \tag{8.2}$$

The condensate mass flux, $\dot{m}''$ is used as a variable in their set of equations while the zero transpiration friction factor, $f_{0,v}$ is adopted from Churchill [46]:

$$f_{0,v} = 2\left[\left(\frac{8}{\mathrm{Re}_v}\right)^{12} + \frac{1}{\left(\left\{5.6569\log\left(\frac{6.9}{\mathrm{Re}_v}\right)^{0.9} + \frac{\varepsilon}{3.71 D_{hv}}\right\}^{16} + \left\{\frac{37530}{\mathrm{Re}_v}\right\}^{16}\right)^{1.5}}\right]^{1/12} \tag{8.3}$$

where, ε is the surface roughness, D_{hv} is the vapor hydraulic diameter and Re_v is the local vapor Reynolds Number, given by $\mathrm{Re}_v = \rho_v U_v D_{hv}/\mu_v$. Here D_{hv} is another variable used in their equation set.

Begg et al [41] have used a similar expression relating to the condensation friction factor, f to the zero transpiration friction factor, $f_{0,v}$. However, in their work, the expression for the zero-transpiration friction factor is adopted from Bowman and Hitchcock [58] which is different from the expression in Equation 8.3. Bandhauer et al [35] has adopted a different way of relating the interfacial friction factor to the flow parameters and then using that to find the interfacial stress. However, in their approach, the interfacial suction effect due to condensation is indirectly related to the interfacial

friction factor through the local liquid Reynolds Number $\mathrm{Re}_l = \dfrac{GD(1-x)}{(1+\sqrt{\alpha})\mu_l}$, where G is

the total refrigerant mass flux, D is the hydraulic diameter of the channel, x is the local

vapor quality and μ_l is the liquid viscosity. α represents the void fraction given by

Baroczy [61].

In parallel, similar work has been performed in describing the interfacial activity

in case of cavitation of liquid into bubbles and condensation of the vapor back into liquid,

most notably by Senocak and Shyy [62] who have compared experimental results with

three recent models and proposed their own. However, their model for interfacial mass

flux depends on defining a characteristic length scale and free stream velocity of the fluid

which poses difficulty in application in case of condensation in micro-channels.

In short, it is apparent that the approaches in modeling the interfacial phenomenon

is varied and tend to depend on earlier works based on conventional scale tubes or

channels. The preliminary investigation in CFD modeling of a bubble motion, as

presented in this work, and similar work carried out by Taha and Cui [49, 50, 51], van

Baten and Krishna [52], Zheng [53] and others indicate significant interest in capturing

the actual physical phenomena and incorporating it in a numerical model. Any such

attempt will be benefited if a convincing model of interfacial dynamics for condensing

flows in micro-channels may be developed with experimentally-derived parameters (such

as accommodation coefficient etc.) for different fluids. Clearly, this presents itself as an

opportunity for further research in modeling and experimental corroboration.

8.4 SUMMARY

In this chapter a brief overview and conclusions from present work was provided, with specific findings enumerated. It was followed by recommendations for future work for certain new dimensions in the experimental measurements, as well as numerical modeling on condensation in micro channels. Of particular interest are local measurement of the heat transfer and pressure drop data; also, the need for a comprehensive and more convincing interfacial dynamics model were emphasized to facilitate more realistic modeling of the actual phenomenon of condensation in micro channels.

REFERENCES

[1]   Sherizawa, A., Feng, Z., and Kawara, Z., "Two-phase flow in micro-channels," Experimental Thermal and Fluid Sciences, volume 26, issue 6-7, pages 703-714, 2002.

[2]   Kew, P. A., and Cornwell, K., "Correlations for the prediction of boiling heat transfer in small-diameter micro-channels," Applied Thermal Engineering, volume 17, issue 8-10, pages 705-715, 1997.

[3]   Butterworth, D., "A comparison of some void-fraction relationships for co-current gas liquid flow," International Journal of Multiphase Flow, volume 1, issue 6, 845-850, 1975.

[4]   Smith, S. L., "Void-fractions in two-phase flow: a correlation based upon an equal velocity head model," Proceedings of the Institution of Mechanical Engineers, Thermodynamics and Fluid Mechanics Group, pages 647-657, 1969.

[5]   Premoli, A., Francesco, D., and Prina, A., "A dimensionless correlation for determining the density of two-phase mixtures," La Termotecnica, volume 25, pages 17-26, 1971.

[6]   Kariyasaki, A., Fukano, T., Ousaka, A., and Kagawa, M., "Characteristics of time-varying void fraction in isothermal air-water co-current flow in horizontal capillary tube," Transactions of JSME, volume 57(B), pages 4036-4043, 1991.

[7]   Mishima, K., and Hibiki, T., "Visualization and measurement of two-phase flow by using neutron radiography," Nuclear Engineering and Design, volume 175, issue 1-2, pages 25-35, 1997.

[8]   Mishima, K., and Hibiki, T., "Development of high-frame-rate neutron radiography and quantitative measurement method for multi-phase flow research," Nuclear Engineering and Design, volume 184, issue 2-3, pages 183-201, 1998.

[9]   Triplett, K. A., Ghiaasiaan, S. M., Abdel-Khalik, S. I., LeMouel, A., and McCord, B. N., "Gas-liquid two-phase flow in micro-channels: part II: void-fraction and pressure drop," International Journal of Multiphase Flow, volume 25, issue 3, pages 395-410, 1999a.

[10] Triplett, K. A., Ghiaasiaan, S. M., Abdel-Khalik, S. I., and Sadowski, D. L., "Gas-liquid two-phase flow in micro-channels: part I: two-phase flow patterns," International Journal of Multiphase Flow, volume 25, issue 3, pages 377-394, 1999b.

[11] Lowe, D. C., and Rezkallah, K. S., "Flow regime identification in microgravity two-phase flows using void fraction signals," International Journal of Multiphase Flow, volume 25, issue 3, pages 433-457, 1999.

[12] Kawahara, A., Sadatomi, M., Okayama, K., Kawaji, M., and Chung, P. M.-Y., "Effect of channel diameter and liquid properties on void fraction in adiabatic two-phase flow through micro-channels," Heat Transfer Engineering, volume 26, issue 3, pages 13-19, 2005.

[13] Traviss, D. P., Rohsenow, W. M., and Baron, A. B., "Flow regimes in horizontal two-phase flow with condensation," ASHRAE Transactions, volume 79, issue 2, pages 31-39, 1973.

[14] Breber, G., Palen J. W., and Taborek, J., "Prediction of horizontal tube-side condensation of pure components using flow regime criteria," Journal of Heat Transfer, Transactions of ASME, volume 102, issue 3, pages 471-476, 1980.

[15] Sardesai, R. G., Owen, R. G., Pulling, D. J., "Flow regimes for condensation of a vapor inside a horizontal tube," Chemical Engineering and Science, volume 36, issue 7, pages 1173-1180, 1981.

[16] Soliman, H. M., "On the annular-to-wavy flow pattern transition during condensation inside horizontal tubes," Canadian Journal of Chemical Engineering, volume 60, issue 4, pages 475-481, 1982.

[17] Soliman, H. M., "Mist-annular transition during condensation and its influence on the heat transfer mechanism," International Journal of Multiphase Flow, volume 12, issue 2, pages 277-288, 1986.

[18] Tandon, T. N., Varma, H. K., and Gupta, C. P., "New flow regimes map for condensation inside horizontal tubes," Journal of Heat Transfer, volume 104, issue 4, pages 763-768, 1982.

[19] Wang, C. C., Chiang, C. S., and Lu, D. C., "Visual observation of two-phase flow pattern for R22, R134a, and R407C in a 6.5 mm smooth tube," Experimental Thermal and Fluid Sciences, volume 15, issue 4, pages 395-405, 1997.

[20] Dobson, M. K., and Chato, J. C., "Condensation in smooth horizontal tubes," Journal of Heat Transfer, Transactions of ASME, volume 120, issue 1, pages 193-213, 1998.

[21] Coleman, J. W., and Garimella, S., "Characterization of two-phase flow patterns in small diameter round and rectangular tubes," International Journal of Heat and Mass Transfer, volume 42, issue 15, pages 2869-2881, 1999.

[22] Coleman, J. W., and Garimella, S., "Two-phase flow regimes in round, square, and rectangular tubes during condensation of refrigerant R134a," International Journal of Refrigeration, volume 26, issue 1, pages 117-128, 2003.

[23] Yang, C. Y., and Webb, R. L., "Condensation of R-12 in small hydraulic diameter extruded aluminum tubes with and without micro-fins," International Journal of Heat and Mass Transfer, volume 39, issue 4, pages 791-800, 1996a.

[24] Yang, C. Y., and Webb, R. L., "Friction pressure drop of R-12 in small hydraulic diameter extruded aluminum tubes with and without micro-fins," International Journal of Heat and Mass Transfer, volume 39, issue 4, pages 801-809, 1996b.

[25] Zhang, M., and Webb, R. L., "Correlation of two-phase friction for refrigerants in small-diameter tubes," Experimental Thermal and Fluid Sciences, volume 25, issue 3-4, pages 131-139, 2001.

[26] Webb, R. L., and Ermis, K., "Effect of hydraulic diameter on the condensation of R134a in Flat Extruded Aluminum tubes," Journal of Enhanced Heat Transfer, volume 8, issue 2, pages 77-90, 2001.

[27] Garimella, S., and Bandhauer, T. M., "Measurement of condensation heat transfer coefficients in micro-channel tubes," Proceedings of ASME International Mechanical Engineering Congress and Exposition, N.Y., pages 243-249, 2001.

[28] Wilson, M. J., Newell, T. A., Chato, J. C. and Infante Ferreira, C. A., "Refrigerant charge, pressure drop and condensation heat transfer in flattened tubes," International Journal of Refrigeration, volume 26, issue 4, pages 442-451, 2003.

[29] Koyama, S., Kuwahara, K., Nakashita, K., and Yamamoto, K., "An experimental study of condensation of refrigerant R134a in a multi-port extruded tube," International Journal of Refrigeration, volume 26, issue 4, 425-432, 2003.

[30] Wang, W. W.-W., Radcliff, T. D., and Christensen, R. N., "A condensation heat transfer correlation for milli-meter scale tubing with flow regime trasition," Experimental Thermal and Fluid Sciences, volume 26, issue 5, pages 473-485, 2002.

[31] Baird, J. R., Fletcher, D. F., and Haynes, B. S., "Local Condensation Heat Transfer Rates in Fine Passages," International Journal of Heat and Mass Transfer, volume 46, pages 4453-4466, 2003.

[32] Cavallini, A., Del Col, D., Doretti, L., Matkovic, M., Rosetto, L., and Zilio, C., Condensation heat transfer and pressure gradient inside multiport minichannels," Heat Transfer Engineering, volume 26, issue 3, pages 45-55, 2005.

[33] Cavallini, A., Del Col, D., Doretti, L., Matkovic, M., Rossetto, L., and Zilio, C., "Update on Condensation Heat Transfer and Pressure Drop inside Minichannels," Heat Transfer Engineering, volume 27, no. 4, pages 74-87, 2006.

[34] Kim, M. H., Shin, J. S., Huh, C., Kim, T. J., and Seo, K. W., "A Study of Condensation Heat Transfer in a Single Mini-Tube and Review of Korean Micro-

and Mini-Channel Studies," Proceedings of the First International Conference on Micro-channels and Mini-channels, Rochester, N.Y., pages 47-58, 2003.

[35] Bandhauer, T. M., Agarwal, A., and Garimella, S., "Measurement and modeling of condensation heat transfer, coefficients in circular micro-channels, Journal of Heat Transfer, volume 128, pages 1050-1058, 2006.

[36] Haraguchi, H., Koyama, S., Fujii, T., "Condensation of refrigerants HCFC22, HFC134a and HCFC123 in a horizontal smooth tube: proposal of empirical expressions for the local heat transfer coefficient," Transactions of JSME(B), volume 60(574), pages 245–252, 1994.

[37] Mishima, K., and Hibiki, T., "Effect of inner diameter on some characteristics of air-water two-phase flows in capillary tubes," Transactions of JSME(B), volume 61, pages 99–106, 1995.

[38] Moser, K. W., Webb, R. L., and Na, B., "A new equivalent Reynolds number models for condensation in smooth tubes," Journal of Heat Transfer, Transactions of ASME, volume 120, issue 2, pages 410-417, 1998.

[39] Friedel, L., "Pressure drop during gas/vapor-liquid flow in pipes," International Journal of Chemical Engineering, volume 20, issue 3, pages 352-367, 1980.

[40] Cavallini, A., Censi, G., Del Col, D., Doretti, L., Longo, G. A., and Rossetto, L., "Condensation of halogenated refrigerants inside smooth tubes," HVAC and R Research, volume 8, issue 4, pages 429-451, 2002.

[41] Begg, E., Khrustalev, D., and Faghri, A., "Complete condensation of forced-convection two-phase flow in a miniature tube," Journal of Heat Transfer, Transactions of ASME, volume 121, pages 904-905, 1999.

[42] Wang, H. S., and Rose, R. W., "A theory of film condensation in horizontal non-circular section microchannels," Journal of Heat Transfer, Transactions of ASME, volume 127, pages, 1096-1105, 2005.

[43] Wang, H. S., and Rose, R. W., "Film condensation in horizontal microchannels: effect of channel shape," International Journal of Thermal Sciences, volume 45, pages 1205-1212, 2006.

[44] Munoz-Cobo, J. L., Herranz, L., Sancho, J., Tkachenko, I., and Verdu, G., "Turbulent vapor condensation with non-condensable gases in vertical tubes," International Journal of Mass Transfer, volume 39, no. 15, pages 3249-3260.

[45] Kays, W. M., Crawford, M. E. and Weigand, B., Convective Heat and Mass Transfer, 4th edition, McGraw-Hill, N. Y., pages 212–215, 2005.

[46] Churchill, S. W., "Friction-factor equation spans all fluid-flow regimes," Chemical Engineering Progress, volume 84, pages 91–92, 1977.

[47] Chen, Y., and Cheng, P., "Condensation of steam in silicon microchannels," International Communications of Heat and Mass Transfer, volume 32, pages 175-183, 2005.

[48] Nijhuis, T. A., Kreutzer, M. T., Romijn, A. C. J., Kapteijn, F., and Moulijn, J. A., "Monolithic catalysts as efficient three phase reactors," Chemical Engineering Science, volume 56, pages 823-829.

[49] Taha, T., and Cui, Z. F., "Hydrodynamics of slug flow inside capillaries," Chemical Engineering Science, volume 59, pages 1181-1190, 2004.

[50] Taha, T., and Cui, Z. F., "CFD modeling of slug flow in vertical tubes," Chemical Engineering Science, volume 61, pages 676-687, 2006.

[51] Taha, T., and Cui, Z. F., "CFD modeling of slug flow inside square capillaries," Chemical Engineering Science, volume 61, pages 665-675, 2006.

[52] van Baten, J. M., Krishna, R., "CFD simulations of mass transfer from Taylor bubbles rising in circular capillaries," Chemical Engineering Science, volume 59, pages 2535-2545, 2004.

[53] Zheng, D., He, X., and Che, D., "CFD simulations of hydrodynamic characteristics in a gas-liquid vertical upward slug flow," International Journal of Heat and Mass Transfer, volume 50, pages 4151-4165, 2007.

[54] FLUENT ver. 6.3 User's Guide, ANSYS, Inc., PA, U.S.A.

[55] Teng, H., Cheng, P., and Zhao, T. S., "Instability of condensate film and capillary blocking in small-diameter-thermosyphon condensers," International Journal of Heat and Mass Transfer, volume 42, pages 3071-3083, 1999.

[56] Cavallini, A., Censi, G., Del Col, D., Doretti, L., Longo, G. A., and Rossetto, L., "Experimental investigation on condensation heat transfer and pressure drop of new HFC refrigerants (R134a, R125, R32, R410A, R236ea) in a horizontal smooth tube," International Journal of Refrigeration, volume 24, pages 73-87, 2001.

[57] Cavallini, A., Del Col, D., Doretti, L., Longo, G. A., and Rossetto, L., "A New Computational Procedure for Heat Transfer and Pressure Drop during Refrigerant Condensation inside Enhanced Tubes," Journal of Enhanced Heat Transfer, volume 6, pages 441–456, 1999.

[58] Bowman, W. J., and Hitchcock, J. E., "Transient, Compressible Heat Pipe Vapor Dynamics," Proceedings of ASME National Heat Transfer Conference, Houston, TX, volume 1, pages 329-338. 1988.

[59]   Sanchez, S., Gui, C., Elwenspoek, M.,"Spontaneous Direct Bonding of Thick Silicon Nitride", Journal of Micromechanics and Microengineering, volume 7, pages 111-113, 1997.

[60] Bower, R. W., Ismail, M. S., Roberds, B. E., "Low Temperature Si_3N_4 Direct Bonding", Applied Physics Letters, volume 62, no. 26, pages 3485-3487, 1993.

[61] Baroczy, C. J., "Correlation of Liquid Fraction in Two-Phase Flow with Applications to Liquid Metals," Chemical Engineering Prog., Symposium Ser., volume 61(57), pages 179–191, 1965.

[62] Senocak, I., Shyy, W., "Interfacial Dynamics-based Modeling of Turbulent Cavitating Flows, Part-1: Model Development and Steady-state Computations," International Journal for Numerical Methods in Fluids, volume 44, pages 975-995, 2004.

[63]   Kandlikar, S. G., Garimella, S., Li, D., Colin, S., King, M. R., "Heat Transfer and Fluid Flow in Minichannels and Microchannels," Elsevier (Singapore) Pte Ltd., 2006.

[64] Ghiaasiaan S. M., "Two-phase Flow, Boiling and Condensation: In Conventional and Miniature Systems," Cambridge University Press, 2008.